THESIS

DIAGNOSING THE ANGULAR MOMENTUM FLUXES THAT DRIVE THE QUASI-BIENNIAL OSCILLATION

Submitted by

Ann-Casey Hughes

Department of Atmospheric Science

In partial fulfillment of the requirements

For the Degree of Master of Science

Colorado State University

Fort Collins, Colorado

Fall 2023

Master's Committee:

Advisor: David A. Randall

James Hurrell
Iuliana Oprea

ABSTRACT

DIAGNOSING THE ANGULAR MOMENTUM FLUXES
THAT DRIVE THE QUASI-BIENNIAL OSCILLATION

The quasi-biennial oscillation (QBO) is a descending pattern of alternating easterly and westerly equatorial stratospheric winds that is produced by the upward transport of momentum in multiple types of atmospheric waves. The discovery of the QBO and its role in the global circulation are discussed. The angular momentum budget of the QBO is analyzed using ERA-Interim isentropic analyses. We explain the benefits of isentropic coordinates and angular momentum as tools for analyzing atmospheric motion. We diagnose vertical motion utilizing continuity, allowing direct computation of the angular momentum fluxes due to vertical motion. The angular momentum fluxes due to unresolved convectively generated gravity waves are computed as a residual. These results are discussed with the goal of improving the representation of sub-grid scale motions in numerical models. We also discuss these results within the context of the reliability of reanalysis datasets and the downsides to treating reanalysis data as observations. We also revisit and discuss the seasonal dependence of the QBO transition.

TABLE OF CONTENTS

Chapter 1

Introduction

1.1 What is the QBO?

The quasi-biennial oscillation (hereafter, the QBO) is a descending pattern of alternating easterly and westerly equatorial stratospheric winds that terminates near the tropopause. The amplitude of the oscillation at the equator is approximately 20 m s^{-1} between 5-40 hPa, diminishing to less than 5 m s^{-1} at the stratopause, near 1 hPa [Baldwin et al., 2001]. The period of the oscillation ranges from 20 to 37 months, averaging 28 months [Anstey et al., 2022]. Westerly shear zones (in which westerly winds increase with height) descend more regularly and rapidly than easterly shear zones [Baldwin et al., 2001]. In Figure 1.1, we show the zonally averaged monthly averaged time series of zonal wind in the stratosphere on isentropic surfaces. The easterly and westerly phases will be called QBO-E and QBO-W. Figure 1.1 shows the maximum easterly wind to be on the order of -40 m s^{-1}, whereas the maximum westerly wind peaks closer to 25 m s^{-1}. We can also see that the pattern of descent was disrupted in the years between 2015-2018. A similar disruption occurred in the years between 2018 and 2023.

Moving meridionally away from the equator, the amplitude has an approximately Gaussian spatial distribution out to 12° N and S [Wallace, 1973]. The wind signal of the QBO is approximately independent of longitude, so a zonal average gives a clear picture of QBO behavior. In Figure 1.2, we show the zonally averaged monthly averaged time series of zonal wind (with the seasonal cycle removed) on the 600 K isentropic surface, or approximately 20 hPa near the Equator, showing the meridional structure of QBO winds [Belmont and Dartt, 1968]. In the 2022 paper, "Impacts, processes and projections of the quasi-biennial oscillation," James Anstey describes the QBO as "arguably the most predictable mode of atmospheric variability that is not linked to the changing seasons" [Anstey et al., 2022].

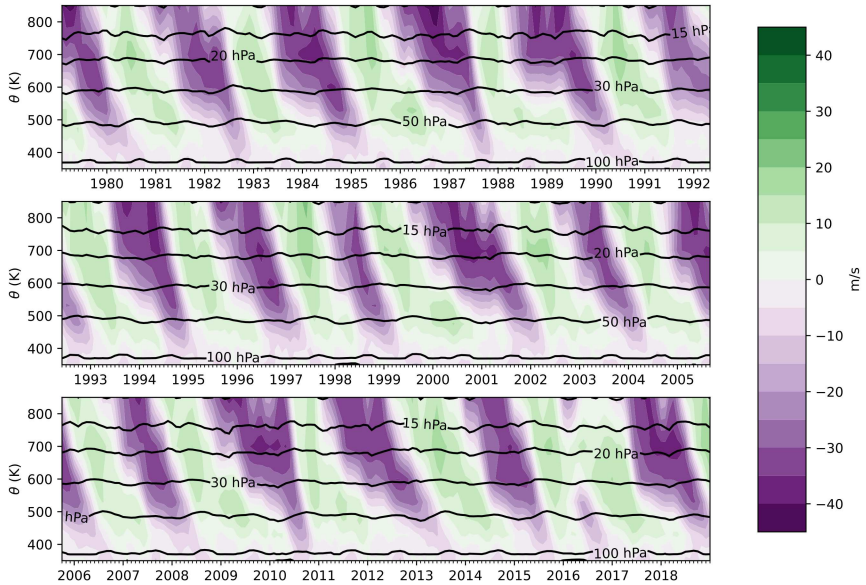

Figure 1.1: Time series from 1979-2018 of zonally and monthly averaged **zonal wind** on isentropic surfaces from ERA-Interim *in the stratosphere*. Results have been meridionally averaged from 5°N - 5°S. Pressure contours have been included for orientation.

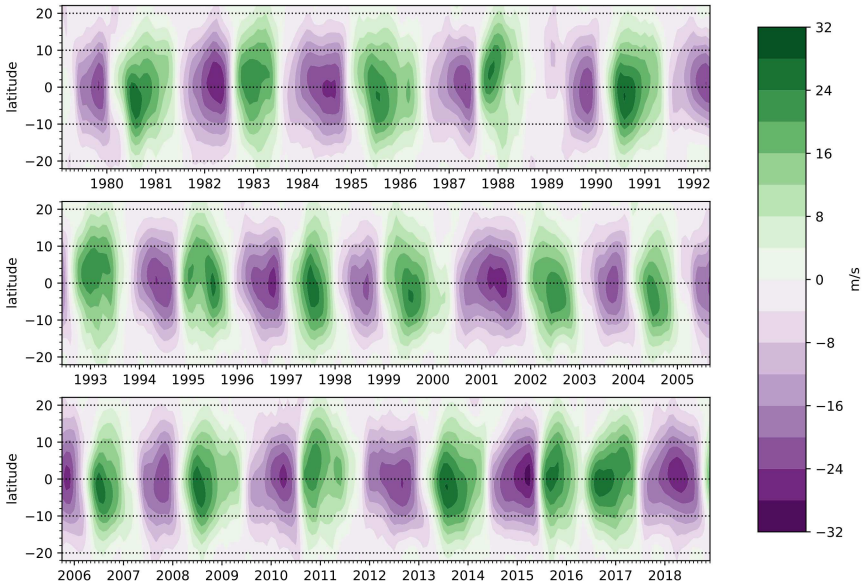

Figure 1.2: Time series from 1979-2018 of zonally and monthly averaged deseasonalized **zonal wind** on the 600 K isentropic surface from ERA-Interim between 22°N - 22°S.

The QBO is driven by interactions between vertically propagating equatorial waves and zonal mean flow in the stratosphere [Lindzen and Holton, 1968; Holton and Lindzen, 1972]. This includes waves of varying scales, including: Kelvin waves, Rossby-gravity waves, inertia-gravity waves, and smaller scale gravity waves [Baldwin et al., 2001]. The most uncertainty arises from unresolved smaller scale gravity waves. The other waves have lower frequencies and longer wavelengths, allowing for detection in observations, as well as ability to resolve them in coarse-resolution earth system models.

There is a quasi-biennial signal in other variables–temperature, ozone concentration, and more. There is also a secondary meridional circulation, creating a path for extratropical teleconnections. Figure 1.3 from Anstey et al. [2022] summarizes the main drivers of the QBO and its global impacts. Westerly winds are shown in red and easterly winds are shown in blue. Driving waves are shown as black arrows. Other aspects of the global circulation that are impacted by or impact the QBO are the overturning meridional circulation (the Brewer Dobson circulation), the thermal wind-driven mean meridional circulation (also called the QBO secondary circulation), and extratropical planetary Rossby waves. Each element shown in Figure 1.3 will be discussed later in Chapter 1.

1.2 QBO History (late 19th century-present)

1.2.1 The Krakatau Easterlies (1883-1907)

The first observation that foreshadowed the eventual discovery of the quasi-biennial oscillation was the discovery of the "Krakatau easterlies" after the 1883 eruption of Krakatau, a volcano in the active volcanic chain in the Sunda Strait – the passage of water between the islands of Sumatra and Java. The eruption was one of the first global events reported around the world in real-time, made possible by the new intercontinental telegraph network, and is often still referred as "Krakatoa" because of an erroneous early radio report. Radiative impacts of the stratospheric aerosol included strange optical phenomena, which were reported on across the globe in the following days and weeks [Hamilton, 2012].

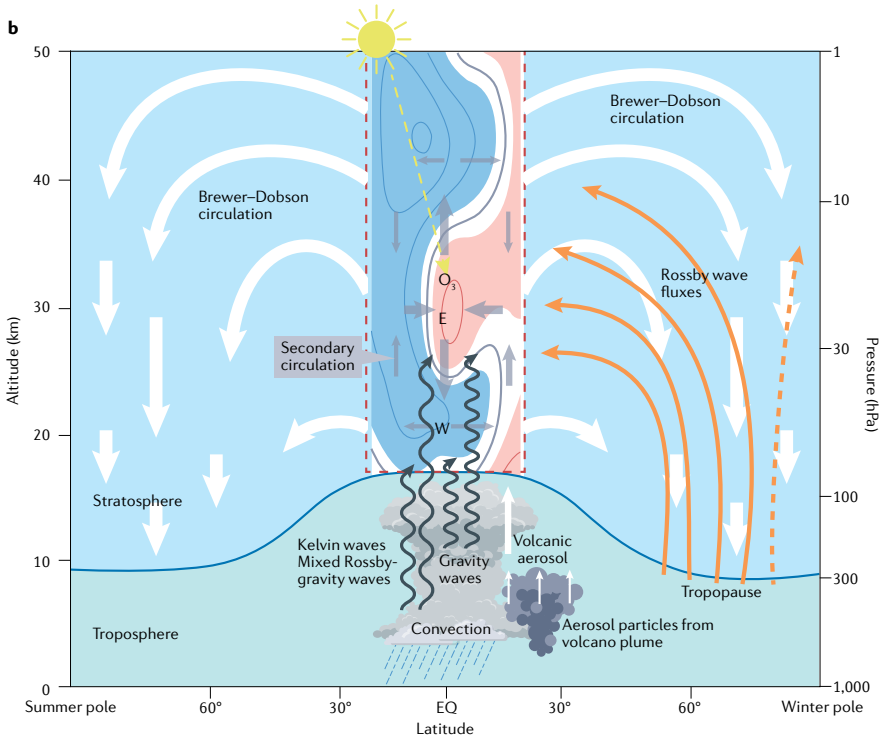

Figure 1.3: Figure 1b from [Anstey et al., 2022]. The original caption: "Eastward (E) and westward (W) zonal winds (red and blue, respectively) in the tropical stratosphere (box bounded by dashed red line) when the QBO phase is transitioning from westward to eastward at 30 hPa (zero-wind line, thick grey contour), and the semi-annual oscillation (SAO) in the upper stratosphere is in its westward phase. Rossby waves propagate through the winter extratropical stratosphere (orange arrows), transporting westward momentum equatorwards that can be important for 'QBO disruption' events. Black wavy arrows represent upwards-propagating tropical waves that drive the QBO in the canonical model (see Box 1). The QBO is also affected by the overturning circulation of the stratosphere (Brewer–Dobson circulation, thick white arrows) and the QBO mean-meridional circulation maintaining thermal wind balance, hereinafter referred to as the QBO secondary circulation (grey arrows inside red dashed box), which modulates the distribution of ozone."

In the May 1884 issue of the Hawaiian Monthly [Bishop, 1884]), Rev. Dr. Sereno Bishop describes the August 1883 eruption of Krakatau that “shot to unmeasured heights millions of tons of the fiery entrails of earth,” producing “a swift strong fling. . . of a vast stream of smoke” traveling “due west with precision along a narrow equatorial belt, at an enormous velocity, nearly around the globe.” Synthesizing reports from surrounding nations, he determined the “broad sheets of gold and olive green and blazing crimson” in the “upper atmospheric strata” travelled 18000 miles westward in 10 days from Java to his location in Honolulu. This is approximately 33 meters per second, consistent with what is now known as the easterly phase of the QBO. In an 1888 report made by the Royal Society of London [Russell and Symons, 1888], the Honorable Rollo Russell, born during his father Lord John Russell’s time as British prime minister, synthesized data from personal reports, telegraph communications, and newspapers from around the globe to characterize the temporal and spatial behavior of the plume in the aftermath of the eruption (Figure 1.4). Bishop’s observations, in congruence with the reports of Rollo Russell from the Royal Society report in 1888, created the notion of the "Krakatau easterlies."

1.2.2 The Berson Westerlies (1908-1959)

A second important contribution to the discovery of the QBO was the "Berson westerlies." Arthur Berson was a German meteorologist who, in 1890, was an assistant to Richard Aßman at the Meteorological Institute in Berlin. There, Berson manned balloons that ascended to great heights. During one expedition, he rose to 10800 feet and fell unconscious, just after he opened a valve for descent. Aßman and the French meterologist Léon Teisserenc de Bort are credited with the 1902 discovery of the stratosphere. In the early twentieth century, tropical meteorology was an area of much interest because of colonial powers’ territory near the Equator and the large populations near the equator [Brönnimann and Stickler, 2013]. In 1908, Arthur Berson and others members of the Royal Aeronautic Observatory made an expedition to Eastern Africa, visiting Lake Victoria, Dar es Salaam (Tanzania), Mombasa (Kenya) and Mozambique, with the goal of studying east African monsoon circulation and tropical cyclone activity. During the ex-

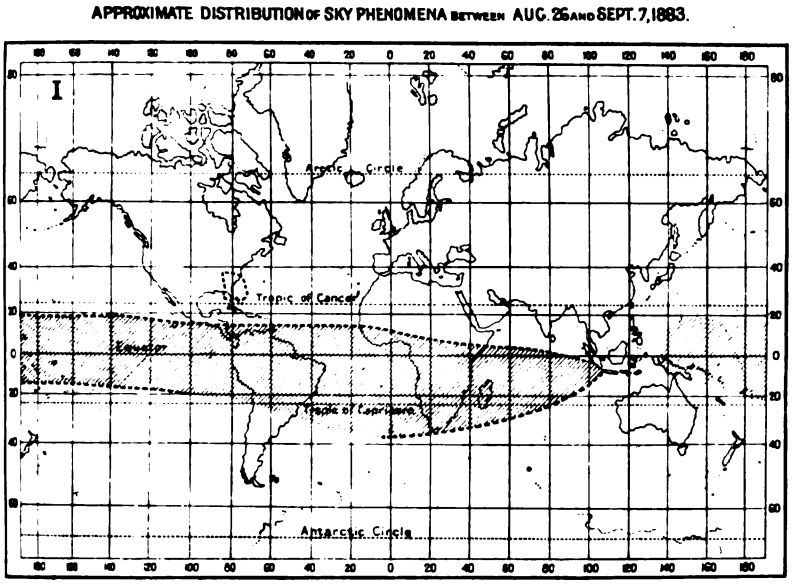

Figure 1.4: Rollo Russell's sketch of "The Approximate Distribution of Sky Phenomena between 27 August and 7 September 1883" in the aftermath of the eruption of Krakatau in Java. From one of Russell's sections, "Spread of the Phenomena Round the World, with Maps Illustrated Thereof," in the Royal Society's 1888 report, *The Eruption of Krakatoa and Subsequent Phenomena.*
[Russell and Symons, 1888]

pedition, successful observations included 25 registering balloon ascents, 65 kite ascents, and 84 pilot balloon ascents. Berson published a 1908 paper that was translated to English by Reinhard Suring in 1910 [Süring, 1910], recounting the expedition and two lasting discoveries: that the tropical tropopause was much higher and colder than that over the midlatitudes, and that westerly winds filled the lower stratosphere, contradicting the Krakatau easterlies. The Berson Westerlies were erroneously believed to occupy a small cross-section in the lowermost stratosphere, surrounded by easterlies, shown in the Figure 1.5. This configuration was created to explain away the contradictory observations between easterly and westerly equatorial stratospheric winds and remained in textbooks until the 1960s [Hastenrath, 2007].

1.2.3 Discovery of the oscillatory winds (1959-1963)

The first documented observations of the descending pattern of the QBO are in the April 1959 issue of the Meteorological Magazine, which includes an article on the minutes from a tropical meteorology discussion at the UK Met Office in late 1958 [Graystone, 1959]. Included

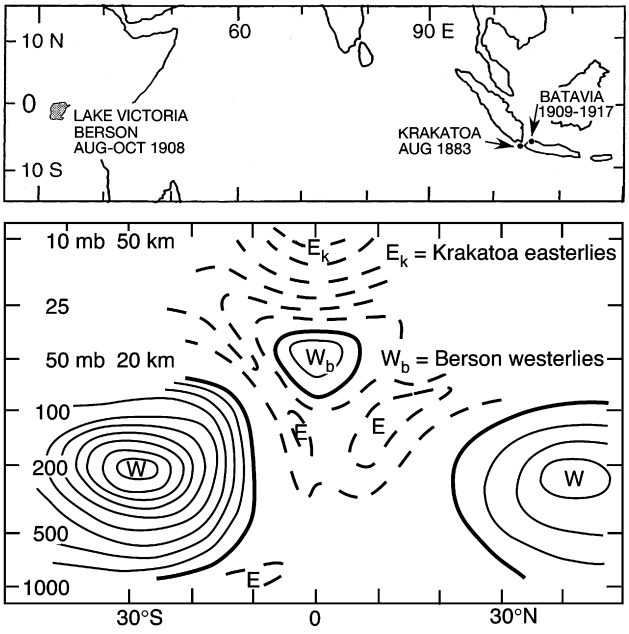

Figure 1.5: A schematic [Hastenrath, 2007] that shows the broad Western scientific consensus was for upper atmospheric circulation prior to the discovery of the QBO.

are the radiosonde observations over a period of two years by P. Graystone over Christmas Island (1.9°N), now known as Kiritimati, the largest island of the nation Kiribati. Graystone made the comment that "the absence of any annual cycle and the presence of very large shear values" were "noteworthy." (Figure 1.6) These observations were later recognized as the descending easterly and westerly regimes of the quasi-biennial oscillation.

Richard Reed of the University of Washington and Robert Ebdon of the UK Met Office did simultaneous but independent work describing the regime of stratospheric easterly and westerly equatorial winds seen in rawinsonde observations of upper air winds from Kanton Island (2.8°S, an atoll that is also part of Kiribati). Reed presented the work at the American Meteorological Society Boston meeting in January 1960 [Baldwin et al., 2001; Reed, 1960] and published it in a 1961 paper [Reed et al., 1961], along with supporting observations of Nairobi, Kenya (1.3°S), provided by the East African Meteorological Department. Ebdon concurrently published similar findings in 1960, ascribing a two year period to the oscillation [Ebdon, 1960]. With the inclusion of Graystone's Christmas Island data, data from Gan (The Maldives, 0.7°S), Aden (Yemen, 12.8°N), Guayaquil (Ecuador, 2.2°S), and many more locations, Ebdon and R.G.

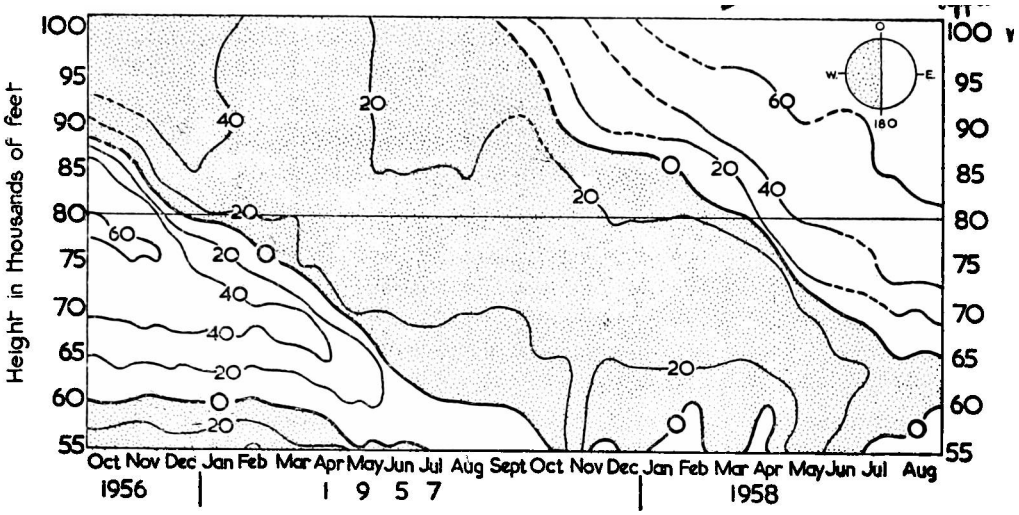

Figure 1.6: Zonal components of winds above the tropopause at Christmas Island using 10 day means. Taken by flight observation. Originally Figure 4 from [Graystone, 1959]

.

Veryard updated his estimate to a period of 23-29 months in the May 1961 Meteorological Magazine [Veryard and Ebdon, 1961]. The variety of locations used in Ebdon and Veryard's dataset allowed them to also describe the poleward decrease in amplitude of the oscillation. In 1963, J. K. Angell and J. Korshover of the U.S. Weather Bureau in Washington D.C. coined the term "quasi-biennial oscillation" to describe the phenomena recently discovered by their colleagues [Angell and Korshover, 1964]. The latter half of the 1960s was filled with many small steps forward, broadening scientific understanding of the most important traits of the QBO.

1.2.4 A historical note on tropical observations and discoveries

I want to acknowledge that, as is often the case in Western science, especially that which requires the observation of tropical phenomena, the work of the majority of people described above was not done in collaboration with the indigenous people of the lands on which the research and observations were performed [Salazar, 2014; Sammler and Lynch, 2021]. In other cases, the work was done with disdain for the Native peoples. In particular, I would like to include the following information include the following information about Sereno Bishop. Although Bishop was born in Honolulu in 1927, spending the majority of his life on the island

of Hawaii, he was the son of white Christian missionaries. He was a regular contributor to the Honolulu Advertiser, then known as the Pacific Commercial Advertiser, a publication known for their support of the 1893 illegal U.S. overthrow of the Hawaiian monarch her majesty Queen Lili'uokalani [Hawaii at Manoa, 2013]. In his writings, he asserted views of white supremacy over the native Hawaiian people. In one article, Bishop depicts the Hawaiian people, before the invasion of white Christian missionaries and colonizers, as "depressed serfs under oppressive and arrogant chiefs... deeply degraded in morals. Such was the barbarian depression of the Hawaiians when the Gospel of Christ arrived here to deliver and elevate them" [Bishop, 1904]. It is also important to note that there is always a possibility that discoveries made by the Western scientists mentioned above, in particular the observation of the nature of upper equatorial winds in the aftermath of volcanic eruptions, were preceded by indigenous science. It is very important that as we move forward, the work that we do in the Global South be done in Equitable Exchange with the communities that reside there, as outlined in Harris et al. [2021].

1.2.5 Development of a theory (1964-1982)

In 1987, Richard Lindzen published a paper entitled "On the Development of the Theory of the QBO" [Lindzen, 1987], that outlines the path of research and logic that went into the establishment of a working theory for the mechanism driving the QBO. Lindzen was a graduate student at Harvard in the early 1960s. His advisor, Richard Goody, suggested that the QBO was thermally forced because the photochemical relaxation time of ozone at 25 km in the tropics is about 26 months. Lindzen worked on this theory for his thesis topic and while a postdoctoral fellow at the University of Washington (UW) and then the University of Oslo. The published papers in 1964-1966 contributed to understanding of ozone photochemistry in the stratosphere, but without adequately accounting for a QBO mechanism [Lindzen and Goody, 1965; Lindzen, 1966a,b,c]. J. Michael Wallace of UW published a paper in 1967 [Wallace, 1967], arguing that the QBO could not be thermally forced at the equator because thermal forcing in the tropics would

induce vertical motion that would cancel the effect of the heating and that momentum sources were a more likely culprit.

While a research scientist at the National Center for Atmospheric Research (NCAR), Lindzen began developing the theory for the type of vertically propagating equatorial waves that would be required to transport the momentum necessary to drive the QBO [Lindzen, 1967]. Simultaneously but separately, Taroh Matsuno of the University of Tokyo made important contributions to the theory of waves on the equatorial β-plane using shallow water equations, which have equatorially trapped wave solutions [Matsuno, 1966].

This work eventually led to a collaboration (likely via snail mail) between Matsuno and Lindzen in [Lindzen and Matsuno, 1968], with a resulting paper published years before the two actually met in person. The paper describes the theory behind observations of vertically and westward propagating equatorial waves made by Taketo Maruyama and Michio Yanai, also of the University of Tokyo [Maruyama, 1967; Yanai and Maruyama, 1966]. These waves were eventually identified and characterized as mixed Rossby-gravity waves, also known as Yanai-Maruyama waves. More observations of equatorial waves were made throughout the latter half of the 1960s, including by Wallace and Vernon Kousky of UW, who observed Kelvin waves in tropical radiosonde data, with momentum fluxes large enough to drive westerly QBO accelerations [Wallace and Kousky, 1968]. The defining characteristics of Kelvin, mixed Rossby-gravity, and other equatorial waves will be outlined in the Appendix.

In 1968, Wallace and James Holton (also of UW) developed an initial hydrostatic & geostrophic model for the QBO, applying both thermal and dynamical forcing, which produced some aspects of alternating wind patterns, without the downward propagation seen in observations [Wallace and Holton, 1968]. In 1967, John Booker and Francis Bretherton at Cambridge described the mechanism of gravity wave momentum deposition in mean zonal flow at "critical levels" [Booker and Bretherton, 1967]. Critical levels are the altitudes at which the zonal phase speed of a wave matches the wind speed, where vertically propagating waves "break" and deposit their zonal momentum into the flow. Booker and Bretherton's breakthrough was the last

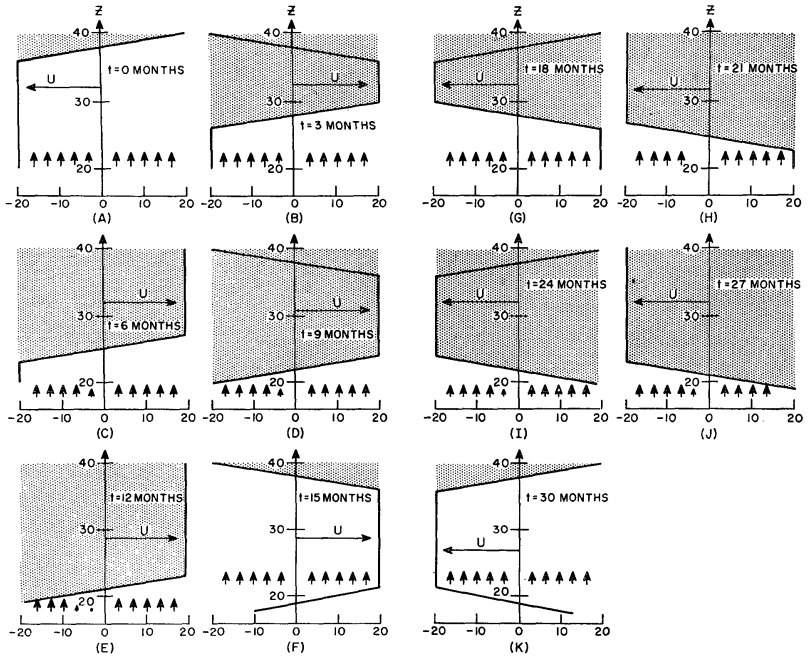

Figure 1.7: Figure 5 from [Lindzen and Holton, 1968]. Original caption: "A schematic time sequence illustrating the proposed theory of the QBO for the synchronous case at three-month intervals from 0-30 months, (a)-(k). Vertical arrows indicate gravity wave propagation."

piece of the puzzle needed by Lindzen and Holton [1968] (hereafter, LH68), which laid out the first successful model for the QBO, involving vertically propagating gravity waves interacting with the zonal wind and producing a long-period oscillation. Figure 1.7 of Lindzen and Holton [1968] shows a time progression of a vertically propagating gravity waves reaching a critical level and depositing momentum into the zonal flow, driving the zonal acceleration toward the phase speed of the waves.

In his 1971 paper, "Equatorial Planetary Waves in Shear," Lindzen describes the interaction of Yanai (or mixed Rossby-gravity) and Kelvin waves with the mean flow within LH68, and suggested that infrared radiation damps the waves, allowing for a continuous exchange of momentum with the mean flow [Lindzen, 1971]. This led to the updated QBO theory of Holton and Lindzen [1972] (HL72). In 1977, Alan Plumb, of the Commonwealth Scientific and Industrial Research Organisation (CSIRO) in Melbourne, Australia, produced a simple numerical model based on the theory of HL72, replacing the westerly Kelvin and easterly mixed Rossby-gravity waves with two gravity waves of opposite phase speeds, with added viscosity to damp the os-

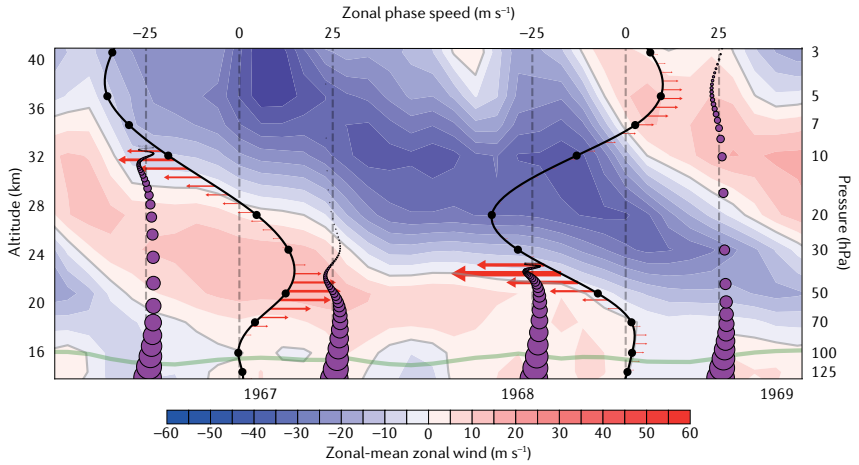

Figure 1.8: Figure from Box 2 in [Anstey et al., 2022]. "Shows an eastward wave propagating upwards in eastward wind shear and a westward wave propagating upwards in westward wind shear. The vertical wavelength and vertical group velocity of the wave both decrease as the wind speed approaches the wave phase speed with altitude. Dragging mean flow toward wave speed creates descending shear zones."

cillation [Plumb, 1977]. Figure 1.8 shows the canonical model of the QBO following Plumb [1977], taken from [Anstey et al., 2022]. It shows two upward propagating waves of opposite phase speeds propagating upward in shear zones of the same respective phase speed directions. Waves are dissipated by radiative damping and wave breaking due to convective and dynamic instability. Momentum is deposited, accelerating wind towards the phase speed of the waves.

Despite the growing literature describing the driving mechanism of the QBO, skepticism persisted some pockets of the scientific community. Much of that doubt was assuaged in 1978, when Plumb and Angus McEwan, also of CSIRO, produced a laboratory simulation of the wave-mean flow interaction driving the QBO. In a rotating tank of stratified saltwater, pistons disturb the lower boundary, forcing standing internal waves of opposite directions. In this configuration, they were able to produce a "a strong mean azimuthal circulation which itself exhibits a long-period oscillation" [Plumb and McEwan, 1978]. A digitized video of the experiment can be found here, showing one iteration of this experiment; small polystyrene spheres in the fluid allow the viewer to see the downward propagation of the shear zones. Over the next couple of years, Plumb and Robert Bell, also of CSIRO, created a three-dimensional numerical model of the QBO with Kelvin and mixed Rossby-gravity waves forced at the lower boundary, with ther-

mal and mechanical dissipation, producing a zonal wind oscillation with a slightly too long 1000-day period [Plumb and Bell, 1982b,a]. These papers, along with the work of Holton [1979] analyzed the latitudinal nature of the oscillation and the damping role of the meridional circulation in the momentum budget of the QBO.

1.2.6 Refining understanding of drivers, impacts & mechanism (1985-present)

In 1985, Hiroshi Tanaka and Nobuyaki Yoshizawa of Nagoya University were able to expand upon the work of Plumb and McEwan (Figure 1.8), allowing the forced waves to evolve in space and time, studying the impact on the resulting oscillation, increasing the period and changing the wave speeds of different types of waves differently [Tanaka and Yoshizawa, 1985].

In 1989, Lesley Gray (Rutherford Appleton Laboratory) and John Pyle (Cambridge University) produced a 2D model of the QBO that also modeled the ozone signal; the ozone response to the QBO is discussed in section 1.3. Gray and Pyle were also able to establish that existing observations of Kelvin and Rossby-gravity waves do not produce enough momentum flux to produce a QBO [Gray and Pyle, 1989]. In 1990, R. Saravanan (Princeton University) generalized and extended the canonical model of the QBO to include multiple waves. In this same publication, he showed that greater wave forcing would be needed to force the downward propagation of the QBO due to tropical upwelling from the Brewer Dobson circulation (BDC) [Saravanan, 1990]. Extending upon this work in 1997, Dunkerton was able to determine that, with tropical upwelling from the BDC, the flux needed to force the QBO must be 2-4 times the current observations of planetary-scale equatorial waves. This meant that inertia-gravity waves and small-scale gravity waves must also contribute to the necessary wave driving [Dunkerton, 1997].

In 1990, Timothy Dunkerton (Northwest Research Associates) provided evidence for a seasonal preference for the onset of the easterly phase of the QBO–typically in the northern hemisphere late Spring. We revisit and reanalyze the work from Dunkerton [1990] in the Appendix.

In 1996, Masaaki Takahashi, of the University of Tokyo, produced the first QBO-like oscillation in a global climate model (GCM) by fine tuning parameters. The resulting oscillation had an amplitude of similar magnitude to observations, but a period of only 18 months, instead of the observed 28 [Takahashi, 1996, 1999]. In the following years, other GCMs produced QBO-like oscillations, also with unreasonable periods and amplitudes, or with radiative parameters tuned outside the scope of reality [Hamilton et al., 1999; Horinouchi and Yoden, 1998]. Adam Scaife and others at the UK Met Office (UKMO) showed that in order to simulate a realistic QBO, the simulation needed to include a parameterization of the contribution from sub-grid scale waves. He also showed that the period of the simulated QBO was sensitive to the quantity of wave forcing, which varied between models [Scaife et al., 2000]. Marco Giorgetta, at Max Planck Institute, produced a realistic QBO in MAECHEM with a combination of increased vertical resolution, parameterized convection, and parameterized gravity wave drag. These experiments showed that a realistic QBO requires a vertical resolution of 1 kilometer or less [Giorgetta et al., 2002].

Between 2018-2022, a series of papers were published as a result of the SPARC (Stratosphere-troposphere Processes And their Role in Climate) QBO-i initiative, evaluating large-scale earth system models and their representation of the QBO. Andrew Bushell, of UKMO, reported that in the years since Takahashi's first successful simulation, most large scale earth system models were able to produce a QBO that reasonably imitates observations. The problems that persist as of 2023 include a period that is a bit shorter than the observed 28 months. Amplitudes are reasonable in the upper stratosphere ($\sim$ 10 hPa), but are only about half of the observed magnitude in the middle and lower stratosphere ($\sim$ 50-70 hPa) [Bushell et al., 2022]. Realistic QBO simulations require both the realistic generation of resolved-scale equatorial planetary waves, as well as a parameterization that produces realistic gravity wave flux and drag. The variation in these two requirements between models produced the spread of model output [Butchart et al., 2018]. Also a part of the SPARC QBO-i initiative, Yaga Richter (NCAR) and colleagues performed experiments analyzing the QBO response to doubled and quadrupled atmospheric

carbon dioxide concentrations . All models predicted a decrease in the amplitude of the QBO, averaging to a 36% decrease under doubled CO_2 and a 51% decrease under the quadrupled CO_2 scenario, both as a result of increased gravity wave momentum flux entering the stratosphere and tropical vertical residual velocity. Between the eleven models studied, there was no consistency in the QBO period response [Richter et al., 2022].

There are numerous gravity wave parameterizations utilized in global climate models [Beres, 2005; Choi and Chun, 2011; Xue et al., 2012]. Efforts to improve these parameterizations and refine the choice of source parameters have involved incorporating observations and reanalysis estimates of the flux due to gravity waves. Others have utilized hindcasts within numerical weather prediction systems to optimize the choice of gravity wave source parameters [Barton et al., 2019]. In 2005, Joan Alexander (UW) and Leonhard Pfister, of NASA Ames Center, published some of the first observational evidence for convectively generated high frequency gravity waves found in flight data Alexander and Pfister [1995]; Alexander et al. [1995].

In the last two decades, there have been studies performed on reanalysis datasets with the goal of quantifying wave forcing in observations, as the relative contribution of various wave types to the QBO remained poorly constrained. Before this time, there were no high resolution long-term global measurements in the stratosphere. In 2005, Charlotte Pascoe (Rutherford Appleton Laboratory) and colleagues at the University of Reading, Oxford, and Northwest Research Associates, analyzed ECMWF Reanalysis 40 in the context of the QBO. They were able to show that the descent rate of the westerly shear zone ($\sim$ 4 hPa per month) is approximately twice as fast as that of the easterly shear zone ($\sim$ 2 hPa per month) [Pascoe, 2005].

Between 2009 and 2014, Manfred Ern and Peter Preusse (both of Forschungszentrum Julich in Germany) published Kelvin wave momentum flux estimates based on temperature satellite data, finding that Kelvin wave forcing peaked close to 0.2 m s^{-1} per day, making up about 30-50% of the observed QBO phase transition forcing and 20-35% of the expected total wave forcing [Ern and Preusse, 2009a,b; Ern et al., 2011]. Good agreement was found [Geller et al., 2013] when these satellite observations were compared to ERA-40 [Uppala et al., 2005] and ERA-Interim

[Dee et al., 2011]. The "missing" drag from ERA-Interim (on height levels), that they attributed to gravity wave momentum flux, was found to be larger than planetary wave drag in the easterly shear zone and comparable in contribution in the westerly shear zone [Ern et al., 2011, 2014].

In 2015, Y.-H. Kim and H.-Y. Chun (Yonsei University) calculated momentum forcing of the QBO due to equatorial waves using ERA-Interim and other reanalysis datasets, comparing pressure-level and model-level data. They found that in westerly shear zones at 30 hPa, Kelvin waves produce 3-9 m s^{-1} per month of the total equatorial wave forcing to the QBO (3-11 m s^{-1} per month), which dominates over the contribution from small-scale gravity wave forcing. In easterly shear zones at 30 hPa, the total equatorial wave forcing is 1-5 m^{-1} per month, with the contribution from unresolved waves dominating. When these results (which were on pressure levels) were compared with native model-level data, they make the argument that Kelvin wave forcing is underestimated by 2-4 m^{-1} per month [Kim and Chun, 2015b]. In 2020 and 2021, Hamid Pahlavan (UW) performed a similar analysis with ERA5 reanalysis [Hersbach et al., 2020], producing similar but refined results [Pahlavan et al., 2020, 2021]. As we will discuss in the following sections, we will perform similar analyses to Ern et al. [2014]; Kim and Chun [2015b] and Pahlavan et al. [2020] with ERA-Interim on isentropic levels in order to quantify the contribution of unresolved wave forcing to the QBO.

1.3 The Importance of the QBO in the Global Circulation

1.3.1 Signal of the quasi-biennial oscillation in other variables

Signal of the QBO in Temperature

By way of thermal wind balance, the vertical wind shear pattern of the QBO induces an analogous QBO in the equatorial stratospheric temperature signal [Baldwin et al., 2001] (Figure 1.9 from NASA (GSFC)). The amplitude of the temperature QBO maximizes at 4K between 30-50 hPa, with cold anomalies correlating with the easterly phase of the QBO. The temperature signal diminishes to +/- 0.5-1 K at the tropical tropopause [Anstey et al., 2022; Tegtmeier et al., 2020]. This signal is the result of thermal wind balance, which occurs as a result of both hydrostatic

and geostrophic balance. In pressure vertical coordinates, thermal wind balance is expressed in component form by:

$$f\frac{\partial u_g}{\partial p} = \frac{R}{p}\frac{\partial T}{\partial y} \tag{1.1}$$

and

$$-f\frac{\partial v_g}{\partial p} = \frac{R}{p}\frac{\partial T}{\partial x}, \tag{1.2}$$

where R is the dry air gas constant and f is the Coriolis parameter. u_g and v_g represent the geostrophic wind, which is the theoretical wind that would result from a balance between the apparent Coriolis force and the pressure gradient force.

Definitions 1.1 and 1.2 imply that an increase in zonal wind with decreasing pressure produces a negative rate of change in temperature in zonal space.

Secondary meridional circulation

Maintaining thermal wind balance requires a secondary residual meridional circulation with ascent at the Equator in the regions of westward vertical shear and descent in regions of eastward vertical shear [Butchart, 2022]. Figure 1.10 shows a schematic illustration from [Butchart, 2022] of this secondary meridional circulation. As an example for the easterly phase of the QBO, the zonal wind acceleration induces ascent through the tropopause, in additional to tropical upwelling, and descent in the middle and upper stratosphere [Baldwin et al., 2001].

Ozone QBO

As a result of the secondary meridional circulation, there are ozone anomalies correlating to the QBO on the order of ± 1.5ppm, with negative anomalies occurring with the QBO-E phase and vice versa. The sign of the ozone signal changes at 15 hPa due to catalytic ozone loss from NO_x [Anstey et al., 2022]. There is an out of phase QBO in higher latitudes (Figure 1.11).

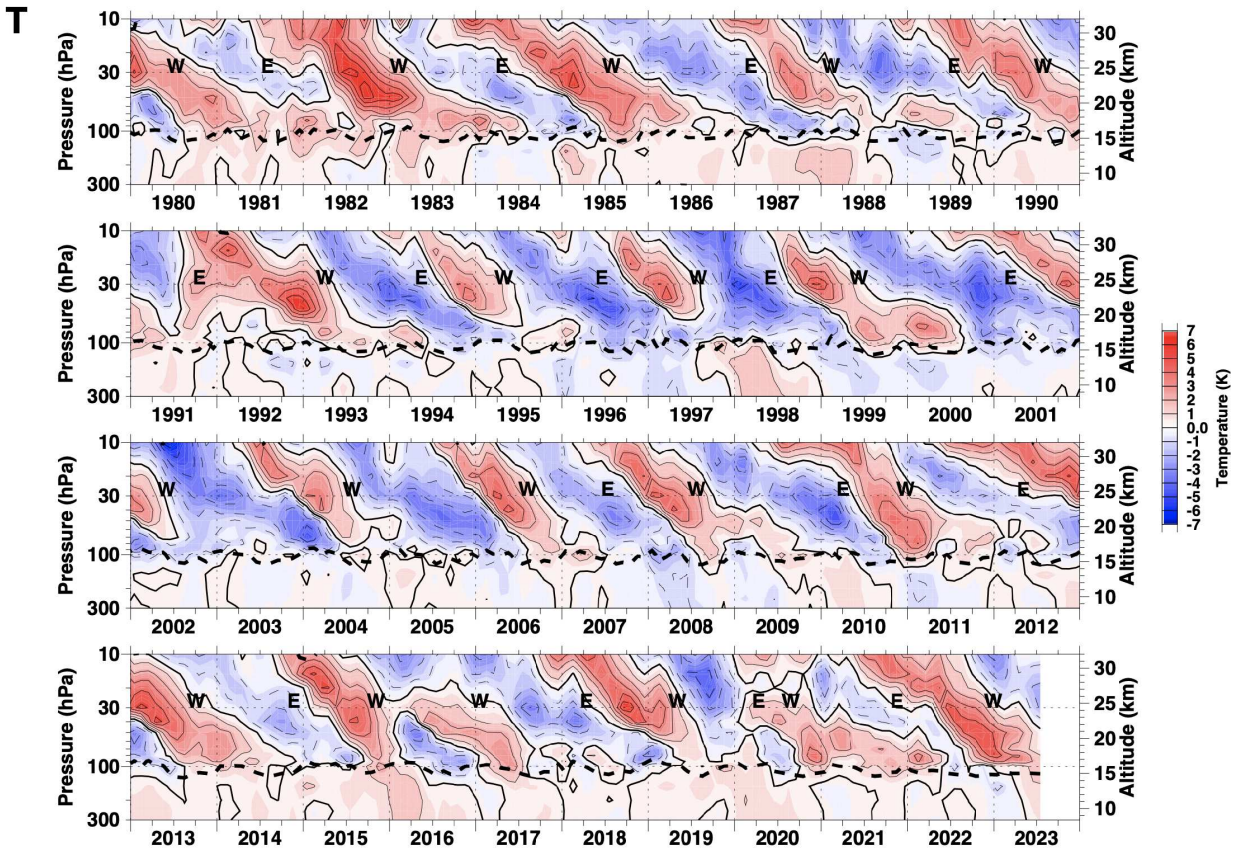

Figure 1.9: Time series of QBO monthly mean temperature from Singapore sonde. Temperature data is detrended, deseasonalized, and smoothed with a 1-2-1 Gaussian filter. The thick dotted line shows the tropopause calculated from the thermal lapse rate. Units are Kelvin.

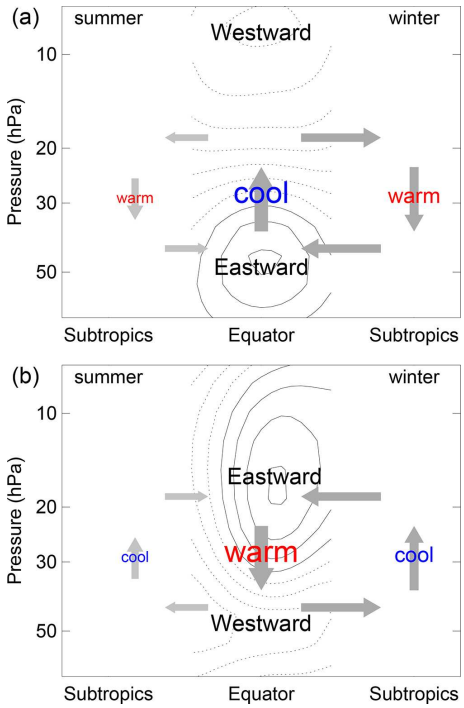

Figure 1.10: Figure 12 from [Butchart, 2022]. Caption: "Schematic showing the secondary residual meridional circulation (grey arrows) associated with the QBO equatorial temperature anomalies and the asymmetry in the circulation between the summer and winter hemispheres. The locations of the warm and cool anomalies are shown in red and blue, respectively, with the font size giving a qualitative guide to the strength of the anomalies. Solid (dotted) contours indicate eastward (westward) zonal mean zonal winds at intervals of 10 m s^{-1} starting at $\pm 5 ms^{-1}$ for (a) westward shear zone and (b) eastward shear zone. After Fig. 1 from Plumb and Bell (1982)."

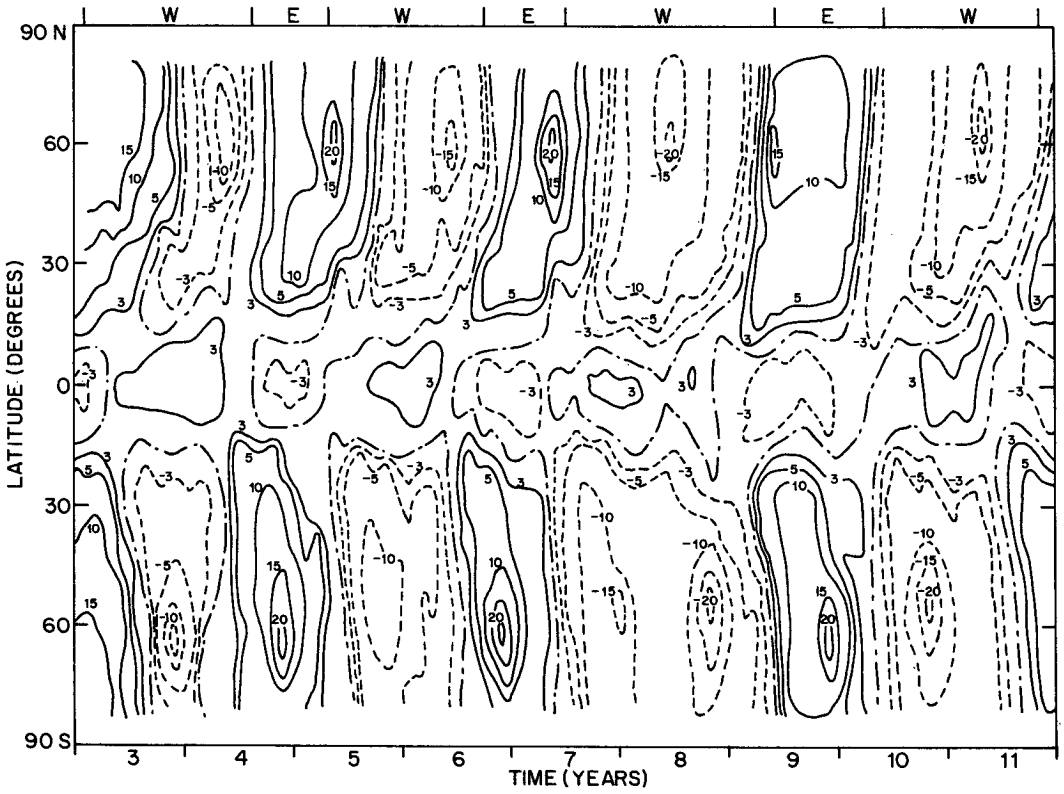

Figure 1.11: Figure 7 from Gray and Pyle [1989]. Original caption: "Latitude-time section of the modeled column ozone anomaly (Dobson Units) from run 1. (The appropriate monthly mean averaged over the whole of the model run has been subtracted in order to obtain the anomaly.) The model data points have been passed through a 1-2-1 filter. The direction of the equatorial wind at approximately 50 mb is indicated at the top of the figure."

1.3.2 QBO Teleconnections

The stratospheric tropical circulation can have important effects on global surface climate variability. Figure 1.12 provides a schematic indicating QBO teleconnections and their pathways. Below is a short summary of some of the most important teleconnections.

Stratospheric Polar Vortex

During the easterly phase of the QBO, polar vortex winds are stronger by approximately 5-10 m/s in the Northern Hemisphere, and vice versa for the westerly phase. This allows the vortex to be more susceptible to vortex disruptions and sudden stratospheric warmings [Anstey et al., 2022]. One proposed mechanism for this coupling is referred to as the Holton-Tan Mechanism, as was first described in 1980 by Holton and Hsiu-Chi Tan (UW) [Holton and Tan, 1980]. The surface on which the zonal mean zonal wind reaches zero with an increase in latitude is referred to as the zero-wind line. The easterly phase of the QBO produces a shift in the zero-wind line towards higher latitudes. This limits the quantity of waves breaking and depositing their momentum into the flow of lower latitudes, confining wave activity to higher latitudes, and thus, the polar vortex, weakening its maximum wind speed.

The SAO

The stratospheric semi-annual oscillation (SAO) is a signature in temperature and zonal wind in the upper stratosphere, with an easterly phase beginning at the stratopause during northern winter and a westerly phase during southern winter [Garcia et al., 1997; Dunkerton and Delisi, 1997]. The seasonal movement of the sun over the Equator, in congruence with wave-mean flow interaction, generate the SAO Mayr et al. [2010].

While QBO westerly zones can originate in the upper stratosphere without an SAO westerly shear zone [Holton and Lindzen, 1972; Plumb, 1977; Plumb and McEwan, 1978; Mayr et al., 2010], they are more likely to be generated in the presence of a westerly shear zone of the SAO. When the westerly phase of the QBO is in the lower stratosphere and diminishing in strength, waves transporting westerly momentum are more likely to penetrate past the lower strato-

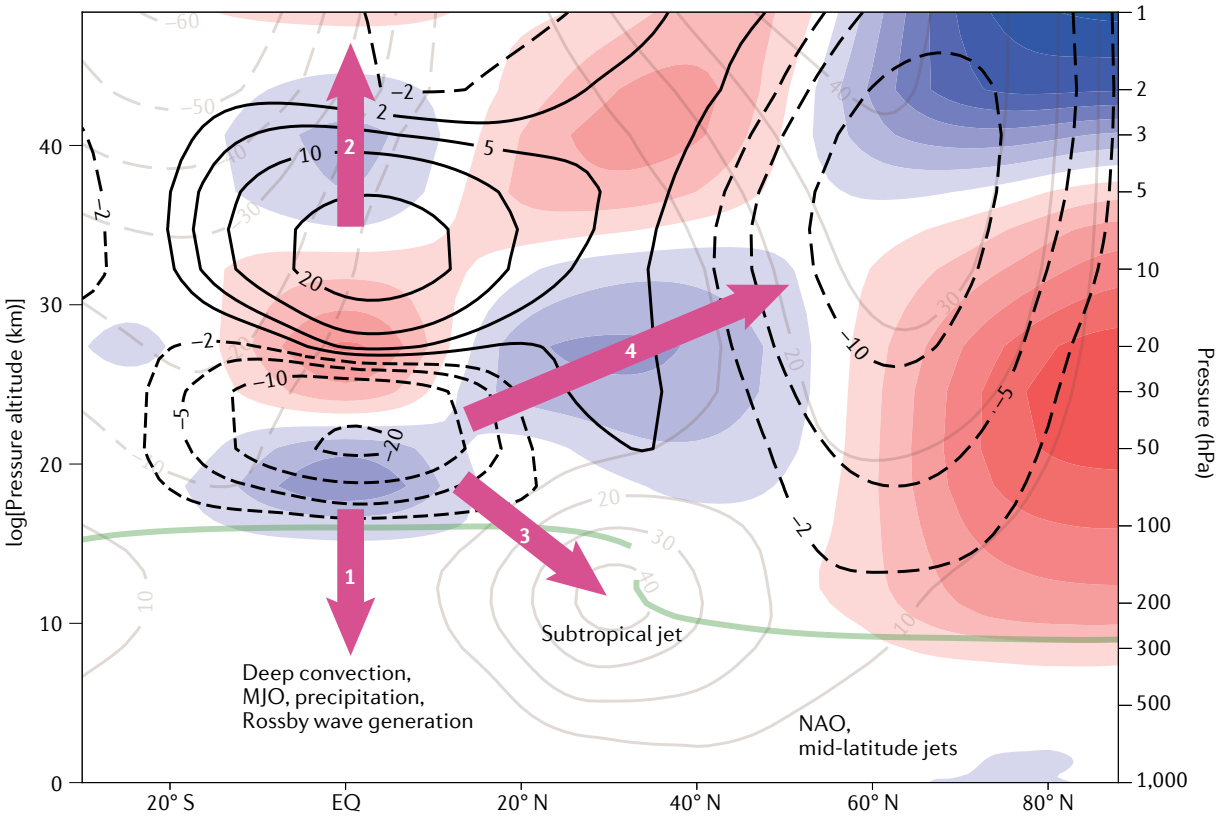

Figure 1.12: Figure 2 from Anstey et al. [2022]. Original caption: "Global QBO teleconnections and their pathways. January difference between westward and eastward QBO composites for 1958–2016 using the JRA-55 reanalyses, defining QBO phase by 50 hPa equatorial wind (westward minus eastward). Black contours represent zonal-mean zonal wind difference (westward dashed, eastward solid, units of metres per second), filled contours represent zonal-mean temperature difference (warmer is indicated by red and colder by blue, 1 K contours starting at ±0.5 K). Also shown are the January climatogical zonal-mean zonal wind (light brown contours, zero contour omitted, units of metres per second) and thermal tropopause (light green). Numbered arrows (purple) indicate pathways for QBO influence by modulating tropical tropopause temperature or wind (pathway 1), filtering upwards-propagating waves that reach the SAO near the stratopause and above (pathway 2), modulation of the subtropical jet by the QBO secondary circulation (pathway 3), and modulating planetary-scale waves that distort the stratospheric polar vortex (pathway 4)."

sphere, ascending to the upper stratosphere, where the SAO is active, before reaching their critical level [Pahlavan et al., 2021]. Deposition of westerly momentum by breaking waves tends to be focused in the westerly shear zones of the SAO, allowing stronger westerly shear zones of the SAO that can propagate downward into the middle and lower stratosphere. This creates conditions for which the westerly shear zones of the SAO can transition a westerly shear zones of the QBO. [Wallace, 1973; Dunkerton and Delisi, 1985; Garcia et al., 1997; Krismer et al., 2013].

Subtropical jets

The QBO regulates seasonal signals in the subtropical jet and sea-level pressure over the oceans. During the easterly phase of the QBO, the subtropical jet shifts poleward during the northern hemisphere early and late winter [Garfinkel and Hartmann, 2011; Wang et al., 2018]. The poleward shift of the subtropical jet is a result of the subtropical zonal wind response associated with the QBO-induced secondary meridional circulation, described in the previous section [Anstey et al., 2022].

The tropical troposphere

There is evidence of a few different QBO-related signals in the tropical troposphere. When the QBO is in the easterly phase at 70 hPa, there is an observed increase in precipitation in the western tropical Pacific and a southward shift of the Intertropical Convergence Zone (ITCZ) [Gray et al., 2018; Son et al., 2017]. This particular signal is difficult to study because it requires disentangling the impact of the El Nino Southern Oscillation (ENSO) from the data.

A possible relationship exists between the Madden Julian Oscillation (MJO) and the QBO. Since 1980, the MJO has been shown to be 40% stronger and to persist roughly 10 days longer during the Northern Hemisphere Winter when the QBO is in its easterly phase at 50 hPa [Son et al., 2017; Martin et al., 2021]. There is evidence to suggest that the QBO signal in temperature induces a tropospheric convection response, which is a proposed mechanism for the MJO-QBO relationship. The stratospheric cooling resulting from increased greenhouse gas concentrations in the atmosphere is a proposed explanation for the lack of signal in observations until 1980

[Martin et al., 2021]. If this teleconnection continues to prove robust in future work, it would be a helpful tool for subseasonal prediction.

1.4 Motivation & Goal

1.4.1 Motivation

There is evidence that many different types of waves contribute to the driving of the QBO, including equatorially trapped Kelvin and mixed-Rossby gravity waves, inertia-gravity waves, and small-scale gravity waves from both orographic and convective sources. The precise mix of waves that drive the QBO is still uncertain. The relative contributions of different wave types impact details such as its strength, period, and vertical extent, which are all crucial to simulate a realistic QBO [Anstey et al., 2022]. It is important to successfully simulate the QBO, as it is an important source of predictability across the climate system on subseasonal to seasonal timescales Nardi et al. [2020]. Reducing the uncertainty of the relative importance of forcing contributions by different wave types is also important in order to better understand how the QBO will respond to climate forcing–in particular, its response to greenhouse gas forcing [Richter et al., 2022]. Over the last few decades, it has become increasingly clear that small-scale convectively generated gravity waves make a significant contribution to the wave driving of the QBO [Dunkerton, 1997; Alexander and Holton, 1997; Garcia et al., 1997; Ern et al., 2014; Kim and Chun, 2015a]. It is particularly difficult to quantify the vertical momentum fluxes associated with small-scale gravity waves because they are unresolved in reanalysis datasets [Pahlavan et al., 2020; Ern et al., 2014]. We employ an indirect method to further quantify the contributions of unresolved waves to the driving of the QBO.

1.4.2 Goal

We aim to quantify the angular momentum fluxes from unresolved convectively generated gravity waves, as well as their contributions to the acceleration of the stratospheric equatorial zonal wind, by post processing re-analysis data.

We first consider the flux form of the mass continuity equation in isentropic coordinates. We directly compute zonal and meridional mass flux divergence and the time tendency of the zonally averaged pseudodensity, leaving the vertical mass flux divergence as the residual. We vertically integrate to get vertical mass flux. We analyze these various components of the mass budget to confirm the mass circulation of the QBO. In isentropic coordinates, when we divide the vertical mass flux by pseudodensity, we can compute the heating rate and analyze its seasonality and relationship to the QBO.

We then use a zonally averaged flux form of the conservation of angular momentum equation in spherical horizontal coordinates and potential temperature (or isentropic) vertical coordinates. We convert this equation to an advective form, utilizing Eliassen-Palm flux (defined in the next chapter), separating eddy and zonal mean circulation of angular momentum, allowing separation of the mass flow from the angular momentum flow to some extent. We directly compute absolute angular momentum tendency, meridional and vertical advection, meridional Eliassen-Palm flux divergence, and components of vertical Eliassen-Palm flux divergence due to heating (utilizing the heating rate found in the mass budget analysis) and isentropic form drag (also defined in the next section). This leaves a residual of vertical Eliassen-Palm flux divergence, which can be integrated to obtain the vertical fluxes due to unresolved wave forcing, with mostly contributions from small-scale convectively generated gravity waves.

The advantage of angular momentum as an alternative for zonal wind is that there are no Coriolis or metric terms in the angular momentum equation, so when moving across latitudes, the only process to consider is advection of angular momentum. We use meridional angular momentum fluxes to determine the vertical.

We have the goal of identifying areas for improvement in reanalysis datasets generally, and ERA-Interim, as well as just considerations to keep in mind when working with reanalyses. We also discuss these results within the context of the reliability of reanalysis datasets and the downsides to treating reanalysis data as observations. We consider what aspects of the results

of this analysis are not based in reality. Stratospheric observations are not made everywhere, and the tropics are not very well-populated.

We also analyze the seasonal cycles of resolved and unresolved angular momentum fluxes, as well as their potential links to the onset of QBO phase reversals. We also provide evidence in general support of a previously reported preference for the onset of the easterly phase of the QBO to occur during Northern Hemisphere spring.

Chapter 2

Background

2.1 Isentropic Coordinates

Many vertical coordinates can be used to analyze atmospheric motions–these include height, pressure, and others. One vertical coordinate that has advantageous properties for this analysis is potential temperature, θ, which is a function of the entropy. In general, vertical coordinates need to vary monotonically with height, and this is largely true with isentropic coordinates because potential temperature increases with height in almost all instances. In our analysis, we utilize ECMWF Reanalysis Interim (ERA-I) isentropic analysis, which will be discussed and defined in section 3.1. ERA-I is interpolated to 15 isentropic levels from the original 37 model levels. This poses some disadvantages, but isentropic surfaces do allow for variable vertical resolution in height, producing a higher resolution in regions where isentropic surfaces are packed [Hsu and Arakawa, 1990]. One issue with this coordinate is that coordinate surfaces intersect the bottom boundary, but this allows for the treatment of these intersecting layers as "massless," which makes it easier to account for topography, as these layers conform to the lower boundary [Hsu and Arakawa, 1990]. Figure 2.1 from [Hsu and Arakawa, 1990] shows an example of the way the "massless layer" tactic is employed. According to [Egger et al., 2007], isentropic coordinates are not usually used in angular momentum analysis, despite their advantages, which will become clear in the following sections.

The most important advantage of isentropic coordinates is that under adiabatic processes, mass can not cross isentropic surfaces, allowing a semi-Lagrangian perspective when analyzing atmospheric circulation. Another advantage is that the vertical flux of mass is proportional to the heating rate, which functions as the vertical motion variable.

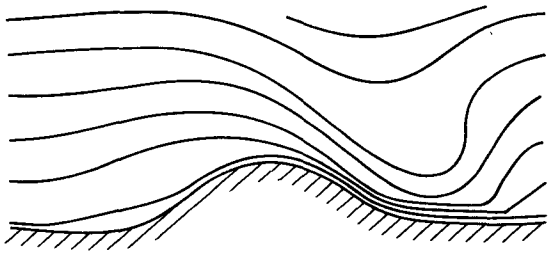

Figure 2.1: Figure 2 from [Hsu and Arakawa, 1990]. Original caption: "Illustration of massless layers along the lower boundary."

2.2 Mass budget

Mass continuity in isentropic coordinates is expressed by

$$\frac{\partial \rho_\theta}{\partial t} + \nabla \cdot \left(\rho_\theta \vec{V}\right) + \frac{\partial}{\partial \theta}\left(\rho_\theta \dot{\theta}\right) = 0. \tag{2.1}$$

The pseudodensity, ρ_θ, is defined by

$$\rho_\theta = \frac{-1}{g}\frac{\partial p}{\partial \theta}. \tag{2.2}$$

Expanding 2.1 in spherical coordinates

$$\frac{\partial \rho_\theta}{\partial t} + \frac{1}{a\cos\varphi}\frac{\partial}{\partial \varphi}\left(\rho_\theta v \cos\varphi\right) + \frac{1}{a\cos\varphi}\frac{\partial}{\partial \lambda}\left(\rho_\theta u\right) + \frac{\partial}{\partial \theta}\left(\rho_\theta \dot{\theta}\right) = 0. \tag{2.3}$$

Here,

$$\begin{aligned}
\frac{\partial \rho_\theta}{\partial t} &= \text{time tendency of pseudodensity} \\
\frac{1}{a\cos\varphi}\frac{\partial}{\partial \lambda}\left(\rho_\theta u\right) &= \text{zonal mass flux divergence} \\
\frac{1}{a\cos\varphi}\frac{\partial}{\partial \varphi}\left(\rho_\theta v \cos\varphi\right) &= \text{meridional mass flux divergence} \\
\frac{\partial}{\partial \theta}\left(\rho_\theta \dot{\theta}\right) &= \text{vertical mass flux divergence.}
\end{aligned}$$

Equation 2.3 can be used to solve for the vertical mass flux, which is proportional to the vertical heating rate, $\dot{\theta}$. This is one of the advantages of the use of isentropic coordinates in our analysis. Vertical velocity in reanalysis has historically been poorly constrained.

Zonally averaging 2.1 and simplifying, we obtain:

$$\frac{\partial \overline{\rho_\theta}^{\lambda}}{\partial t} + \frac{1}{a\cos\varphi}\frac{\partial}{\partial \varphi}\left(\overline{\rho_\theta v}^{\lambda}\cos\varphi\right) + \frac{\partial}{\partial \theta}\left(\overline{\rho_\theta \dot{\theta}}^{\lambda}\right) = 0, \tag{2.4}$$

where the notation for the zonal average of a scalar A is $\overline{A}^{\lambda}$.

In a *sufficiently long* temporal average of Equation 2.4, the time tendency of pseudodensity becomes negligible, and we get Equation 2.5:

$$\frac{1}{a\cos\varphi}\frac{\partial}{\partial \varphi}\left(\overline{\rho_\theta v}^{\lambda,t}\cos\varphi\right) + \frac{\partial}{\partial \theta}\left(\overline{\rho_\theta \dot{\theta}}^{\lambda,t}\right) = 0. \tag{2.5}$$

This equation implies that without heating, there cannot be any time and zonally averaged meridional mass flow on isentropic surfaces.

2.3 Angular momentum budget

The angular momentum of an air parcel in Earth's atmosphere, $\vec{L}$, is:

$$\vec{L} = \vec{r} \times \vec{V} \tag{2.6}$$

in which

- $\vec{r}$ = the position vector of the parcel from the origin, or the center of the Earth in our case.
- $\vec{V}$ = the velocity vector of the parcel, which must also in our case include the velocity of Earth's rotation

The components of $\vec{L}$ include an axial component, which points in the direction of the Earth's axis of rotation, as well as two components in the equatorial plane. The angular momentum of the atmosphere is dominated by the axial component, which includes the rapid

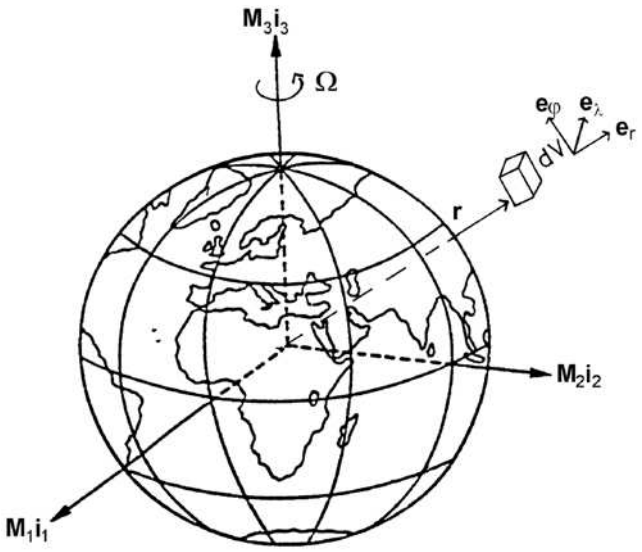

Figure 2.2: Figure 1 from [Egger et al., 2007]. "Rotating Earth and the components $M_i \mathbf{i}_i$ global angular momentum $\vec{M}$ in the rotating coordinate system with basic vectors $\mathbf{i}_i$. The position vector $\vec{r}$ points to a volume element dV in space, where the unit vectors $\vec{e}_\lambda$, $\vec{e}_\varphi$, and $\vec{e}_r$ of the local rotating spherical coordinate system are defined."

rotation of the Earth, which is much stronger than other rotational motion, so we focus on that component in our analysis. The component of angular momentum per unit mass that points in the direction of the Earth's axis of rotation is given by:

$$M \equiv a\cos\varphi\left(u + \Omega a\cos\varphi\right), \tag{2.7}$$

in which:

- $ua\cos\varphi$ = angular momentum due to the rotation of the atmosphere,
  or *relative* angular momentum
- $\Omega a^2\cos^2\varphi$ = angular momentum due to the rotation of the solid earth

Figure 2.2, from [Egger et al., 2007], shows a diagram of the rotating Earth with the components of angular momentum. M_3 in this diagram corresponds with M from Equation 2.7.

Conservation of angular momentum in isentropic coordinates is expressed by:

$$\frac{\partial}{\partial t}(\rho_\theta M) + \nabla \cdot (\rho_\theta \vec{V} M) + \frac{\partial}{\partial \theta}(\rho_\theta \dot{\theta} M + X) = -\rho_\theta \frac{\partial s}{\partial \lambda}, \tag{2.8}$$

in which

F_u = vertical flux of zonal momentum due to small scale eddies (convection and turbulence)

$X = F_u a \cos\varphi$ = vertical flux of *angular* momentum due to due to

small scale eddies (convection and turbulence)

s = dry static energy, also called the Montgomery potential

$-\rho_\theta \frac{\partial s}{\partial \lambda}$ = the pressure-gradient force

Zonally averaging 2.8 produces:

$$\frac{\partial}{\partial t}(\overline{\rho_\theta M}^\lambda) + \frac{1}{a\cos\varphi}\frac{\partial}{\partial \varphi}(\overline{\rho_\theta v M \cos\varphi}^\lambda) + \frac{\partial}{\partial \theta}(\overline{\rho_\theta \dot{\theta} M}^\lambda + \overline{X}^\lambda) = -\overline{\rho_\theta \frac{\partial s}{\partial \lambda}}^\lambda. \tag{2.9}$$

Assuming hydrostatic balance, the following relationship is true [Klemp and Lilly, 1978]:

$$\overline{-\rho_\theta \frac{\partial s}{\partial \lambda}}^\lambda = \frac{\partial}{\partial \theta}\left(p\overline{\frac{\partial z}{\partial \lambda}}^\lambda\right) \tag{2.10}$$

This allows us to write 2.9 in the following way:

$$\frac{\partial}{\partial t}(\overline{\rho_\theta M}^\lambda) + \frac{1}{a\cos\varphi}\frac{\partial}{\partial \varphi}(\overline{\rho_\theta v M \cos\varphi}^\lambda) + \frac{\partial}{\partial \theta}(\overline{\rho_\theta \dot{\theta} M}^\lambda + \overline{X}^\lambda - p\overline{\frac{\partial z}{\partial \lambda}}^\lambda) = 0. \tag{2.11}$$

In 2.11, the last three terms represent various components of vertical angular momentum flux divergence:

Vertical angular momentum flux due to heating and advection:

$$\overline{\rho_\theta \dot{\theta} M}^\lambda. \tag{2.12}$$

Vertical angular momentum flux due to friction at the surface and turbulence above the surface:

$$\overline{X}^{\lambda} = \overline{F_u}^{\lambda} a \cos\varphi. \tag{2.13}$$

Vertical angular momentum flux divergence due to orographic and isentropic form drag, (at the surface and above the surface, respectively):

$$\overline{-p\frac{\partial z}{\partial \lambda}}^{\lambda}. \tag{2.14}$$

A physical interpretation of isentropic form drag will be given in the following section. Isentropic coordinates provide a quasi-Lagrangian view of the circulation, which means that in an adiabatic process, pressure torque and frictional stress are the only vertical angular momentum flux [Hsu and Arakawa, 1990].

2.4 Surface Torque & Isentropic Form Drag, etc.

2.4.1 Isentropic form drag

Expression 2.14 represents isentropic form drag above the surface. Isentropic form drag is a vertical exchange of angular momentum when a drag force is produced by atmospheric motions across uneven isentropic surfaces. These occur when various pockets of warm and cold temperatures exist across the same pressure surface or height surface. They can be thought of as "mountains" of air, bounded by θ-surfaces. The pressure gradient produces a net force at a given level. Isentropic form drag is associated with eddies, such as baroclinic waves, equatorial waves, and orographic and convectively generated gravity waves. The isentropic form drag is strong in the midlatitudes in areas of baroclinic instability, where it transports angular momentum downward.

2.4.2 Mountain torque and surface friction

When vertical angular momentum flux divergence is integrated downwards to the surface, the terms contributing to the vertical angular momentum flux are mountain torque and surface friction. The mountain torque at the surface is analagous to the isentropic form drag term above the surface, replacing a mountain of air with a physical mountain. As air flows across a mountain range, pressure builds up on the upwide side of the mountain, creating a high pressure region, and an area of lower pressure is produced on the downwind side, producing a pressure force. The mountain exerts an equal and opposite force against the flow, creating drag. Surface friction produces additional drag, allowing for the transfer of angular momentum between the atmosphere and the ocean-solid Earth system.

2.5 Isentropic EP Flux

This section utilizes theory and derivations from Andrews [1983]; Andrews and McIntyre [1976]; Andrews [1978, 1987] and Randall [2015]. The tendency term of the mass-weighted angular momentum (from Equation 2.11) can be decomposed in the following way:

$$\frac{\partial}{\partial t}\left(\overline{\rho_\theta M}^\lambda\right) = \frac{\partial}{\partial t}\left(\overline{\rho_\theta}^\lambda \overline{M}^\lambda\right) + \frac{\partial}{\partial t}\left(\overline{\rho_\theta {}^* M^*}^\lambda\right). \tag{2.15}$$

Substituting 2.15 into the zonally averaged equation for conservation of angular momentum (Equation 2.11):

$$\begin{aligned} &\frac{\partial}{\partial t}\left(\overline{\rho_\theta}^\lambda \overline{M}^\lambda\right) + \frac{1}{a\cos\varphi}\frac{\partial}{\partial \varphi}\left(\overline{\rho_\theta v M}^\lambda \cos\varphi\right) \\ &= -\frac{\partial}{\partial t}\left(\overline{\rho_\theta {}^* M^*}^\lambda\right) + \frac{\partial}{\partial \theta}\left(\overline{p^* \frac{\partial z^*}{\partial \lambda}}^\lambda - \overline{\rho_\theta M \dot{\theta}}^\lambda + \overline{X}^\lambda\right). \end{aligned} \tag{2.16}$$

We wish to obtain an advective form of the angular momentum equation, so we multiply $\overline{M}^\lambda$ by the zonally averaged continuity equation in isentropic coordinates (Equation 2.4). We then subtract this product from Equation 2.16 and simplify. The result is

$$\begin{aligned}
&\overline{\rho_\theta}^\lambda \frac{\partial \overline{M}^\lambda}{\partial t} + \frac{1}{a\cos\varphi}\left\{\frac{\partial}{\partial\varphi}\left(\overline{\rho_\theta v M}^\lambda \cos\varphi\right)\right\} - \frac{\overline{M}^\lambda}{a\cos\varphi}\frac{\partial}{\partial\varphi}\left(\overline{\rho_\theta v}^\lambda \cos\varphi\right) \\
&= -\frac{\partial}{\partial t}\left(\overline{\rho_\theta{}^* M^*}^\lambda\right) + \overline{M}^\lambda \frac{\partial}{\partial\theta}\left(\overline{\rho_\theta \dot{\theta}}^\lambda\right) + \frac{\partial}{\partial\theta}\left(\overline{p^* \frac{\partial z^*}{\partial\lambda}}^\lambda - \overline{\rho_\theta M\dot{\theta}}^\lambda + \overline{X}^\lambda\right).
\end{aligned} \tag{2.17}$$

The mass-weighted average of any scalar variable, A, is defined in the following way:

$$\hat{A} \equiv \frac{\overline{\rho_\theta A}^\lambda}{\overline{\rho_\theta}^\lambda}. \tag{2.18}$$

The definition 2.18 implies:

$$\begin{aligned}
\rho_\theta A &= \overline{\rho_\theta A}^\lambda + \left(\rho_\theta A\right)^* \\
&= \overline{\rho_\theta}^\lambda \hat{A} + \left(\rho_\theta A\right)^*.
\end{aligned} \tag{2.19}$$

Applying 2.18 and 2.19 to scalar A and another scalar B, we can say:

$$\begin{aligned}
\overline{\rho_\theta AB}^\lambda &= \overline{\rho_\theta A}^\lambda \overline{B}^\lambda + \overline{\left(\rho_\theta A\right)^* B^*}^\lambda \\
&= \overline{\rho_\theta}^\lambda \hat{A}\overline{B}^\lambda + \overline{\left(\rho_\theta A\right)^* B^*}^\lambda.
\end{aligned} \tag{2.20}$$

Applying these identities 2.19 and 2.20 to $\hat{v}$, $\hat{\dot{\theta}}$, and M, we can say the following:

$$\begin{aligned}
\overline{\rho_\theta v M}^\lambda &= \overline{\rho_\theta v}^\lambda \overline{M}^\lambda + \overline{\left(\rho_\theta v\right)^* M^*}^\lambda \\
&= \overline{\rho_\theta}^\lambda \hat{v}\overline{M}^\lambda + \overline{\left(\rho_\theta v\right)^* M^*}^\lambda.
\end{aligned} \tag{2.21}$$

and

$$\begin{aligned}
\overline{\rho_\theta \dot{\theta} M}^\lambda &= \overline{\rho_\theta \dot{\theta}}^\lambda \overline{M}^\lambda + \overline{\left(\rho_\theta \dot{\theta}\right)^* M^*}^\lambda \\
&= \overline{\rho_\theta}^\lambda \hat{\dot{\theta}}\overline{M}^\lambda + \overline{\left(\rho_\theta \dot{\theta}\right)^* M^*}^\lambda.
\end{aligned} \tag{2.22}$$

Using 2.18 in the continuity equation, we can rewrite Equation 2.4 as:

$$\frac{\partial \overline{\rho_\theta}^{\lambda}}{\partial t} + \frac{1}{a\cos\varphi}\frac{\partial}{\partial \varphi}\left(\overline{\rho_\theta}^{\lambda}\hat{v}\cos\varphi\right) = -\frac{\partial}{\partial \theta}\left(\overline{\rho_\theta}^{\lambda}\hat{\dot{\theta}}\right). \tag{2.23}$$

Substituting 2.19 and 2.20 in the conservation of angular momentum equation (Equation 2.17), we simplify and obtain:

$$\begin{aligned}\overline{\rho_\theta}^{\lambda}\frac{\partial \overline{M}^{\lambda}}{\partial t} + \frac{1}{a\cos\varphi}\frac{\partial}{\partial \varphi}\left\{\left[\overline{\rho_\theta}^{\lambda}\hat{v}\overline{M}^{\lambda} + \overline{\left(\rho_\theta v\right)^{*}M^{*}}^{\lambda}\right]\cos\varphi\right\} - \frac{\overline{M}^{\lambda}}{a\cos\varphi}\frac{\partial}{\partial \varphi}\left(\overline{\rho_\theta}^{\lambda}\hat{v}\cos\varphi\right) \\ = -\frac{\partial}{\partial t}\left(\overline{\rho_\theta{}^{*}M^{*}}^{\lambda}\right) + \overline{M}^{\lambda}\frac{\partial}{\partial \theta}\left(\overline{\rho_\theta}^{\lambda}\hat{\dot{\theta}}\right) + \frac{\partial}{\partial \theta}\left[\overline{p^{*}\frac{\partial z^{*}}{\partial \lambda}}^{\lambda} - \overline{\rho_\theta}^{\lambda}\hat{\dot{\theta}}\overline{M}^{\lambda} - \overline{\left(\rho_\theta\dot{\theta}\right)^{*}M^{*}}^{\lambda} - \overline{X}^{\lambda}\right].\end{aligned} \tag{2.24}$$

We can simplify and gather eddy terms to the right-hand side to obtain:

$$\begin{aligned}\overline{\rho_\theta}^{\lambda}\left(\frac{\partial \overline{M}^{\lambda}}{\partial t} + \frac{\hat{v}}{a}\frac{\partial \overline{M}^{\lambda}}{\partial \varphi} + \hat{\dot{\theta}}\frac{\partial \overline{M}^{\lambda}}{\partial \theta}\right) = -\frac{\partial}{\partial t}\left(\overline{\rho_\theta{}^{*}M^{*}}^{\lambda}\right) \\ -\frac{1}{a\cos\varphi}\frac{\partial}{\partial \varphi}\left[\overline{\left(\rho_\theta v\right)^{*}M^{*}}^{\lambda}\cos\varphi\right] + \frac{\partial}{\partial \theta}\left[\overline{p^{*}\frac{\partial z^{*}}{\partial \lambda}}^{\lambda} - \overline{\left(\rho_\theta\dot{\theta}\right)^{*}M^{*}}^{\lambda} - \overline{X}^{\lambda}\right].\end{aligned} \tag{2.25}$$

In order to simplify Equation 2.25, we define the isentropic Eliassen-Palm flux and its divergence in the following way:

$$\mathbf{IEPF} \equiv \left(0,\ IEPF_{\varphi},\ IEPF_{\theta}\right) \tag{2.26}$$

$$IEPF_{\varphi} \equiv -\overline{\left(\rho_\theta v\right)^{*}M^{*}}^{\lambda} \tag{2.27}$$

$$IEPF_{\theta} \equiv \overline{p^{*}\frac{\partial z^{*}}{\partial \lambda}}^{\lambda} - \overline{\left(\rho_\theta\dot{\theta}\right)^{*}M^{*}}^{\lambda} \tag{2.28}$$

$$\nabla\cdot\mathbf{IEPF} = \frac{-1}{a\cos\varphi}\frac{\partial}{\partial \varphi}\left[\overline{\left(\rho_\theta v\right)^{*}M^{*}}^{\lambda}\cos\varphi\right] + \frac{\partial}{\partial \theta}\left[\overline{p^{*}\frac{\partial z^{*}}{\partial \lambda}}^{\lambda} - \overline{\left(\rho_\theta\dot{\theta}\right)^{*}M^{*}}^{\lambda}\right] \tag{2.29}$$

We apply this definition to Equation 2.25 to give:

$$\frac{\partial \overline{M}^{\lambda}}{\partial t} + \frac{\hat{v}}{a}\frac{\partial \overline{M}^{\lambda}}{\partial \varphi} + \hat{\dot{\theta}}\frac{\partial \overline{M}^{\lambda}}{\partial \theta} = \frac{1}{\overline{\rho_\theta}^{\lambda}}\left[-\frac{\partial}{\partial t}\left(\overline{\rho_\theta {}^* M^*}^{\lambda}\right) + \nabla \cdot \mathbf{IEPF} - \frac{\partial \overline{X}^{\lambda}}{\partial \theta} \right]. \tag{2.30}$$

Chapter 3

Methods

Given the information and background of the previous chapters, we now walk through the tools and methods utilized to characterize the angular momentum budget of the QBO on isentropic surfaces. We discuss our use of ERA-Interim reanalysis, and its previous utility in the characterization of the QBO momentum budget. There is a description of the correction to the meridional wind in order to balance the mass budget. We describe the calculations using equations from the previous chapter describing the angular momentum and mass budgets. We discuss the isolation of various components to determine contributions of various angular momentum budget components to the driving and maintenance of the QBO.

3.1 Data

The data used is ECMWF Reanalysis Interim (ERA-I) on potential temperature surfaces from 1979-2017 [Dee et al., 2011]. The dataset has a temporal resolution of 6 hours, 1.42 degrees of horizontal resolution and 15 isentropic levels, peaking at 850 K or approximately 5-10 hPa. ERA-Interim has been used in previous studies assessing the QBO on pressure and model levels, and was found to be reliable in the middle and lower stratosphere [Pahlavan et al., 2021; Ern et al., 2014; Kim and Chun, 2015b; Schenzinger et al., 2017] with a good representation of planetary waves [Ern and Preusse, 2009b,a]. Kim and Chun [2015b] did find a loss of accuracy when ERA-Interim was interpolated from native model levels to pressure levels that produced weakened Kelvin wave forcing. It is possible that the same is true for interpolation to potential temperature surfaces. It should also be noted that ERA-Interim lacks a gravity wave drag parameterization, so wave driving due to small-scale gravity waves is interpreted from the residual correction to the wind from data assimilation.

3.2 Mass budget correction

Consider the zonally averaged mass continuity equation in isentropic coordinates (Equation 2.4), repeated here for convenience:

$$\frac{\partial}{\partial t}\overline{\rho_\theta}^{\lambda} + \frac{1}{a\cos\phi}\frac{\partial}{\partial\phi}\left(\overline{\rho_\theta v}^{\lambda}\cos\phi\right) + \frac{\partial}{\partial\theta}\left(\overline{\rho_\theta \dot{\theta}}^{\lambda}\right) = 0 \tag{3.1}$$

Vertically integrating 3.1, we have:

$$\frac{\partial}{\partial t}\left(\int_0^\infty \overline{\rho_\theta}^{\lambda} d\theta\right) + \frac{1}{a\cos\phi}\frac{\partial}{\partial\phi}\left(\int_0^\infty \overline{\rho_\theta v}^{\lambda} d\theta\cos\phi\right) + \frac{\partial}{\partial\theta}\left(\int_0^\infty \overline{\rho_\theta \dot{\theta}}^{\lambda} d\theta\right) = 0 \tag{3.2}$$

The first term of 3.2 is equal to $\frac{1}{g}\frac{\partial p_s}{\partial t}$. The last term of 3.2 is zero because the vertical mass flux is zero both at the surface and at the top of atmosphere. This leaves us with:

$$\frac{1}{g}\frac{\partial p_s}{\partial t} + \frac{1}{a\cos\phi}\frac{\partial}{\partial\phi}\left(\int_0^\infty \overline{\rho_\theta v}^{\lambda} d\theta\cos\phi\right) = 0 \tag{3.3}$$

Instantaneously, the first term of 3.3 is very small, and in a long time average, it disappears. Thus:

$$\overline{\int_0^\infty \overline{\rho_\theta v}^{\lambda} d\theta}^{t} = 0 \tag{3.4}$$

This is not true when tested in a long time average of data from ERA-Interim isentropic analysis, so we apply a correction to meridional wind in order to balance the mass budget in our dataset and enforce 3.4 in a long time average. For simplicity, the corrected wind will be defined by v' and the original meridional wind will be v. We want to enforce the following, where $nlev$ is the total number of vertical levels:

$$\sum_{j=0}^{nlev-2} \overline{\rho_\theta v'_j}^{\lambda,t} \Delta\theta_j = 0 \tag{3.5}$$

Thus, we define a function $c(\phi, t)$ that is uniform in height, but varies with latitude and time, so that:

$$v'(\varphi,\theta,t) = v(\varphi,\theta,t) - c(\varphi,t) \tag{3.6}$$

Substitute 3.6 into 3.5 and use it to solve for $c(\phi, t)$.

$$\sum_{j=0}^{nlev-2} \overline{\rho_\theta \big(v - c(\varphi,t)\big)}_j^{\lambda,t} \Delta\theta_j = 0 \tag{3.7}$$

$$\sum_{j=0}^{nlev-2} \overline{\rho_\theta v}_j^{\lambda,t} \Delta\theta_j - \sum_{j=0}^{nlev-2} \overline{\rho_\theta c(\phi,t)}_j^{\lambda,t} \Delta\theta_j = 0 \tag{3.8}$$

$$c(\varphi,t) \sum_{j=0}^{nlev-2} \overline{\rho_\theta}_j^{\lambda,t} \Delta\theta_j = \sum_{j=0}^{nlev-2} \overline{\rho_\theta v}_j^{\lambda,t} \Delta\theta_j \tag{3.9}$$

$$c(\varphi,t) = \frac{\sum_{j=0}^{nlev-2} \overline{\rho_\theta v}_j^{\lambda,t} \Delta\theta_j}{\sum_{j=0}^{nlev-2} \overline{\rho_\theta}_j^{\lambda,t} \Delta\theta_j} \tag{3.10}$$

This correction is applied to the meridional wind at all time steps, vertical levels, latitudes, and longitudes. Figure 3.1 shows the correction as a function of latitude as an average during June, July, and August (JJA), as well as December, January, and February (DJF).

3.3 Diagnosis of the vertical flux of mass

Figure 3.2 is a schematic walking through the steps described in this section.

We begin with the mass continuity equation in isentropic and spherical coordinates, given in Equation 2.3, and repeated here for convenience:

$$\frac{\partial \rho_\theta}{\partial t} + \frac{1}{a\cos\varphi}\frac{\partial}{\partial \varphi}\big(\rho_\theta v \cos\varphi\big) + \frac{1}{a\cos\varphi}\frac{\partial}{\partial \lambda}\big(\rho_\theta u\big) + \frac{\partial}{\partial \theta}\big(\rho_\theta \dot{\theta}\big) = 0, \tag{3.11}$$

From the reanalysis, we begin with the variables for pressure and the horizontal wind components on potential temperature surfaces at all longitudes and latitudes at 6-hourly time resolution for January 1979-December 2017. Pseudodensity (ρ_θ) is computed first, according to

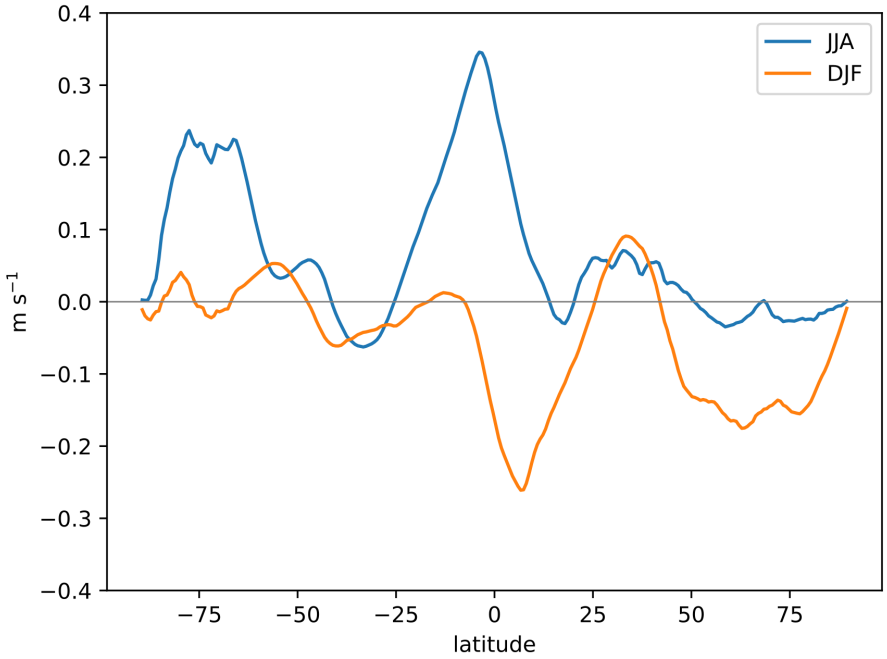

Figure 3.1: Correction to the meridional wind as a function of latitude as seasonal averages during June, July, and August (JJA), as well as December, January, and February (DJF).

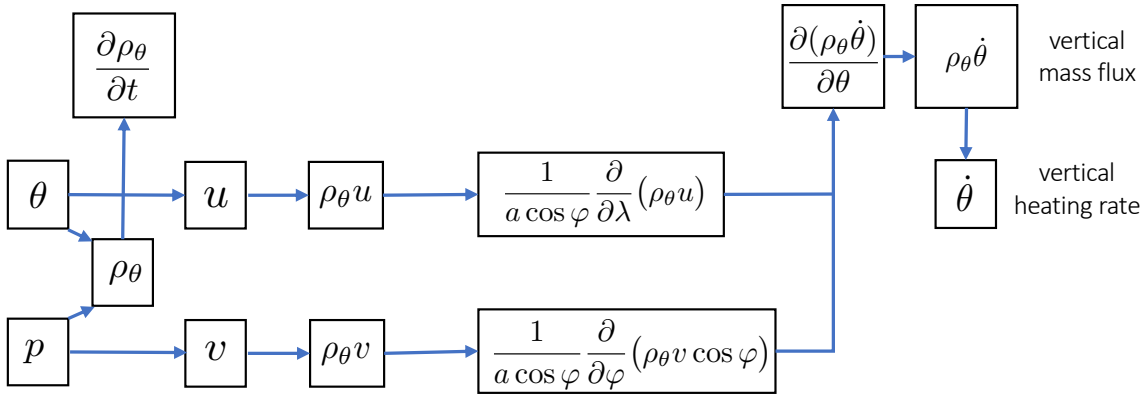

Figure 3.2: Schematic detailing the computation of vertical heating rate and the vertical mass flux from the mass continuity equation.

2.2. We directly calculate the pseudodensity tendency, as well as zonal and meridional mass flux divergences, leaving the vertical mass flux divergence as a residual:

$$\frac{\partial}{\partial\theta}(\rho_\theta\dot{\theta}) = -\frac{\partial\rho_\theta}{\partial t} - \frac{1}{a\cos\varphi}\frac{\partial}{\partial\varphi}(\rho_\theta v\cos\varphi) - \frac{1}{a\cos\varphi}\frac{\partial}{\partial\lambda}(\rho_\theta u). \tag{3.12}$$

Assuming zero mass flux at the top, we integrate the vertical mass flux divergence downwards to determine the vertical mass flux, $\rho_\theta\dot{\theta}$, at each isentropic level:

$$\rho_\theta\dot{\theta} = \int_\theta^{\theta_{top}} \left(-\frac{\partial\rho_\theta}{\partial t} - \frac{1}{a\cos\varphi}\frac{\partial}{\partial\varphi}(\rho_\theta v\cos\varphi) - \frac{1}{a\cos\varphi}\frac{\partial}{\partial\lambda}(\rho_\theta u)\right) d\theta \tag{3.13}$$

We divide out the pseudodensity from the vertical mass flux. This produces the time tendency of potential temperature–in other words, the heating rate. As was discussed in section 2.1, an advantage of isentropic coordinates is that the vertical flux of mass is proportional to the heating rate, $\dot{\theta}$.

$$\hat{\dot{\theta}} = \frac{\overline{\rho_\theta\dot{\theta}}^\lambda}{\overline{\rho_\theta}^\lambda} \tag{3.14}$$

3.4 Diagnosis of the vertical flux of angular momentum

Figure 3.3 is a schematic walking through the steps described in this section. A more detailed description of the discretizations used in this section and the previous section are laid out in the Appendix in Section B.

We begin with equation 2.30, repeated here for convenience:

$$\frac{\partial\overline{M}^\lambda}{\partial t} + \frac{\hat{v}}{a}\frac{\partial\overline{M}^\lambda}{\partial\varphi} + \hat{\dot{\theta}}\frac{\partial\overline{M}^\lambda}{\partial\theta} = \frac{1}{\overline{\rho_\theta}^\lambda}\left[-\frac{\partial}{\partial t}\left(\overline{\rho_\theta{}^* M^*}^\lambda\right) + \nabla\cdot\mathbf{IEPF} - \frac{\partial\overline{X}^\lambda}{\partial\theta}\right], \tag{3.15}$$

where (also repeated)

$$\nabla\cdot\mathbf{IEPF} = \frac{-1}{a\cos\varphi}\frac{\partial}{\partial\varphi}\left[\overline{(\rho_\theta v)^* M^*}^\lambda\cos\varphi\right] + \frac{\partial}{\partial\theta}\left[\overline{p^*\frac{\partial z^*}{\partial\lambda}}^\lambda - \overline{(\rho_\theta\dot{\theta})^* M^*}^\lambda\right]. \tag{3.16}$$

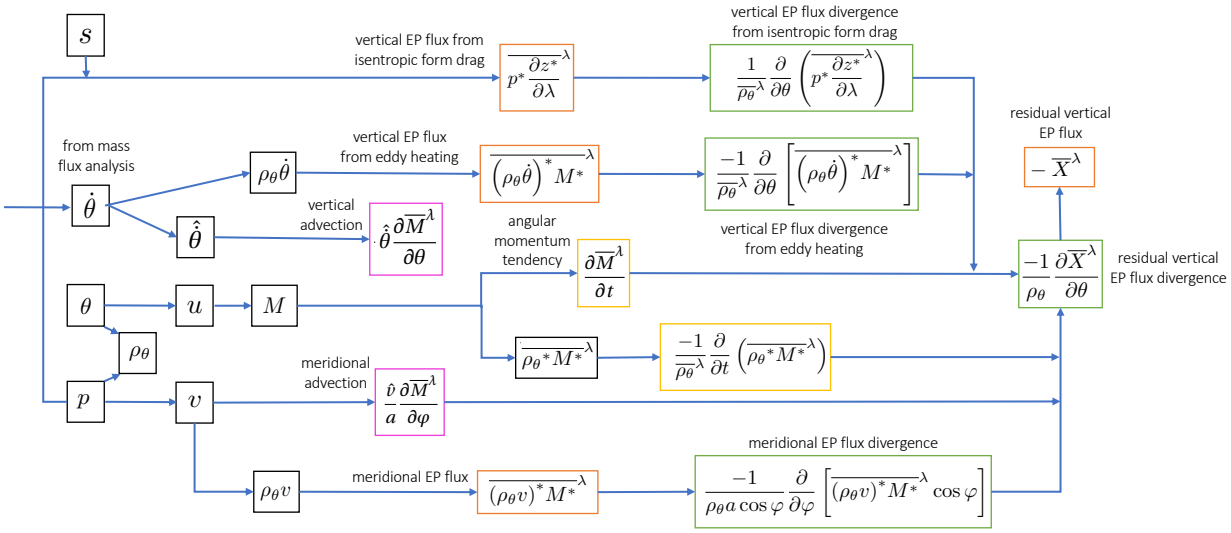

Figure 3.3: Schematic detailing the computation of Eliassen-Palm flux divergences, advection terms and the unresolved wave contribution to vertical EP flux.

We want to compute based on monthly averages, so we rewrite 3.15 and 3.16 with a temporal average included in the notation:

$$\frac{\partial \overline{M}^{\lambda}}{\partial t} + \frac{\hat{v}}{a}\frac{\partial \overline{M}^{\lambda,t}}{\partial \varphi} + \hat{\dot{\theta}}\frac{\partial \overline{M}^{\lambda,t}}{\partial \theta} = \frac{1}{\overline{\rho_\theta}^{\lambda,t}}\left[-\frac{\partial}{\partial t}\left(\overline{\rho_\theta {}^* M^*}^{\lambda,t}\right) + \nabla\cdot\mathbf{IEPF} - \frac{\partial \overline{X}^{\lambda,t}}{\partial \theta}\right] \tag{3.17}$$

and

$$\nabla\cdot\mathbf{IEPF} = \frac{-1}{a\cos\varphi}\frac{\partial}{\partial \varphi}\left[\overline{(\rho_\theta v)^* M^*}^{\lambda,t}\cos\varphi\right] + \frac{\partial}{\partial \theta}\left[\overline{p\frac{\partial z}{\partial \lambda}}^{\lambda,t} - \overline{(\rho_\theta \dot{\theta})^* M^*}^{\lambda,t}\right]. \tag{3.18}$$

We calculate absolute angular momentum, M, zonally average, and compute its tendency. We compute the mass-weighted zonal average meridional wind, $\hat{v}$, and $\hat{\dot{\theta}}$ according to 3.14, in order to compute the meridional and vertical advection terms. The first term on the right hand side of 3.15, the meridional EP flux divergence, and the vertical EP flux divergence are computed using eddy values of ρ_θ^*, $(\rho_\theta v)^*$, $(\rho_\theta \dot{\theta})^*$ and M^*.

Using the Montgomery potential (dry static energy), s, from ERA-Interim, we compute z, according to its definition:

$$s \equiv \Pi\theta + gz, \tag{3.19}$$

where Π is the Exner function, which is defined as:

$$\Pi = c_p \left(\frac{p}{p_0} \right)^{\kappa}. \tag{3.20}$$

We can then compute the vertical EP flux divergence due to isentropic form drag. We are then able to isolate the residual term:

$$\frac{1}{\overline{\rho_\theta}^{\lambda}} \left(\frac{-\partial \overline{X}^{\lambda}}{\partial \theta} \right) = \frac{\partial \overline{M}^{\lambda}}{\partial t} + \frac{\hat{v}}{a} \frac{\partial \overline{M}^{\lambda}}{\partial \varphi} + \hat{\dot{\theta}} \frac{\partial \overline{M}^{\lambda}}{\partial \theta} + \frac{1}{\overline{\rho_\theta}^{\lambda}} \left(\frac{\partial}{\partial t} \left(\overline{\rho_\theta {}^* M^*}^{\lambda} \right) \right) - \frac{1}{\overline{\rho_\theta}^{\lambda}} \left(\nabla \cdot \mathbf{IEPF} \right) \tag{3.21}$$

We can multiply both sides by ρ_θ, giving:

$$\frac{-\partial \overline{X}^{\lambda}}{\partial \theta} = \overline{\rho_\theta}^{\lambda} \left(\frac{\partial \overline{M}^{\lambda}}{\partial t} + \frac{\hat{v}}{a} \frac{\partial \overline{M}^{\lambda}}{\partial \varphi} + \hat{\dot{\theta}} \frac{\partial \overline{M}^{\lambda}}{\partial \theta} \right) + \frac{\partial}{\partial t} \left(\overline{\rho_\theta {}^* M^*}^{\lambda} \right) - \nabla \cdot \mathbf{IEPF} \tag{3.22}$$

We assume zero angular momentum flux at the top isentropic level, and integrate 3.22 to get vertical angular momentum flux due to unresolved wave forcing and corrections from data assimilation:

$$-\overline{X}^{\lambda} = \int_{\theta}^{\theta_{top}} \left(\overline{\rho_\theta}^{\lambda} \left(\frac{\partial \overline{M}^{\lambda}}{\partial t} + \frac{\hat{v}}{a} \frac{\partial \overline{M}^{\lambda}}{\partial \varphi} + \hat{\dot{\theta}} \frac{\partial \overline{M}^{\lambda}}{\partial \theta} \right) + \frac{\partial}{\partial t} \left(\overline{\rho_\theta {}^* M^*}^{\lambda} \right) - \nabla \cdot \mathbf{IEPF} \right) d\theta \tag{3.23}$$

3.5 Determination of zonal flow contribution

Since we are mostly interested in the change to the zonal wind, we divide each component of Equation 2.30 by $a\cos\varphi$ to determine contribution to the zonal wind tendency (Figure 4.18), producing:

$$\left(a\cos\varphi\right)^{-1}\frac{\partial\overline{M}^{\lambda}}{\partial t}+\left(a\cos\varphi\right)^{-1}\frac{\hat{v}}{a}\frac{\partial\overline{M}^{\lambda}}{\partial\varphi}+\left(a\cos\varphi\right)^{-1}\hat{\dot{\theta}}\frac{\partial\overline{M}^{\lambda}}{\partial\theta}=$$
$$\left(a\cos\varphi\right)^{-1}\frac{1}{\overline{\rho_\theta}^{\lambda}}\left[-\frac{\partial}{\partial t}\left(\overline{\rho_\theta{}^{*}M^{*}}^{\lambda}\right)+\nabla\cdot\mathbf{IEPF}-\frac{\partial\overline{X}^{\lambda}}{\partial\theta}\right], \quad (3.24)$$

which simplifies to:

$$\frac{\partial\overline{u}^{\lambda}}{\partial t}=\frac{-\hat{v}}{a^2\cos\varphi}\frac{\partial\overline{M}^{\lambda}}{\partial\varphi}+\frac{-\hat{\dot{\theta}}}{a\cos\varphi}\frac{\partial\overline{M}^{\lambda}}{\partial\theta}+\frac{-1}{\overline{\rho_\theta}^{\lambda}a\cos\varphi}\frac{\partial}{\partial t}\left(\overline{\rho_\theta{}^{*}M^{*}}^{\lambda}\right)+$$
$$\frac{-1}{\overline{\rho_\theta}^{\lambda}a^2\cos^2\varphi}\frac{\partial}{\partial\varphi}\left(\overline{\left(\rho_\theta v\right)^{*}M^{*}}^{\lambda}\cos\varphi\right)+\frac{1}{\overline{\rho_\theta}^{\lambda}a\cos\varphi}\frac{\partial}{\partial\theta}\left(\overline{p\frac{\partial z}{\partial\lambda}}^{\lambda}\right)+$$
$$\frac{-1}{\overline{\rho_\theta}^{\lambda}a\cos\varphi}\frac{\partial}{\partial\theta}\left(\overline{\left(\rho_\theta\dot{\theta}\right)^{*}M^{*}}^{\lambda}\right)+\frac{-1}{\overline{\rho_\theta}^{\lambda}a\cos\varphi}\frac{\partial\overline{X}^{\lambda}}{\partial\theta}. \quad (3.25)$$

Later on, it will become advantageous to consider a residual term that subtracts out the contributions to $\left(\partial\overline{u}^{\lambda}\right)\left(\partial t\right)^{-1}$ from vertical and meridional advection. Thus, we are able to consider the components of the residual term that are not spent correcting and damping an overestimated vertical advection. Beginning with Equation 3.25 and defining a residual term $G(t,\theta,\varphi)$:

$$\frac{\partial\overline{u}^{\lambda}}{\partial t}=\frac{-1}{\overline{\rho_\theta}^{\lambda}a\cos\varphi}\frac{\partial}{\partial t}\left(\overline{\rho_\theta{}^{*}M^{*}}^{\lambda}\right)+\frac{-1}{\overline{\rho_\theta}^{\lambda}a^2\cos^2\varphi}\frac{\partial}{\partial\varphi}\left(\overline{\left(\rho_\theta v\right)^{*}M^{*}}^{\lambda}\cos\varphi\right)+$$
$$\frac{1}{\overline{\rho_\theta}^{\lambda}a\cos\varphi}\frac{\partial}{\partial\theta}\left(\overline{p\frac{\partial z}{\partial\lambda}}^{\lambda}\right)+\frac{-1}{\overline{\rho_\theta}^{\lambda}a\cos\varphi}\frac{\partial}{\partial\theta}\left(\overline{\left(\rho_\theta\dot{\theta}\right)^{*}M^{*}}^{\lambda}\right)+G(t,\theta,\varphi), \quad (3.26)$$

where

$$G(t,\theta,\varphi)=\frac{-1}{\overline{\rho_\theta}^{\lambda}a\cos\varphi}\frac{\partial\overline{X}^{\lambda}}{\partial\theta}+\frac{-\hat{v}}{a^2\cos\varphi}\frac{\partial\overline{M}^{\lambda}}{\partial\varphi}+\frac{-\hat{\dot{\theta}}}{a\cos\varphi}\frac{\partial\overline{M}^{\lambda}}{\partial\theta}. \quad (3.27)$$

Chapter 4

Results

4.1 Zonal wind

In this subsection, we show plots of the zonal wind and its acceleration in the tropical stratosphere to establish the QBO pattern that we seek in other variables. In Chapter 1, we saw time series of zonal wind in the stratosphere in Figure 1.1, as well as the latitudinal distribution of zonal wind in the stratosphere as a function of time in Figure 1.2.

Figure 4.1 shows latitude-height plots of the zonally averaged zonal wind for two different seasons–Northern Hemisphere (NH) winter (DJF) and Southern Hemisphere (SH) winter (JJA). We can see both the Northern and Southern Hemispheric westerly winter stratospheric polar vortices; the SH polar vortex is much stronger because the lack of topography produces fewer planetary waves that can disrupt it. We can see the subtropical jet stream in both hemispheres during both seasons, with a stronger jet in the winter hemisphere. There is a weak signal in the tropical stratosphere tending towards easterlies in the summer hemisphere, as is consistent with the climatology of the stratospheric circulation. This tendency is what allows the easterly phase of the QBO to reach a stronger maximum wind speed, which can be seen in Figure 1.1.

Figure 4.2 is a QBO composite of the deseasonalized zonal wind as a function of height. The QBO composite in Figure 4.2, as well as others shown later on, are constructed based on when the zonally averaged zonal wind speed at 20 hPa is zero m s^{-1}, transitioning from a positive to a negative value [Schenzinger et al., 2017]. Since the data exists on isentropic levels, zonal wind values are linearly interpolated to a 20 hPa pressure level. This transition time is designated as month 0 on the horizontal axis. The 14 months leading up to that time represent the westerly phase of the QBO, and the 14 months after that time represent the easterly phase. Composites are averaged over 17 QBO-East to West phase transitions between 1979-2018. Ozone in the stratosphere absorbs incoming solar radiation creating a more rapid increase of potential tem-

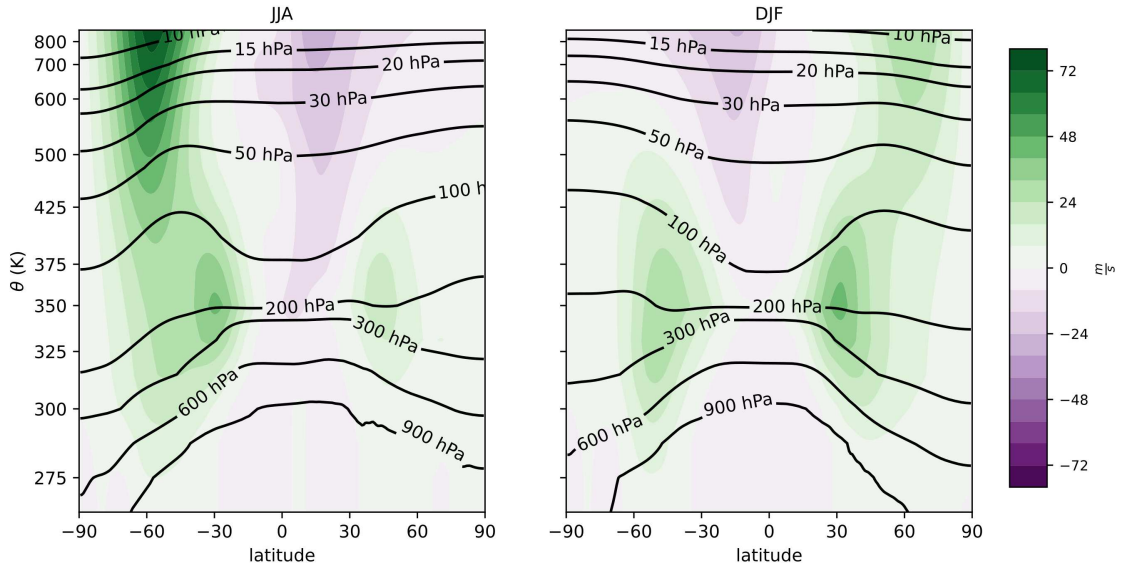

Figure 4.1: Latitude-height plots of zonally averaged **zonal wind** averaged for JJA (June, July, August) and DJF (December, January, February) on isentropic surfaces, averaged for 1979-2018. Pressure contours have been included for orientation.

perature with height in the stratosphere than in the troposphere; the tick spacing on the vertical axis for potential temperature is skewed accordingly.

Figure 4.3 more clearly shows the structural evolution of the deseasonalized zonal wind in the stratosphere. As discussed earlier in this section, when comparing with Figure 1.1, deseasonalization evens out the maxima of the easterly and westerly phases, each maximizing at 24 m s^{-1}.

Figure 4.4 is a QBO composite of zonal wind acceleration with an extended x-axis. The "zero" tick on the x-axis still represents the same point at which the transition from positive to negative winds occurs, as in the QBO composites of Figures 4.2 and 4.3, but with a 28 month extension to more clearly show the evolution between cycles. Figure 4.4 shows maximum negative acceleration at easterly phase transition times and maximum positive acceleration at westerly phase transition times. A notable aspect of the composited acceleration is the six-month pulses throughout the stratosphere; a similar pulsing trend occurs in later figures throughout

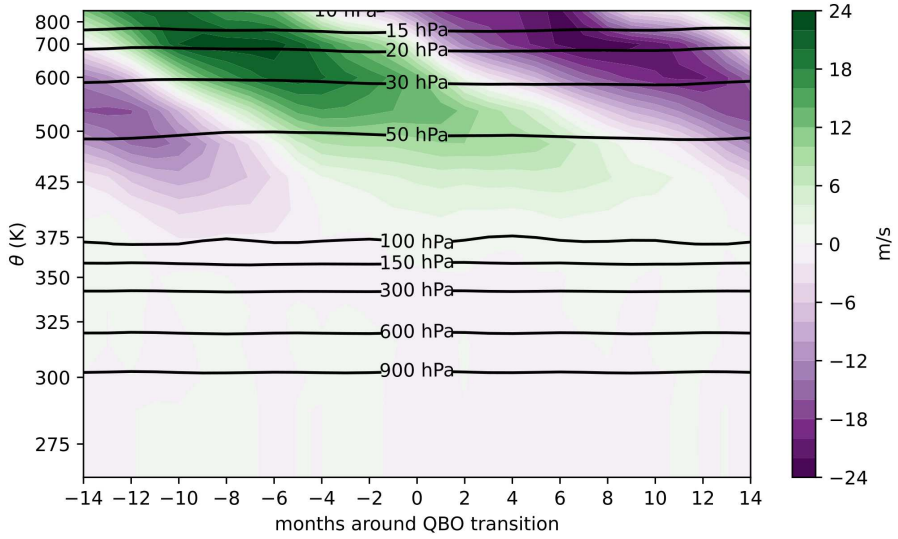

Figure 4.2: QBO composite of de-seasonalized zonally and monthly averaged **zonal wind** on isentropic surfaces. Results have been meridionally averaged from 5° N - 5° S. Pressure contours have been included for orientation. QBO cycles averaged from 1979-2018.

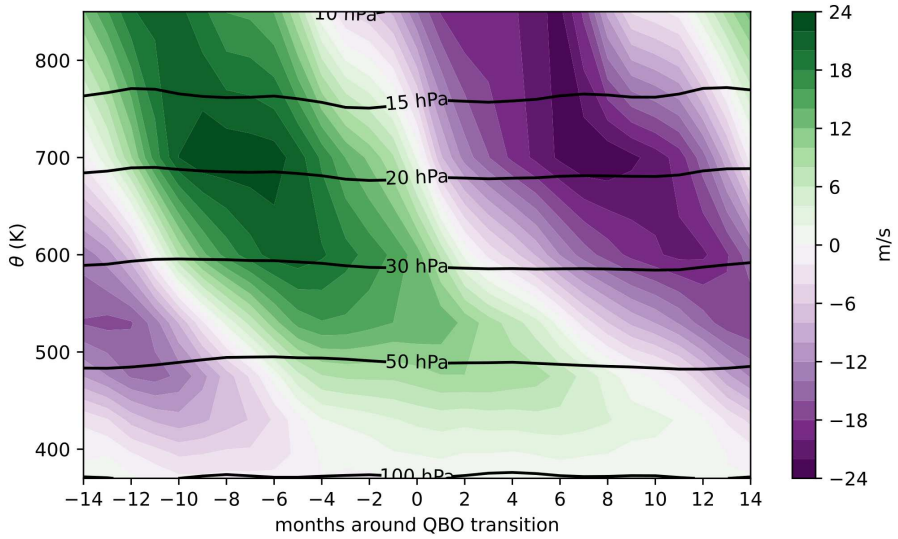

Figure 4.3: QBO composite of de-seasonalized zonally and monthly averaged **zonal wind** on isentropic surfaces in the stratosphere. Results have been meridionally averaged from 5° N - 5° S. Pressure contours have been included for orientation. QBO cycles averaged from 1979-2018.

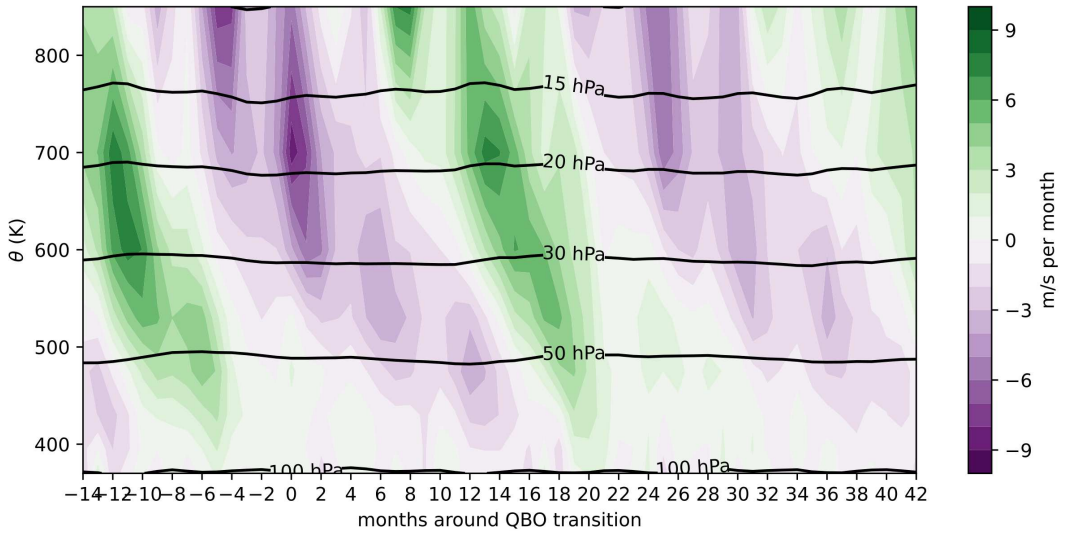

Figure 4.4: QBO composite of de-seasonalized zonally and monthly averaged **time tendency of zonal wind**, $\left(\partial\overline{u}^{\lambda}\right)(\partial t)^{-1}$, on isentropic surfaces. Results have been meridionally averaged from $5°N$ - $5°S$. Pressure contours have been included for orientation. The "zero" tick on the x-axis still represents the same point at which the transition from positive to negative winds occurs, as in the QBO composites of Figures 4.2 and 4.3, but with a 28 month extension to more clearly show the evolution between cycles.

the rest of this thesis. It is a signature of the SAO and its interactions with the QBO, as discussed in Chapter 1.

Figures 4.5 and 4.6 show the seasonaly meridional distributions of the mass-weighted average of the meridional wind, in the full atmospheric column and the stratosphere, respectively. We can see evidence of the Brewer-Dobson circulation in Figure 4.6.

4.2 Mass, angular momentum, and their circulations

4.2.1 Pseudodensity

Figure 4.7 is a latitude-height plot of annually and zonally averaged pseudodensity. There is no mass in the lowest isentropic layer from the equator to the midlatitudes because average potential temperatures do not reach down to 265 K (the lowest level in our dataset). So those portions of the plot represent the massless layers described in Chapter 2. On the other hand,

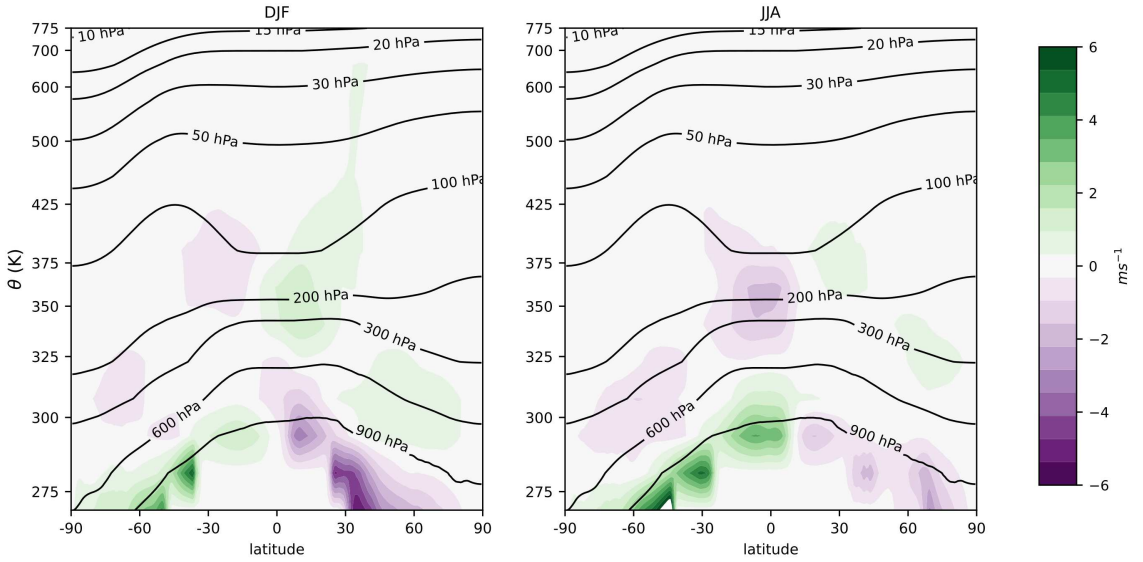

Figure 4.5: Latitude-height plots of mass-weighted zonal average of meridional wind, $\hat{v}$, averaged for JJA (June, July, August) and DJF (December, January, February) on isentropic surfaces, averaged for 1979-2018. Pressure contours have been included for orientation.

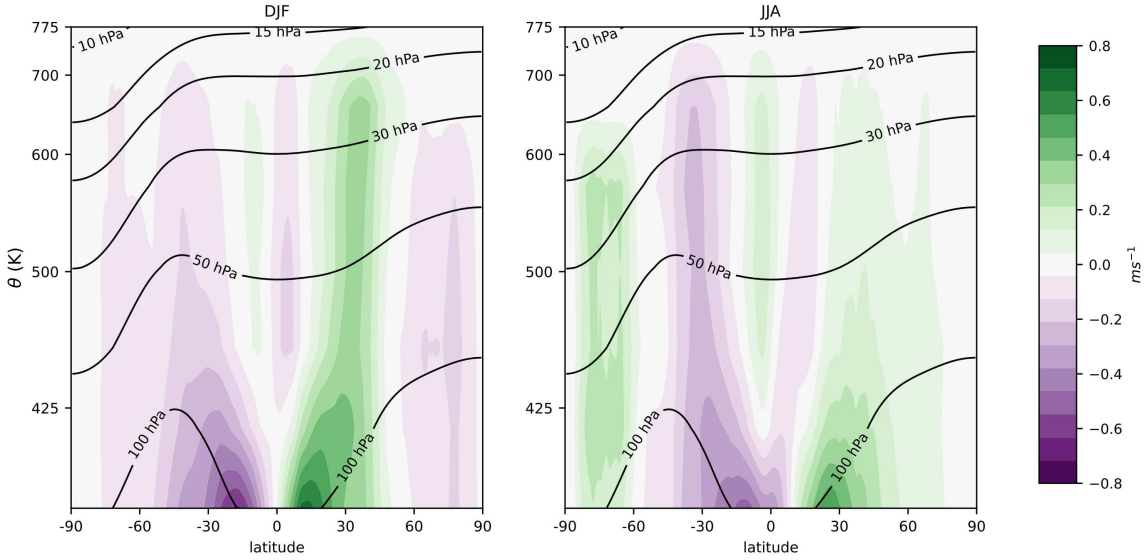

Figure 4.6: Latitude-height plots of mass-weighted zonal average of meridional wind, $\hat{v}$, averaged for JJA (June, July, August) and DJF (December, January, February) on isentropic surfaces *in the stratosphere*, averaged for 1979-2018. Pressure contours have been included for orientation.

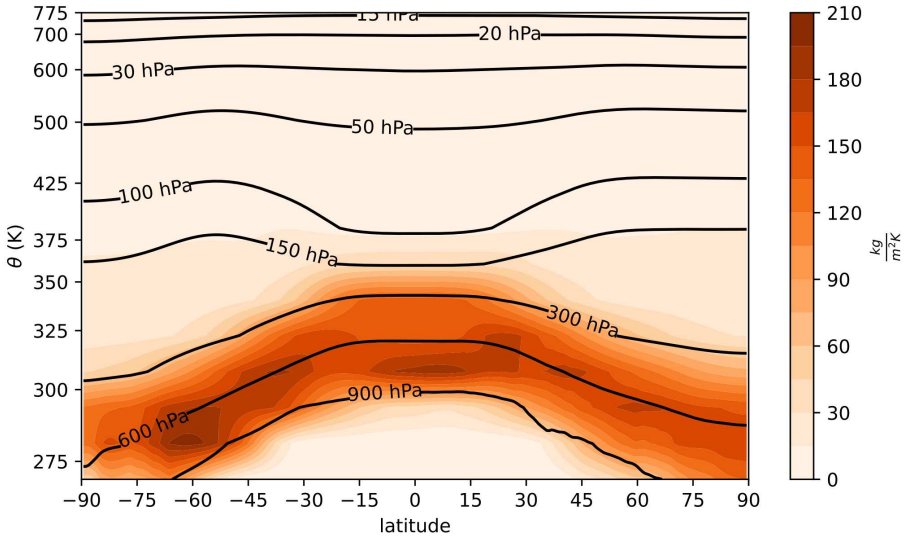

Figure 4.7: Latitude-height figure of zonally and annually averaged pseudodensity, ρ_θ, on isentropic surfaces from 1979-2018. Pressure contours have been included for orientation.

mass exists in the lowest layers over the polar regions in both hemispheres, where cold dense air exists.

Figure 4.8 shows a QBO composite of deseasonalized pseudodensity in the stratosphere. We see a pattern of downward propagating pseudodensity anomalies of changing sign in the stratosphere, mirroring the quasi-biennial oscillation in the zonal wind field, with positive anomalies during the westerly phase and negative during the easterly phase. The maximum of pseudodensity anomalies occurs about 20 hPa lower than the maximum wind speeds.

4.2.2 Mass circulation

Figure 4.9 shows the stream function for the mass circulation in isentropic coordinates, Ψ_θ, defined in the following way:

$$\overline{\rho_\theta v}^{\lambda,t} 2\pi a \cos\varphi \equiv \frac{\partial \Psi_\theta}{\partial \theta} \tag{4.1}$$

$$\overline{\rho_\theta \dot{\theta}}^{\lambda,t} 2\pi a^2 \cos\varphi \equiv \frac{\partial \Psi_\theta}{\partial \varphi} \tag{4.2}$$

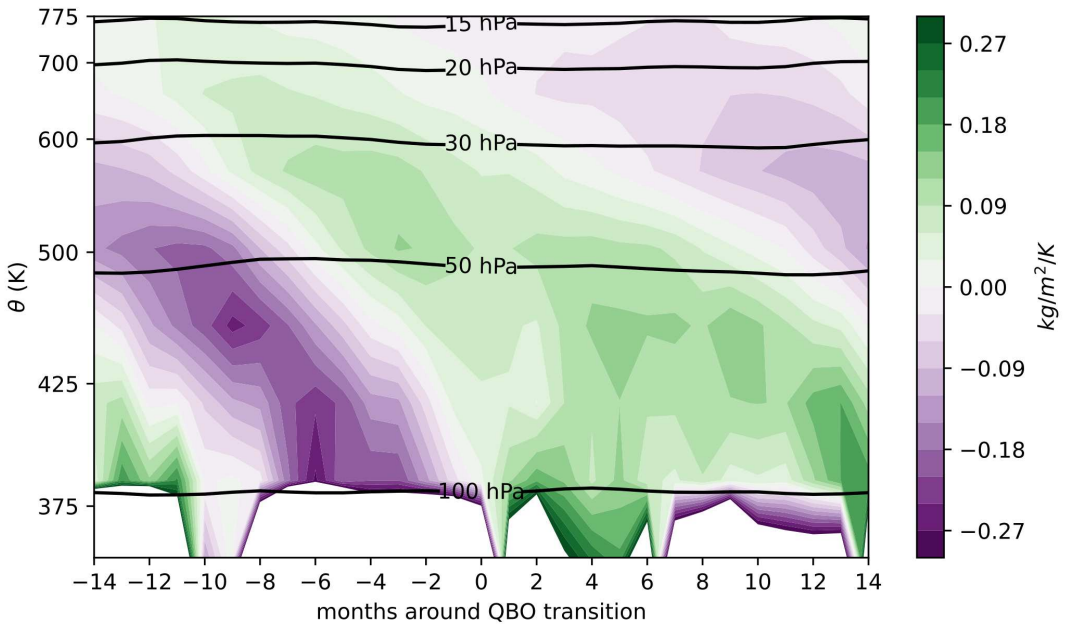

Figure 4.8: QBO composite of zonally and monthly averaged **pseudodensity**, ρ_θ, on isentropic surfaces in both the full column from surface to TOA and trimmed to just the stratosphere. Results have been meridionally averaged from 5° N - 5° S. Pressure contours have been included for orientation. QBO cycles averaged from 1979-2018.

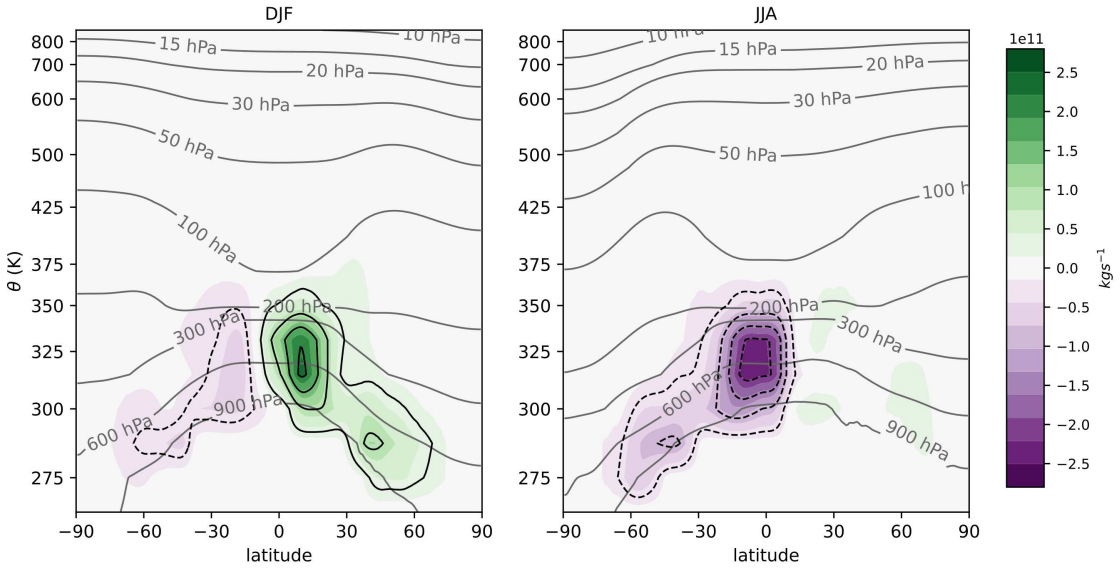

Figure 4.9: Streamfunction of mass circulation for DJF and JJA, Ψ_θ, on isentropic surfaces from 1979-2018. Units are kgs^{-1}. Pressure contours have been included for orientation.

We can see the Hadley cell in the tropics, mainly in the winter hemisphere. A unique aspect of the isentropic coordinates is that the Hadley cell reaches towards the pole. The mass circulation is much stronger in the troposphere than in the stratosphere, which is expected, since the stratosphere does not contain very much mass. The lack of mass means that it does not take very much momentum flux divergence to change the wind.

Since we are mostly interested in the stratosphere, we trim Figure 4.9 to the stratosphere with a refined color bar to resolve the stratospheric circulation more clearly. In Figure 4.10, we can see that the mass circulation continues in the stratosphere with a similar pattern as the troposphere, but slowly diminishing to zero with height. The Brewer-Dobson circulation in the upper stratosphere does not show up in this figure; although, it is visible in Figure 4.6.

4.2.3 Heating rate

Figure 4.11 shows the QBO composite of the mass-weighted zonal mean of the heating rate. No smoothing filter is applied, so there is still some noise in the QBO signal. Vertical velocity is poorly constrained in most reanalyses [Kim and Chun, 2015b], but $\dot{\theta}$ is smoother in the

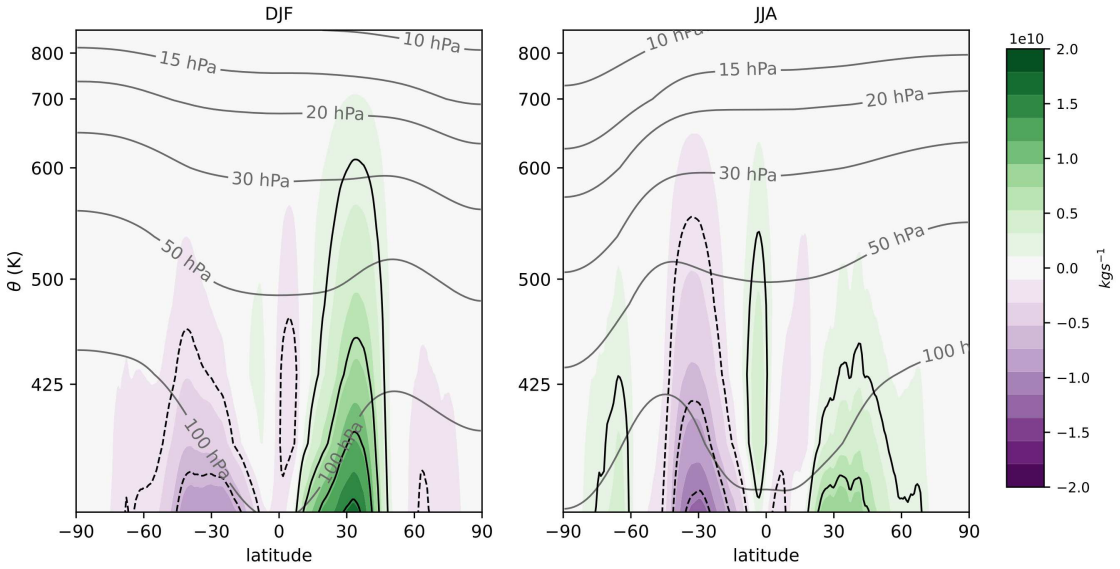

Figure 4.10: Streamfunction of mass circulation in the *stratosphere* for DJF and JJA, Ψ_θ, on isentropic surfaces from 1979-2018. Units are kgs^{-1}. Pressure contours have been included for orientation.

stratosphere than w or ω. When comparing with Figure 4.3, there is generally downward motion in regions with easterly zonal flow and upward motion in those with westerly zonal flow. Downward motion in isentropic coordinates corresponds to cooling and upward motion corresponds to warming. This aligns with the QBO signal in temperature, discussed in Chapter 1. The pulsing SAO signal seen in the zonal wind tendency in Figure 4.4 is present in the maxima of negative heating rates and to some degree in the maxima of positive heating rates with more noise. There is also an approximate two-month pulsing signal between -4 and +4 months; the reason for this is unclear, but it may be an artifact of the calculation.

4.2.4 Angular momentum circulation

Figure 4.12 shows the stream function for the *total* angular momentum flux in isentropic coordinates, Ψ_M, defined in the following way:

$$\overline{\rho_\theta v M}^{\lambda,t} 2\pi a \cos\varphi \equiv \frac{\partial \Psi_M}{\partial \theta} \tag{4.3}$$

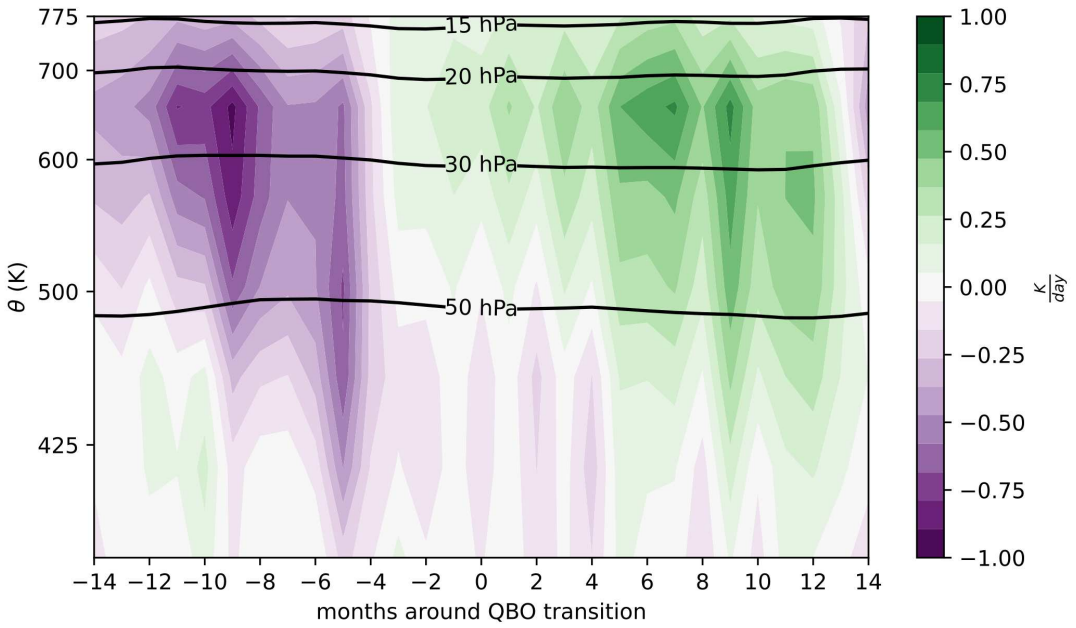

Figure 4.11: QBO composite of monthly averaged mass-weighted zonal average of the **heating rate**, $\hat{\dot{\theta}}$, on isentropic surfaces in both the full column from surface to TOA and trimmed to just the stratosphere. Results have been meridionally averaged from $5°N$ - $5°S$. Pressure contours have been included for orientation. QBO cycles averaged from 1979-2018.

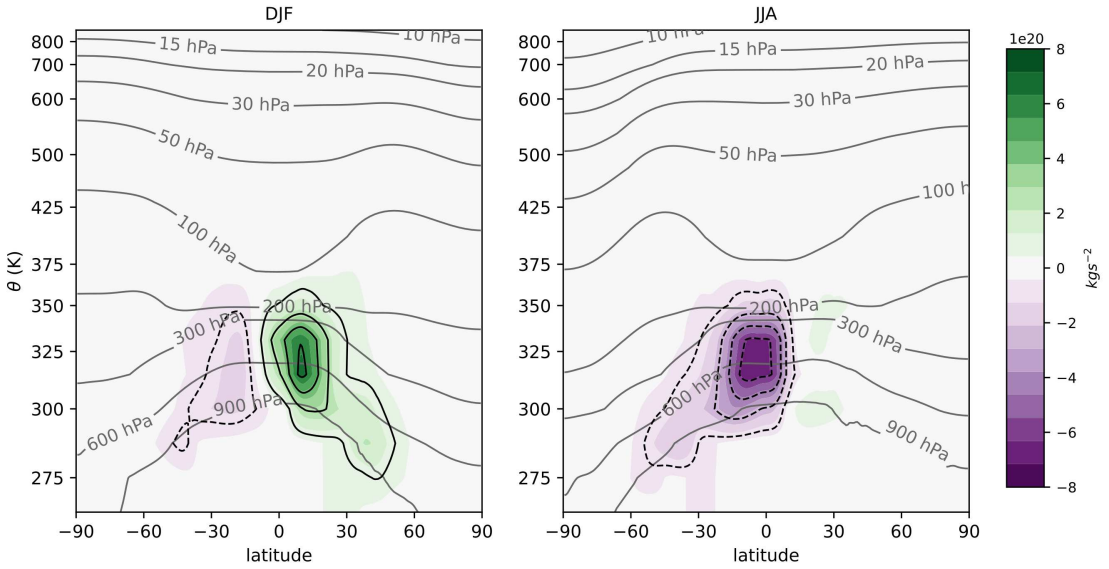

Figure 4.12: Streamfunction of angular momentum flux circulation for DJF and JJA, Ψ_M, on isentropic surfaces from 1979-2018. Units are $N \cdot m$. Pressure contours have been included for orientation.

$$\left(\overline{\rho_\theta \dot{\theta} M}^{\lambda,t} - \overline{X}^{\lambda,t}\right) 2\pi a^2 \cos\varphi \equiv \frac{\partial \Psi_M}{\partial \varphi} \tag{4.4}$$

On the other hand, Figure 4.13 is the stream function for M', which is

$$M' = M - \overline{M}^{GM}, \tag{4.5}$$

where $\overline{M}^{GM}$ is the mass-weighted global average of angular momentum:

$$\overline{M}^{GM} \equiv \left(\int_0^\infty \int_{\pi/2}^{\pi/2} \int_0^{2\pi} (\rho_\theta v M) d\lambda d\varphi d\theta\right)\left(\int_0^\infty \int_{\pi/2}^{\pi/2} \int_0^{2\pi} \rho_\theta d\lambda d\varphi d\theta\right)^{-1}. \tag{4.6}$$

Since M_{GM} is constant in space, the transport of M_{GM} by the mass circulation does not change how angular momentum is distributed throughout the atmosphere. For this reason, the streamfunction, $\Psi_{M'}$, allows us to see the global circulation of angular momentum more clearly. It is defined by:

$$\overline{\rho_\theta v M'}^{\lambda,t} 2\pi a \cos\varphi \equiv \frac{\partial \Psi_{M'}}{\partial \theta} \tag{4.7}$$

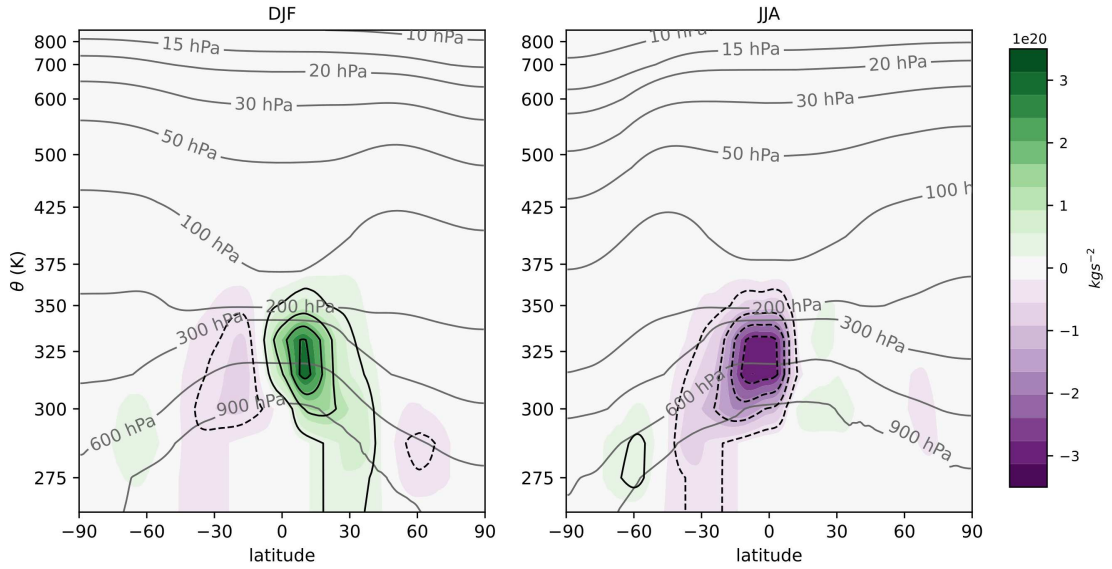

Figure 4.13: Streamfunction of M' flux circulation for DJF and JJA, $\Psi_{M'}$, on isentropic surfaces from 1979-2018. Units are $N \cdot m$. Pressure contours have been included for orientation.

$$\left(\overline{\rho_\theta \dot{\theta} M'}^{\lambda,t} - \overline{X}^{\lambda,t}\right) 2\pi a^2 \cos\varphi \equiv \frac{\partial \Psi_{M'}}{\partial \varphi} \tag{4.8}$$

Comparing Figures 4.12 and 4.13, we can see that the range of $\Psi_{M'}$ is approximately half the range of Ψ_M and the stratosphere shows up more clearly in comparison to the magnitude of tropospheric motion. Ψ_M mimics Ψ_{ρ_θ} in general behavior, and $\Psi_{M'}$ does as well, but to a lesser extent. In both Ψ_M and $\Psi_{M'}$, tropical and subtropical tropospheric circulation of angular momentum generally mirrors the mass circulation with Hadley cells near 10°S and 10°N, that strengthen with the seasons. However, the cell doesn't reach all the way to the poles in $\Psi_{M'}$, like it does in Ψ_{ρ_θ} and Ψ_M. This is because of the downward form drag in the midlatitudes due to baroclinic instability. We are most interested in the stratosphere, so we trim Figure 4.13 to the stratosphere in Figure 4.14.

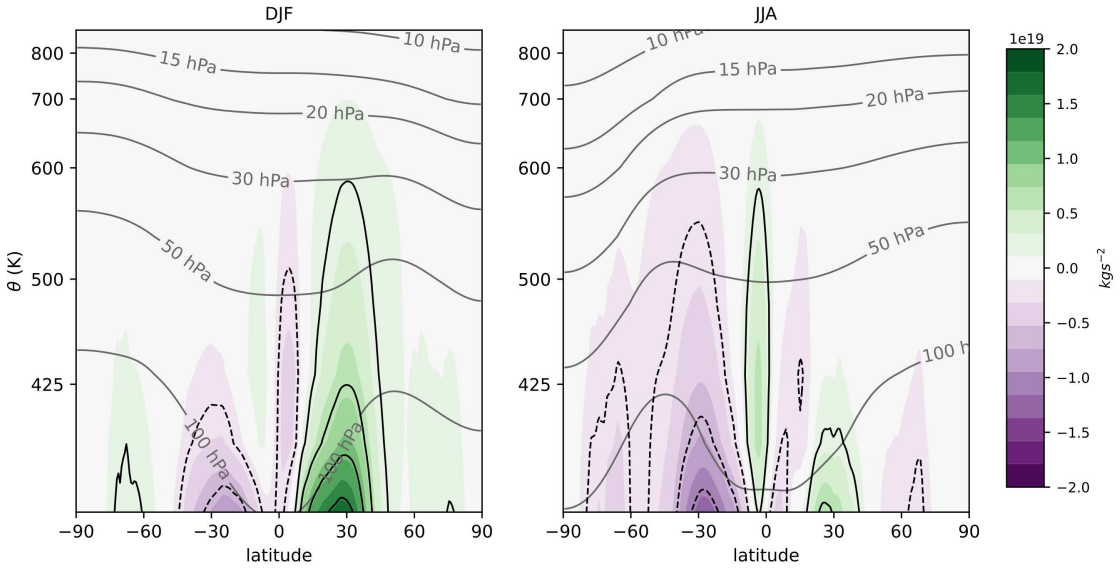

Figure 4.14: M' flux streamfunction in the *stratosphere* for DJF and JJA, $\Psi_{M'}$, on isentropic surfaces from 1979-2018. Units are $N \cdot m$. Pressure contours have been included for orientation.

4.3 Contributions to acceleration of the zonal flow

4.3.1 Decomposition of vertical angular momentum flux

The three components of the vertical Eliassen-Palm flux are from eddy heating, isentropic form drag, and unresolved waves. In an annual average, torques due to isentropic form drag dominate the total vertical Eliassen-Palm flux due to high values in the midlatitudes near the surface (Figure 4.15). However, when we consider the tropical stratosphere and composite over all QBO cycles between 1979 and 2017, the unresolved portion of the total flux dominates (Figure 4.16).

4.3.2 Decomposition of Equation 2.30

In Section 3.5, we discuss considering components of Equation 2.30, but divide each component by $a\cos\varphi$ to obtain each components' contribution to the zonal acceleration. Figure 4.17 shows the proportional relationship of the equatorial QBO response between $\left(\overline{M}^{\lambda}\right)(\partial t)^{-1}$ and $\left(\overline{u}^{\lambda}\right)(\partial t)^{-1}$. Thus, we consider only the contributions to the zonal acceleration.

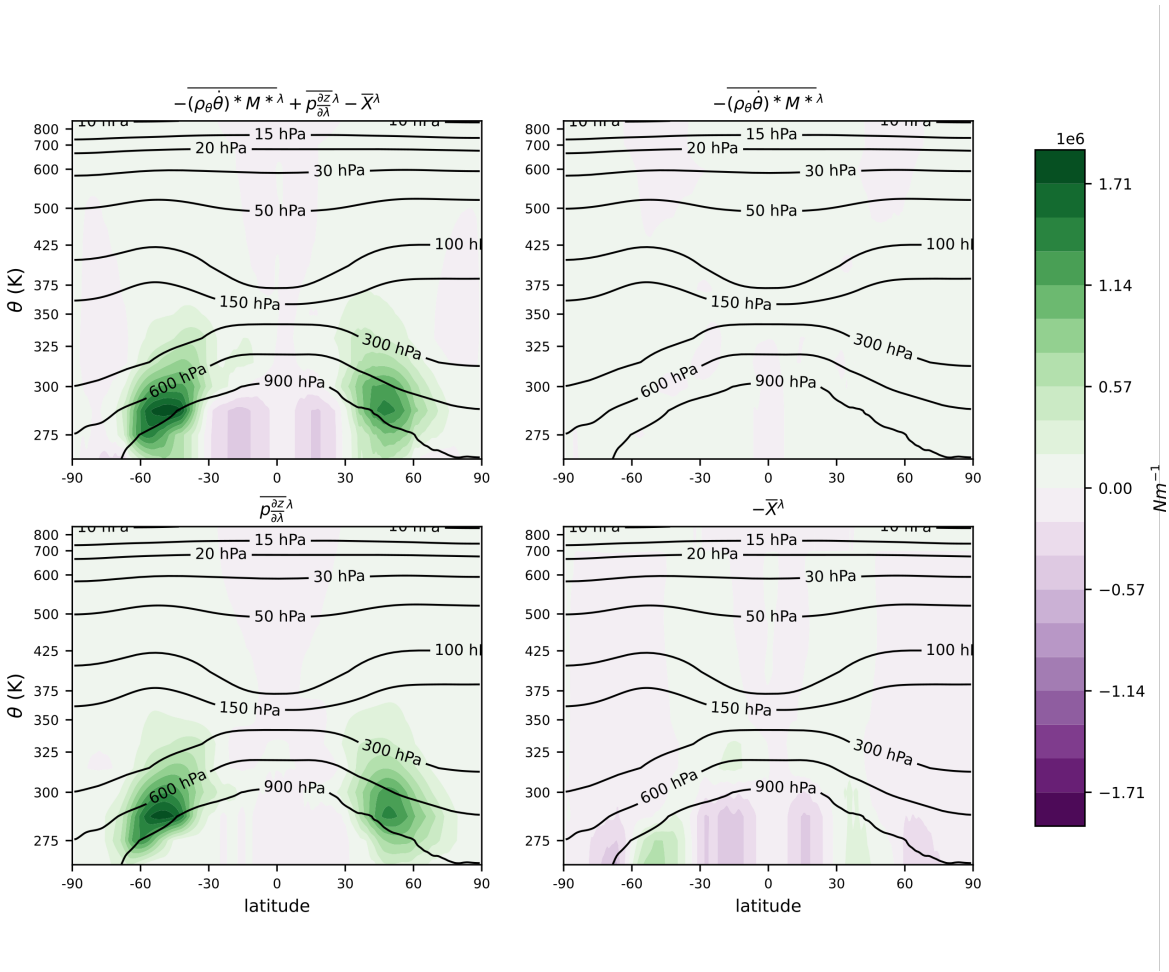

Figure 4.15: Latitude-height plots of zonally and annually averaged total vertical component of the Eliassen-Palm flux, and components due to heating, form drag, and unresolved wave forcing. Pressure contours have been included for orientation.

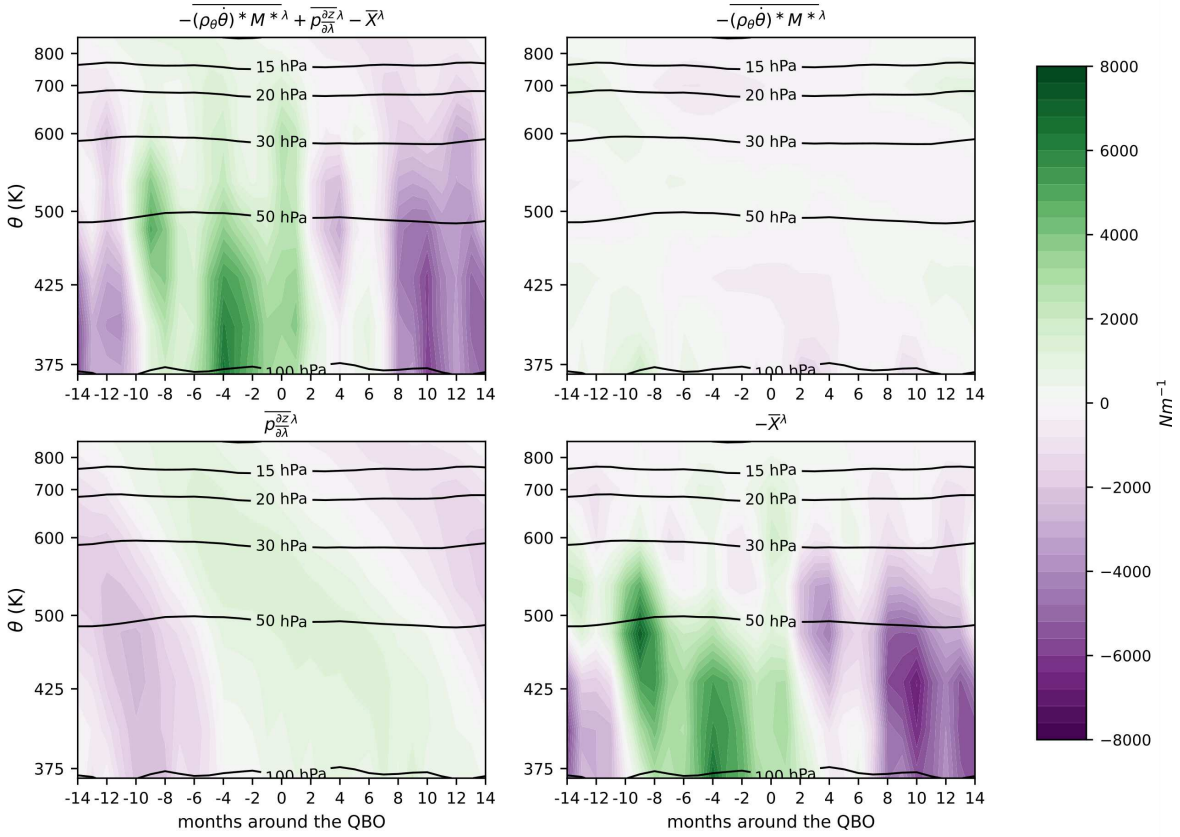

Figure 4.16: QBO composites of de-seasonalized zonally and monthly averaged total vertical Eliassen-Palm flux, and components due to heating, form drag, and unresolved wave forcing. Results have been meridionally averaged from $5^\circ N$ - $5^\circ S$. Pressure contours have been included for orientation. QBO cycles averaged from 1979-2018.

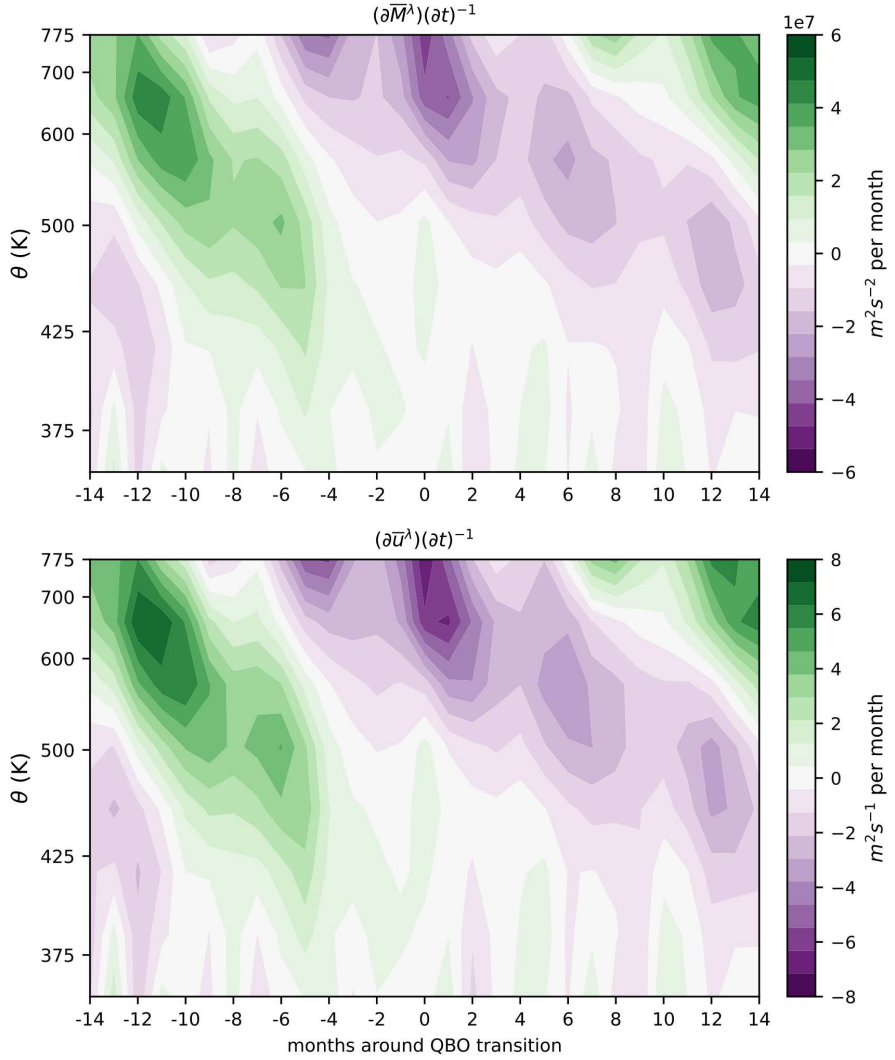

Figure 4.17: QBO composites of de-seasonalized zonally and monthly averaged $\left(\overline{M}^{\lambda}\right)(\partial t)^{-1}$ and $\left(\overline{u}^{\lambda}\right)(\partial t)^{-1}$ on isentropic surfaces. Results have been meridionally averaged from $5°N$ - $5°S$. QBO cycles averaged from 1979-2017.

Figure 4.18 shows the contributions of all components to the zonal acceleration of the QBO in the stratosphere, and Figure 4.19 shows the most important contributions at various isentropic levels to give a better idea of the evolving contribution of each component with height. We also consider the meridional distribution of the contribution of each term to the zonal wind tendency during the westerly to easterly (W2E) transition (Figure 4.20) and the easterly to westerly (E2W) transition (Figure 4.21).

As shown in both Figures 4.19 and 4.18, the 650 K isentropic level (or approximately 25 hPa) the total acceleration reaches its maximum easterly acceleration near the zero-month mark as the QBO transitions from the westerly phase to the easterly phase, and it reaches its maximum westerly acceleration near ± 14 months as the QBO transitions from the easterly to westerly phase. At the 412.5 K level (≈ 75 hPa), in the lower stratosphere, the QBO signal in the zonal wind tendency weakens as the shear zone approaches the tropopause. The levels in between (565K and 452.5K) show maximum and minimum of the QBO signal shifting out of phase with the 650K level as the pattern descends. In the following sections, we consider each component separately, beginning with vertical and meridional advection.

4.3.3 Meridional and vertical advection

Contributions to the zonal wind tendency from meridional and vertical advection are a result of the mean meridional circulation–namely, $\hat{v}$ and $\hat{\dot{\theta}}$. In order to gain a clearer picture of the contributions of meridional and vertical advection to the temporal evolution of the QBO at the equator and the meridional distribution of QBO transition periods, we consider panels *B* and *C* of Figures 4.18, 4.20, and 4.21.

At the equator, vertical advection (orange in Figure 4.19, panel *B* of Figure 4.18) provides the strongest driving force for the maintenance of the QBO, and the meridional advection component has little to no impact (panel *C* of Figure 4.18). However, when we consider the role of vertical advection in the meridional plane (panel *B* in Figures 4.20 and 4.21), the vertical advection damps the poleward flanks of the zonal wind tendency maximum during both phase

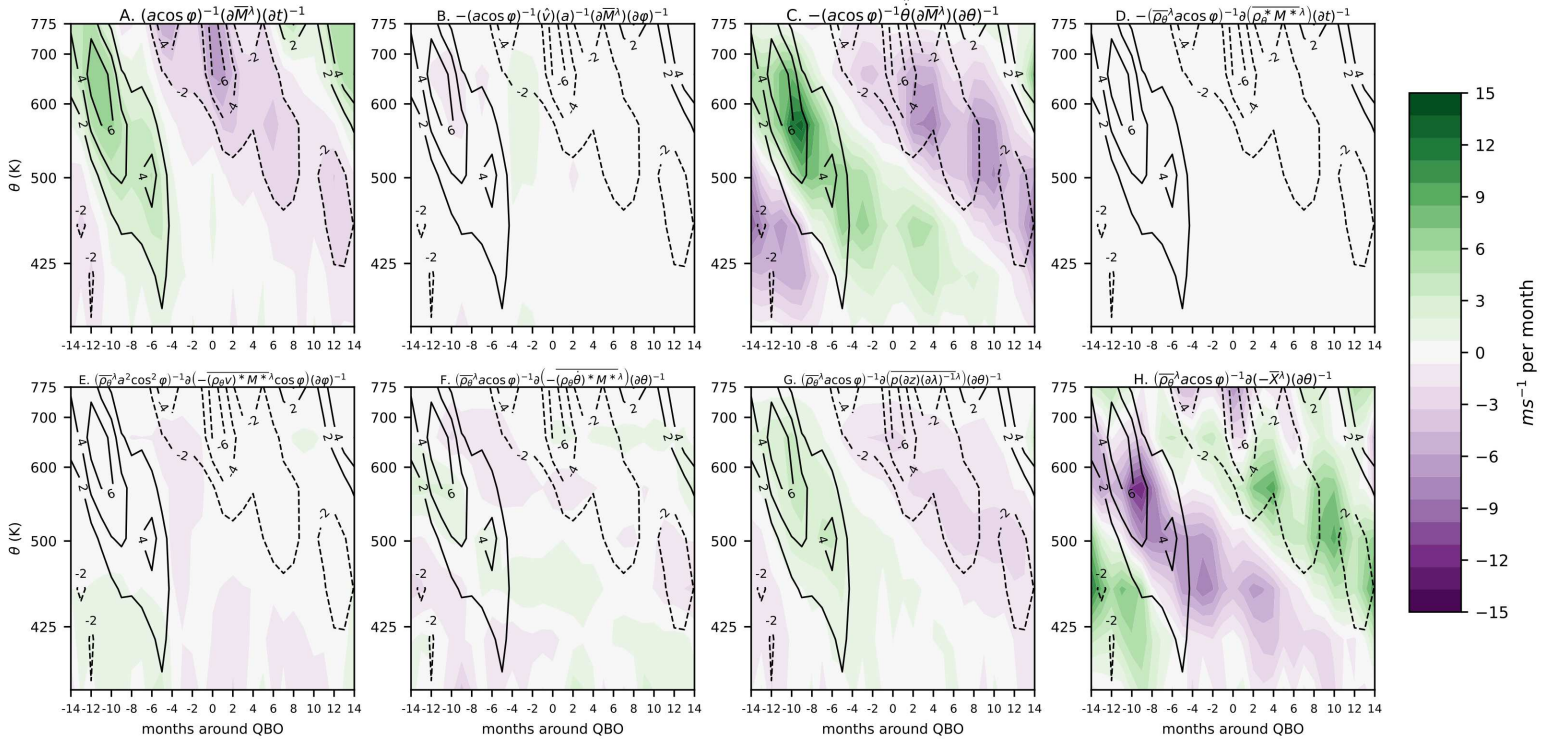

Figure 4.18: QBO composites of de-seasonalized zonally and monthly averaged terms of Equation 2.30 on isentropic surfaces, divided by a to show contribution to zonal acceleration of wind. $(a)^{-1}\frac{\partial\overline{M}^{\lambda}}{\partial t}$ is overlaid on each plot. Results have been meridionally averaged from $5°N$ - $5°S$. QBO cycles averaged from 1979-2017.

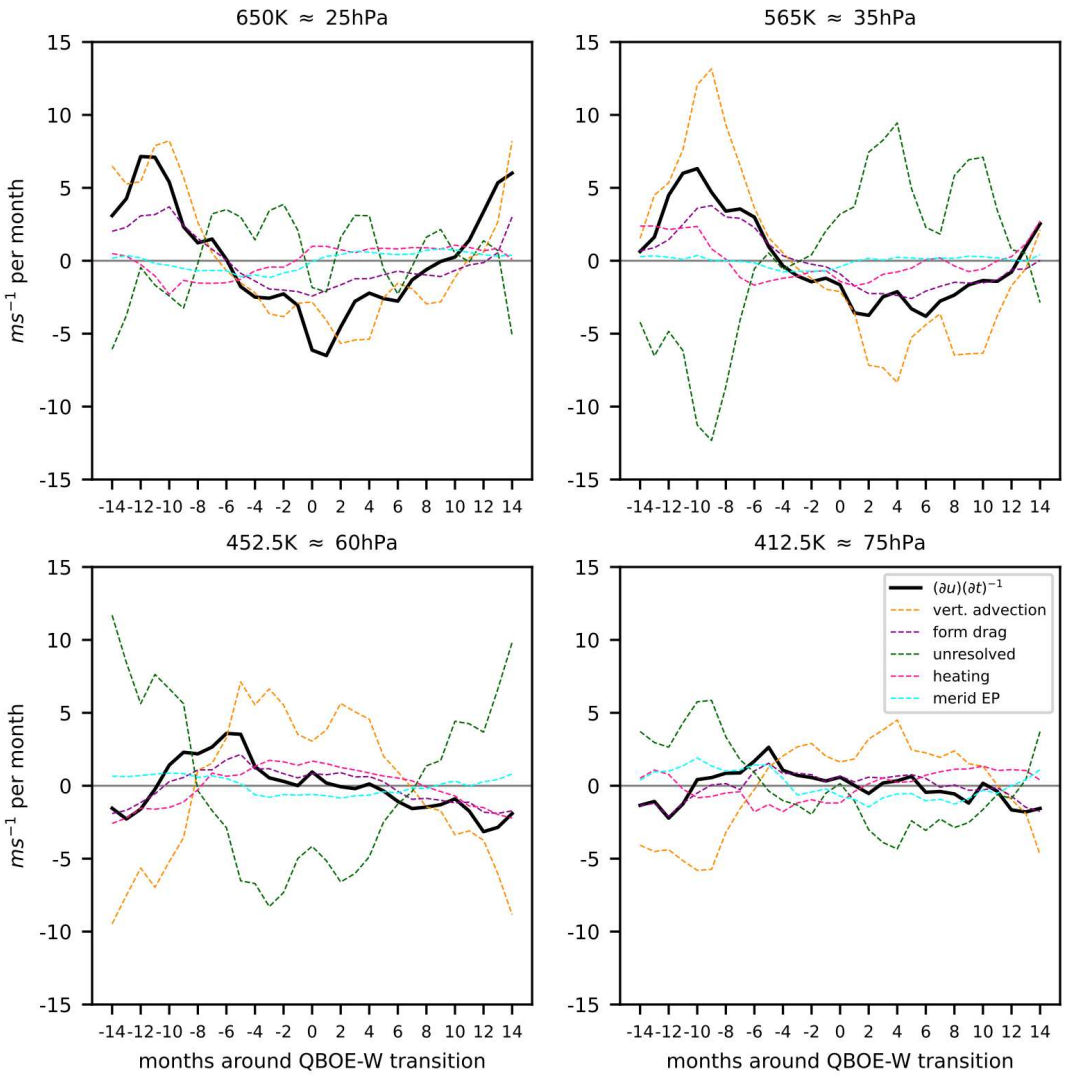

Figure 4.19: Contributions of various components of Equation 2.30 to the zonal acceleration of wind on four different isentropic levels–650K, 565K, 452.5K, and 412.5K. The approximate pressure levels in the Tropics are shown in the figure titles. The solid black line represents the total zonal wind acceleration.

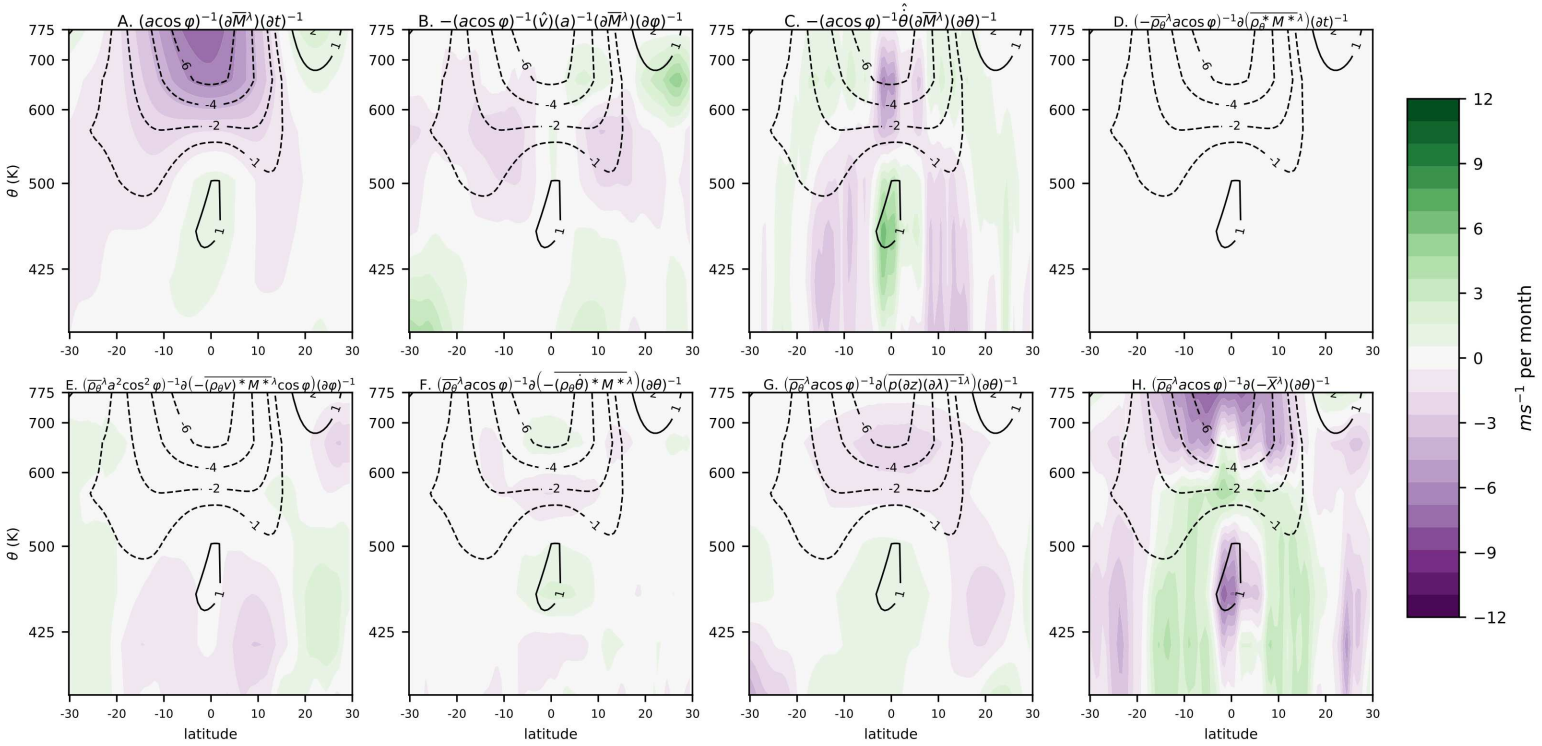

Figure 4.20: Composites of contributions in the meridional plane to zonal wind acceleration by components of Equation 2.30 during months of QBO transition from westerly to easterly phase. Contours of zonal wind acceleration are overlaid on each plot.

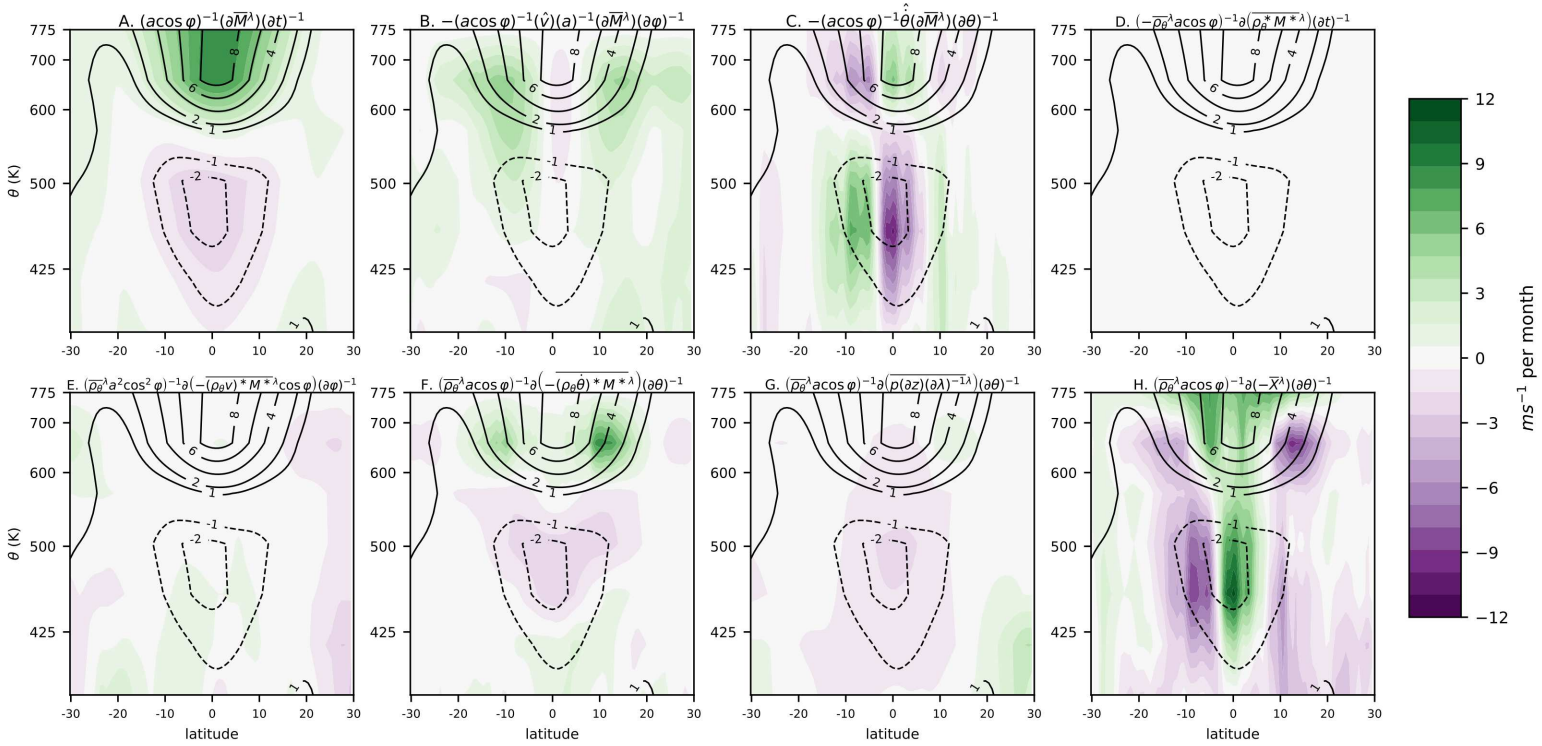

Figure 4.21: Composites of contributions in the meridional plane to zonal wind acceleration by components of Equation 2.30 during months of QBO transition from easterly to westerly phase. Contours of zonal wind acceleration are overlaid on each plot.

transitions at the 650K ~25 hPa) level, as well as in the middle to lower stratosphere between 400K-500K (~80-60hPa). Another notable observation is the overall stronger vertical advection (by a factor of ~2) during the E2W transition.

Meridional advection also acts to strengthen the poleward flanks of the zonal wind tendency maximum. During the E2W transition, this driving occurs at the same upper level as the damping due to vertical advection, effectively cancelling the impact (panel *C* of Figure 4.21). However, during the W2E transition, the largest driving due to meridional advection occurs at a slightly lower level (550K ~ 30-35hPa), producing a zonal wind tendency maximum with a larger meridional and vertical extent (panel *C* of Figure 4.20).

4.3.4 Eliassen-Palm flux divergence (resolved waves)

The meridional Eliassen-Palm (EP) flux divergence and the vertical EP flux divergence due to eddy heating and isentropic form drag correspond to forcing from resolved waves. Each term contributes to the zonal wind tendency in a different way. Per [Giorgetta et al., 2002], resolved waves are primarily produced by parameterized deep convection. Here we focus on panels *E*, *F*, *G* of Figures 4.18, 4.20, and 4.21.

In the equatorial middle stratosphere (at the 452.5K (~ 60 hPa) and 565K (~ 35 hPa) levels), vertical EP flux divergence due to heating positively drives the QBO. However, in the lower stratosphere (412.5K) and the middle-upper stratosphere (650K), the heating term acts to damp the wind signal as it reaches the tropopause and in the middle to upper stratosphere (panel *F* of Figure 4.18, magenta in Figure 4.19). In the meridional plane, eddy heating drives the poleward edges of the zonal wind tendency maximum at the 650K level in both phases, with a more pronounced impact in the E2W phase (panel *F* of Figures 4.20 and 4.21).

Vertical EP flux divergence due to isentropic form drag very clearly mirrors the zonal wind tendency behavior in the equatorial stratosphere, providing a weak but consistent driving force (panel *G* of Figure 4.18 and purple in 4.19). Notably, the isentropic form drag does not exhibit the approximate 6-month pulsing behavior of the zonal wind tendency that is present in the

vertical advection term. This is because the SAO pulsing is a result of the sun's movement; form drag is not affected by solar radiation. The same gentle driving is found throughout the meridional plane, with a less pronounced contribution to the 650K level maximum during the E2W transition and the lobe of negative contribution centered near the 500K level extending into the positive zonal wind tendency (panel *G* in Figure 4.21). The same is not true during the W2E transition (panel *G* in Figure 4.20).

Meridional EP flux divergence near the equator drives the QBO close to the tropopause and appears to damp more with increasing potential temperature; however, its impact at the equator is weaker than the other terms. In the meridional plane, the meridional EP flux divergence acts to damp the poleward sides of the descending region during both transitions, centered at the 425K level, with a more pronounced impact during the W2E transition.

4.3.5 Residual contribution: unresolved waves

At all latitudes and isentropic levels, the residual term acts to diminish the driving or damping impact of other terms (green in Figure 4.19 and panel *H* in Figures 4.18, 4.21, and 4.20). Notably, ERA-Interim lacks a gravity wave parameterization, and data assimilation is utilized to correct the wind signal [Hersbach et al., 2020]. Thus, the residual term encompasses the forcing from unresolved waves required to produce the QBO, combined with the error in the representation of the resolved waves [Kim and Chun, 2015b].

In the equatorial stratosphere, the residual term acts mostly to damp the strength of QBO driving by vertical advection (panel *H* in Figure 4.18 and green in Figure 4.19). The maximum positive contribution of vertical advection to the zonal wind tendency occurs near the 580K level around month -8; whereas the maximum value in zonal wind tendency occurs close the 625K level at month -10. There are also positive contribution pulses at the -4 and +2 month marks and a negative contribution at the -10 month mark, all near the 450K level. While these pulses follow a similar 6-month pattern seen in data, they do not show up in the composited zonal wind tendency. The residual term must act to cancel these characteristics out to produce

the observed zonal wind. This suggests that these particular characteristics in the residual term are corrections to the vertical advection term (panel *C* in Figures 4.18) by data assimilation, and not forcing from subgrid-scale waves.

In higher latitudes, the portion of the residual term that counteracts vertical advection remains dominant component, but to a lesser extent than in the tropics. For example, during the E2W transition, the residual term acts to amplify vertical advection damping of the poleward edges of the upper level zonal wind tendency ($\sim$ 650K) and damp positive accelerations contributed on the poleward edges of the upper level by meridional advection and vertical EP flux divergence from heating (panels *C* and *H* in Figures 4.21). On the other hand, during the W2E transition, the residual term is dominated by cancelling out vertical advection at all latitudes (panels *C* and *H* in Figure 4.20).

There are features in the residual term that do not appear to relate to the cancellation of vertical advection forcing. Considering all panels in Figure 4.21 and 4.20, it appears that features of the zonal wind tendency that are driven only by the residual term are mostly the upper level driving during both phase transitions centered at $\pm 5^\circ$, producing the majority of the latitudinal extent of the zonal wind tendency maxima near 650K. This implies these features are the product of unresolved wave forcing. We investigate this further by considering the contribution of the $G(t,\theta,\varphi)$ to $(\partial\overline{u}^\lambda)(\partial t)^{-1}$ in Figures 4.22, 4.23, and 4.24, which provide a clearer picture of the unresolved contributions not from advection. $G(t,\theta,\varphi)$, defined in 3.27, is repeated here for convenience:

$$G(t,\theta,\varphi) = \frac{-1}{\overline{\rho_\theta}^\lambda a\cos\varphi}\frac{\partial\overline{X}^\lambda}{\partial\theta} + \frac{-\hat{v}}{a^2\cos\varphi}\frac{\partial\overline{M}^\lambda}{\partial\varphi} + \frac{-\hat{\dot{\theta}}}{a\cos\varphi}\frac{\partial\overline{M}^\lambda}{\partial\theta}. \tag{4.9}$$

The most notable aspect of panel *E* of Figure 4.22 is the maximum at the 650K level, which are also observed in the total zonal wind tendency, as was discussed above. This implies that unresolved waves contribute significantly to the observed zonal wind tendency, as is reflected in other studies [Kang et al., 2018; Ern et al., 2014; Kim and Chun, 2015a; Pahlavan et al., 2020]. There is still a positive acceleration near the zero-month mark and 450K level in the residual

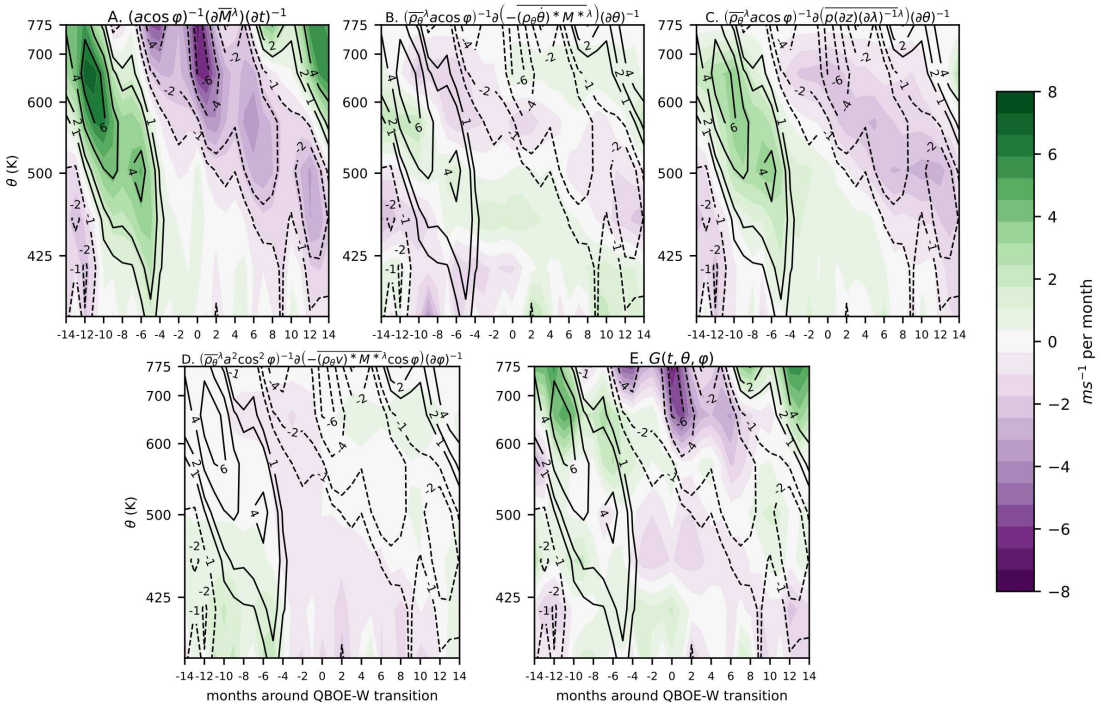

Figure 4.22: QBO composites of de-seasonalized zonally and monthly averaged components of Equation 3.26 on isentropic surfaces, divided by a to show contribution to zonal acceleration of wind. Contours of zonal wind acceleration are overlaid on each plot. Results have been meridionally averaged from $5°N$ - $5°S$. QBO cycles averaged from 1979-2017.

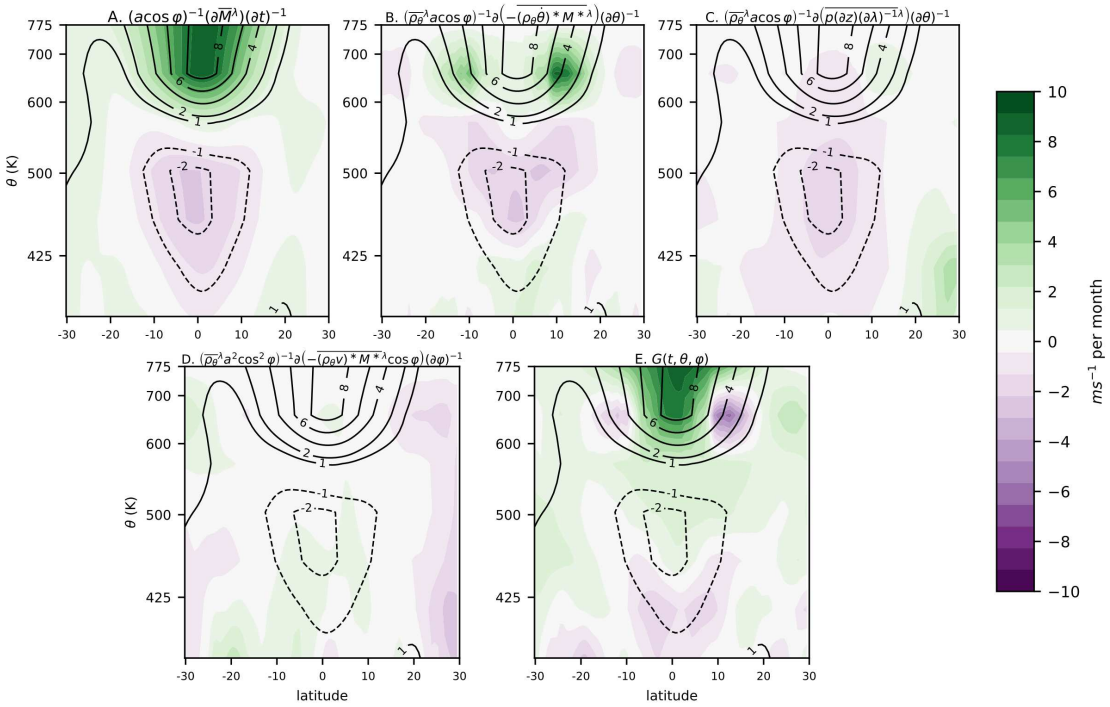

Figure 4.23: Composites of contributions in the meridional plane to zonal wind acceleration by components of Equation 3.26 during months of QBO transition from westerly to easterly phase. Contours of zonal wind acceleration are overlaid on each plot.

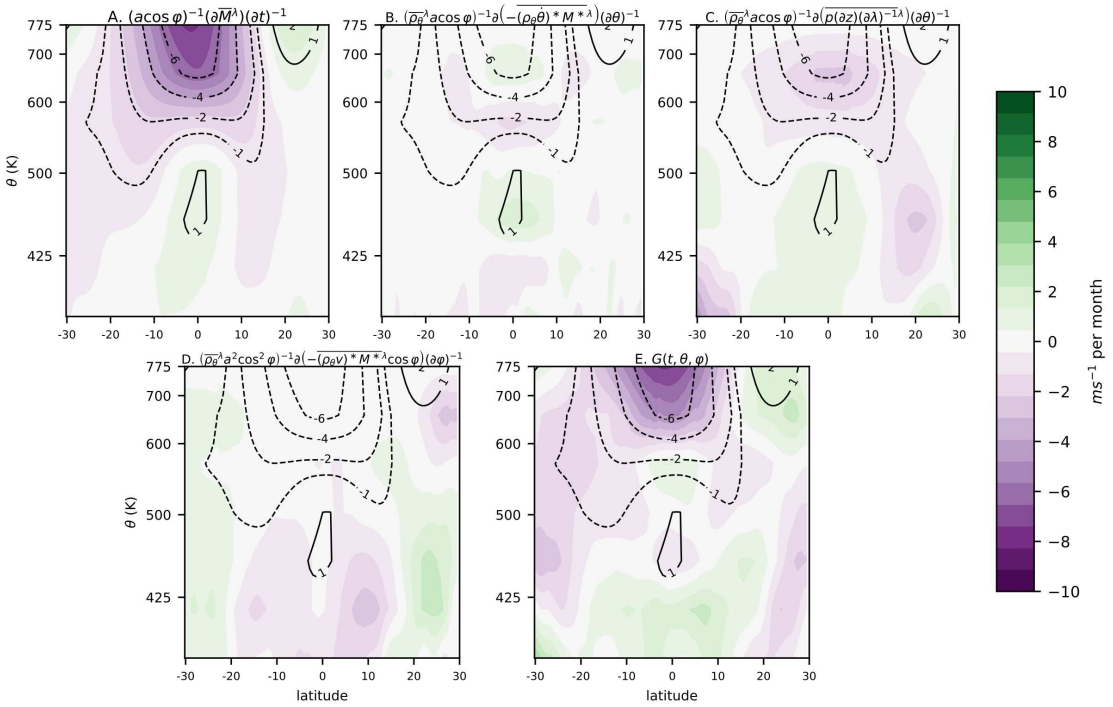

Figure 4.24: Composites of contributions in the meridional plane to zonal wind acceleration by components of Equation 3.26 during months of QBO transition from easterly to westerly phase. Contours of zonal wind acceleration are overlaid on each plot.

contribution that does not appear in the zonal wind tendency; this appears to be a correction of the acceleration produced by vertical EP flux divergence from heating and isentropic form drag. A similar signal can be seen in the meridional EP flux divergence contribution, so it is possible that it is from unresolved waves and not a correction. An important feature that appears are the six-month pulses at the top of the figure, extending from the upper stratosphere. These likely represent the interaction between the SAO and QBO. This is likely a combination of impacts from unresolved waves and resolved waves for which processes are not adequately parameterized.

Figures 4.23 and 4.24 show that $G(t,\theta,\varphi)$ provides the majority of the diving force to the zonal wind tendency maximum near the 700K level during both phase transitions. During the W2E transition, the residual term cancels the subtropical driving force near the 650K level of vertical EP flux divergence from heating (panels *B* and *E* of Figure 4.23). During the E2W transition, the residual term damps some of the equatorial driving in the lower to middle stratosphere from meridional EP flux divergence (panels *D* and *E* from Figure 4.24). During both transitions, the residual term damps the equatorial zonal wind tendency near the 450K isentropic level.

Chapter 5

Summary and Conclusions

5.1 Summary

In 1.4, we designated a goal of quantifying angular momentum fluxes from convectively generated gravity waves and their contribution to the acceleration of the stratospheric equatorial zonal wind. We utilized an indirect method, calculating these values from the isentropic analysis of ERA-Interim.

We computed the total vertical angular momentum flux and decomposed it into contributions from eddy heating, isentropic form drag, and a residual term made up of unresolved wave forcing and correction by data assimilation. The residual angular momentum flux comprised the majority of the total vertical Eliassen-Palm flux, in comparison with more modest contributions due to heating and isentropic form drag.

We characterized the vertical, meridional, and temporal distributions on isentropic surfaces of the contributions of advection, Eliassen-Palm flux divergence, and unresolved wave forcing to the acceleration of zonal wind associated with the transition of the QBO between phases. As was expected, near the Equator, vertical advection dominated over meridional advection in the magnitude of contribution to the zonal wind tendency; however, in the meridional plane, vertical advection damped the subtropical portions of the QBO signal, while the meridional advection contributed a driving force. [Pahlavan et al., 2021] found a similar result when comparing the contributions of meridional and vertical advection.

Forcing from resolved waves was represented by meridional and vertical Eliassen-Palm flux divergence. Vertical Eliassen-Palm flux divergence due to eddy heating was found to drive the zonal wind tendency in the middle equatorial stratosphere and damp in the lower and upper equatorial stratosphere, while driving the subtropical QBO signal. Vertical Eliassen-Palm flux divergence due to isentropic form drag provided consistent weak driving of the QBO signal at

all latitudes throughout the stratosphere. The impact of meridional EP flux divergence is weak at the equator, gently damping with increasing θ; the magnitude of contribution increases as it damps the subtropical QBO signal.

In the consideration of the contribution from the residual term to the zonal wind tendency, we found that a large portion of the residual acceleration contribution is "spent" damping the impact of vertical advection, implying an overestimation of vertical advection in ERA-Interim isentropic analysis. We considered the contribution of the residual term without vertical and meridional advection, in the equatorial stratosphere and in the meridional plane during phase transitions. The majority of upper-level forcing to the QBO was provided by unresolved wave forcing at all latitudes considered. In the lower and middle stratosphere, the contributions are weakened by EP flux divergence terms, with vertical EP flux divergence from eddy heating and isentropic form drag, providing the driving force during phase transitions.

5.2 Discussion

Per Dunkerton [1997], gravity waves provide as much as 75% of the vertical flux of zonal momentum required to drive descent of both phases of the QBO. This is in line with our findings of contributions to the zonal wind tendency by $G(t,\theta,\varphi)$. Kawatani et al. [2010] found that gravity waves of wavenumber greater than 36 are the main contributors to the E2W transition in their QBO simulation. Gravity waves with $k > 36$ would not be resolved in our dataset, so when we compare contributions between phase transitions, we can see that in the meridional plane during the E2W, the unresolved forcing term provides much more driving forcing than other terms (panel *E* in Figure 4.24). During the W2E transition, the vertical EP flux divergence from eddy heating contributed in larger part.

Kim and Chun [2015b] found that vertical advection and unresolved wave forcing were larger than resolved wave forcing during the W2E transition. On the other hand, during the E2W transition, vertical advection and resolved wave forcing are of comparable size (with a substantial decrease in magnitude of vertical advection), and both dominate unresolved wave

forcing. These observations remained true in ERA-Interim and across other reanalyses in their study. It should be noted that this work assumes that the correction of the resolved wave forcing is negligible. In order to truly compare these and determine the relative contributions of vertical advection, resolved wave forcing, and unresolved wave forcing, I would need to disentangle what portion of the residual acceleration is due to unresolved small-scale gravity waves and what is a correction to the resolved wave forcing and advection.

Pahlavan et al. [2021] made the same assumption of the negligibility of the resolved wave forcing correction term. They assumed that the residual tendency was only due to unresolved waves. An important difference between this work and that of Pahlavan et al. [2021] is that ERA5 includes a gravity wave drag (GWD) parameterization that was not included in ERA-Interim. This allowed them to separate the residual into GWD and "analysis correction."

An implication of this work is that the vertical advection term is overestimated, so I was not able to assume that the correction to the resolved scale wave contribution is negligible. One proposed hypothesis is that the vertical advection is overestimated by the data assimilation schemes within ERA-Interim as a mechanism to drive the QBO since there is no parameterized unresolved GWD to produce the observed QBO (personal communication with Peter Jan van Leeuwen of Colorado State University). It would be important in future work to determine errors in the vertical advection due to data assimilation, and investigate why that occurs.

Since we do not have the same capability with ERA-Interim (as ERA5 or other reanalysis products) to separate parameterized GWD and analysis correction, we are left with a similar conclusion to previous studies about the contribution of unresolved waves to the QBO.

5.3 Future Work

In future work, we plan to perform the same analysis with ERA-5 isentropic analysis, comparing its response to ERA-Interim, while also extending the number of years included. I am also interested in extending the work to investigate recent disturbed QBO phase cycles. In particular, I would like to consider and analyze the ways that angular momentum flux divergences

may have differed during those cycles, compared with the relatively consistent signatures of flux during QBO cycles from 1979-2016, as the result of a warming climate.

Bibliography

Alexander, M. J. and Holton, J. R. (1997). A Model Study of Zonal Forcing in the Equatorial Stratosphere by Convectively Induced Gravity Waves. *Journal of the Atmospheric Sciences*, 54(3):408–419.

Alexander, M. J., Holton, J. R., and Durran, D. R. (1995). The Gravity Wave Response above Deep Convection in a Squall Line Simulation. *Journal of the Atmospheric Sciences*, 52(12):2212–2226.

Alexander, M. J. and Pfister, L. (1995). Gravity wave momentum flux in the lower stratosphere over convection. *Geophysical Research Letters*, 22(15):2029–2032.

Andrews, D. G. (1978). Generalized Eliassen-Palm and Charney-Drazin Theorems for Waves oin Axismmetric Mean Flows in Compressible Atmospheres. *Journal of the Atmospheric Sciences*, 35(2):175–185.

Andrews, D. G. (1983). A Finite-Amplitude Eliassen-Palm Theorem in Isentropic Coordinates. *Journal of the Atmospheric Sciences*, 40(8):1877–1883.

Andrews, D. G. (1987). On the interpretation of the Eliassen-Palm flux divergence. *Quarterly Journal of the Royal Meteorological Society*, 113(475):323–338.

Andrews, D. G. and McIntyre, M. E. (1976). Planetary Waves in Horizontal and Vertical Shear: The Generalized Eliassen-Palm Relation and the Mean Zonal Acceleration. *Journal of the Atmospheric Sciences*, 33(11):2031–2048.

Angell, J. K. and Korshover, J. (1964). Quasi-Biennial Variations in Temperature, Total Ozone, and Tropopause Height. *Journal of the Atmospheric Sciences*, 21(5):479–492.

Anstey, J. A., Osprey, S. M., Alexander, J., Baldwin, M. P., Butchart, N., Gray, L., Kawatani, Y., Newman, P. A., and Richter, J. H. (2022). Impacts, processes and projections of the quasi-biennial oscillation. *Nature Reviews Earth & Environment*, 3(9):588–603.

Baldwin, M. P., Gray, L. J., Dunkerton, T. J., Hamilton, K., and Haynes, P. (2001). The Quasi-Biennial Oscillation. *Reviews of Geophysics*, 39(2):179–229.

Barton, C. A., McCormack, J. P., Eckermann, S. D., and Hoppel, K. W. (2019). Optimization of Gravity Wave Source Parameters for Improved Seasonal Prediction of the Quasi-Biennial Oscillation. *Journal of the Atmospheric Sciences*, 76(9):2941–2962.

Belmont, A. D. and Dartt, D. G. (1968). Variation with Longitude of the QBO. *Monthly Weather Review*, 96(11):767–777.

Beres, J. H. (2005). Implementation of a gravity wave source spectrum parameterization dependent on the properties of convection in the Whole Atmosphere Community Climate Model (WACCM). *Journal of Geophysical Research*, 110(D10):D10108.

Bishop, S. (1884). The Equatorial Smoke-Stream From Krakatoa. *The Hawaiian Monthly*, 1(5):106–110.

Bishop, S. (1904). How Hawaiian People Were Won From Savagery. *The Pacific commercial advertiser*.

Booker, J. R. and Bretherton, F. P. (1967). The critical layer for internal gravity waves in a shear flow. *Journal of Fluid Mechanics*, 27(3):513–539.

Brönnimann, S. and Stickler, A. (2013). Aerological observations in the Tropics in the Early Twentieth Century. *Meteorologische Zeitschrift*, 22(3):349–358.

Bushell, A. C., Anstey, J. A., Butchart, N., Kawatani, Y., Osprey, S. M., Richter, J. H., Serva, F., Braesicke, P., Cagnazzo, C., Chen, C., Chun, H., Garcia, R. R., Gray, L. J., Hamilton, K., Kerzenmacher, T., Kim, Y., Lott, F., McLandress, C., Naoe, H., Scinocca, J., Smith, A. K., Stockdale, T. N., Versick, S., Watanabe, S., Yoshida, K., and Yukimoto, S. (2022). Evaluation of the Quasi-Biennial Oscillation in global climate models for the SPARC QBO-initiative. *Quarterly Journal of the Royal Meteorological Society*, 148(744):1459–1489.

Butchart, N. (2022). The stratosphere: a review of the dynamics and variability. *Weather and Climate Dynamics*, 3(4):1237–1272.

Butchart, N., Anstey, J. A., Hamilton, K., Osprey, S., McLandress, C., Bushell, A. C., Kawatani, Y., Kim, Y.-H., Lott, F., Scinocca, J., Stockdale, T. N., Andrews, M., Bellprat, O., Braesicke, P., Cagnazzo, C., Chen, C.-C., Chun, H.-Y., Dobrynin, M., Garcia, R. R., Garcia-Serrano, J., Gray, L. J., Holt, L., Kerzenmacher, T., Naoe, H., Pohlmann, H., Richter, J. H., Scaife, A. A., Schenzinger, V., Serva, F., Versick, S., Watanabe, S., Yoshida, K., and Yukimoto, S. (2018). Overview of experiment design and comparison of models participating in phase 1 of the SPARC Quasi-Biennial Oscillation initiative (QBOi). *Geoscientific Model Development*, 11(3):1009–1032.

Cadet, D. and Teitelbaum, H. (1979). Observational Evidence of Internal Inertia-Gravity Waves in the Tropical Stratosphere. *Journal of the Atmospheric Sciences*, 36(5):892–907.

Choi, H.-J. and Chun, H.-Y. (2011). Momentum Flux Spectrum of Convective Gravity Waves. Part I: An Update of a Parameterization Using Mesoscale Simulations. *Journal of the Atmospheric Sciences*, 68(4):739–759.

Dee, D. P., Uppala, S. M., Simmons, A. J., Berrisford, P., Poli, P., Kobayashi, S., Andrae, U., Balmaseda, M. A., Balsamo, G., Bauer, P., Bechtold, P., Beljaars, A. C. M., Van De Berg, L., Bidlot, J., Bormann, N., Delsol, C., Dragani, R., Fuentes, M., Geer, A. J., Haimberger, L., Healy, S. B., Hersbach, H., Hólm, E. V., Isaksen, L., Kållberg, P., Köhler, M., Matricardi, M., McNally, A. P., Monge-Sanz, B. M., Morcrette, J.-J., Park, B.-K., Peubey, C., De Rosnay, P., Tavolato, C., Thépaut, J.-N., and Vitart, F. (2011). The ERA-Interim reanalysis: configuration and performance of the data assimilation system. *Quarterly Journal of the Royal Meteorological Society*, 137(656):553–597.

Dunkerton, T. J. (1990). Annual Variation of Deseasonalized Mean Flow Acceleration in the Equatorial Lower Stratosphere. *Journal of the Meteorological Society of Japan. Ser. II*, 68(4):499–508.

Dunkerton, T. J. (1991). Nonlinear Propagation of Zonal Winds in an Atmosphere with Newtonian Cooling and Equatorial Wavedriving. *Journal of the Atmospheric Sciences*, 48(2):236–263.

Dunkerton, T. J. (1997). The role of gravity waves in the quasi-biennial oscillation. *Journal of Geophysical Research: Atmospheres*, 102(D22):26053–26076.

Dunkerton, T. J. and Delisi, D. P. (1985). Climatology of the Equatorial Lower Stratosphere. *Journal of the Atmospheric Sciences*, 42(4):376–396.

Dunkerton, T. J. and Delisi, D. P. (1997). Interaction of the quasi-biennial oscillation and stratopause semiannual oscillation. *Journal of Geophysical Research: Atmospheres*, 102(D22):26107–26116.

Ebdon, R. A. (1960). Notes on the wind flow at 50 mb in tropical and sub-tropical regions in January 1957 and January 1958. *Quarterly Journal of the Royal Meteorological Society*, 86(370):540–542.

Egger, J., Weickmann, K., and Hoinka, K.-P. (2007). Angular momentum in the global atmospheric circulation: ANGULAR MOMENTUM IN THE GLOBAL ATMOSPHERE. *Reviews of Geophysics*, 45(4).

Ern, M., Ploeger, F., Preusse, P., Gille, J. C., Gray, L. J., Kalisch, S., Mlynczak, M. G., Russell, J. M., and Riese, M. (2014). Interaction of gravity waves with the QBO: A satellite perspective. *Journal of Geophysical Research: Atmospheres*, 119(5):2329–2355.

Ern, M. and Preusse, P. (2009a). Quantification of the contribution of equatorial Kelvin waves to the QBO wind reversal in the stratosphere. *Geophysical Research Letters*, 36(21):L21801.

Ern, M. and Preusse, P. (2009b). Wave fluxes of equatorial Kelvin waves and QBO zonal wind forcing derived from SABER and ECMWF temperature space-time spectra. *Atmospheric Chemistry and Physics*, 9(12):3957–3986.

Ern, M., Preusse, P., Gille, J. C., Hepplewhite, C. L., Mlynczak, M. G., Russell, J. M., and Riese, M. (2011). Implications for atmospheric dynamics derived from global observations of gravity wave momentum flux in stratosphere and mesosphere. *Journal of Geophysical Research*, 116(D19):D19107.

Fritts, D. C. and Alexander, M. J. (2003). Gravity wave dynamics and effects in the middle atmosphere: MIDDLE ATMOSPHERE GRAVITY WAVE DYNAMICS. *Reviews of Geophysics*, 41(1).

Garcia, R. R., Dunkerton, T. J., Lieberman, R. S., and Vincent, R. A. (1997). Climatology of the semiannual oscillation of the tropical middle atmosphere. *Journal of Geophysical Research: Atmospheres*, 102(D22):26019–26032.

Garfinkel, C. I. and Hartmann, D. L. (2011). The Influence of the Quasi-Biennial Oscillation on the Troposphere in Winter in a Hierarchy of Models. Part I: Simplified Dry GCMs. *Journal of the Atmospheric Sciences*, 68(6):1273–1289.

Geller, M. A., Alexander, M. J., Love, P. T., Bacmeister, J., Ern, M., Hertzog, A., Manzini, E., Preusse, P., Sato, K., Scaife, A. A., and Zhou, T. (2013). A Comparison between Gravity Wave Momentum Fluxes in Observations and Climate Models. *Journal of Climate*, 26(17):6383–6405.

Giorgetta, M. A., Manzini, E., and Roeckner, E. (2002). Forcing of the quasi-biennial oscillation from a broad spectrum of atmospheric waves: SIMULATION OF THE QBO. *Geophysical Research Letters*, 29(8):86–1–86–4.

Gray, L. J., Anstey, J. A., Kawatani, Y., Lu, H., Osprey, S., and Schenzinger, V. (2018). Surface impacts of the Quasi Biennial Oscillation. *Atmospheric Chemistry and Physics*, 18(11):8227–8247.

Gray, L. J. and Pyle, J. A. (1989). A Two-Dimensional Model of the Quasi-biennial Oscillation of Ozone. *Journal of the Atmospheric Sciences*, 46(2):203–220.

Graystone, P. (1959). Meteorological Office Discussion. *The Meteorological Magazine*, 88(1042):113–118.

Guest, F. M., Reeder, M. J., Marks, C. J., and Karoly, D. J. (2000). Inertia–Gravity Waves Observed in the Lower Stratosphere over Macquarie Island. *Journal of the Atmospheric Sciences*, 57(5):737–752.

Hamilton, K. (2012). Sereno Bishop, Rollo Russell, Bishop's Ring and the Discovery of the "Krakatoa Easterlies". *Atmosphere-Ocean*, 50(2):169–175.

Hamilton, K., Wilson, R. J., and Hemler, R. S. (1999). Middle Atmosphere Simulated with High Vertical and Horizontal Resolution Versions of a GCM: Improvements in the Cold Pole Bias and Generation of a QBO-like Oscillation in the Tropics. *Journal of the Atmospheric Sciences*, 56(22):3829–3846.

Harris, L. A., Garza, C., Hatch, M., Parrish, J., Posselt, J., Alvarez Rosario, J. P., Davidson, E., Eckert, G., Wilson Grimes, K., Garcia, J. E., Haacker, R., Horner-Devine, M. C., Johnson, A., Lemus, J., Prakash, A., Thompson, L., Vitousek, P., Martin Bras, M. P., and Reyes, K. (2021). Equitable Exchange: A Framework for Diversity and Inclusion in the Geosciences. *AGU Advances*, 2(2).

Hastenrath, S. (2007). Equatorial zonal circulations: Historical perspectives. *Dynamics of Atmospheres and Oceans*, 43(1-2):16–24.

Hawaii at Manoa, U. o. (2013). Chronicling America (Historic American Newspapers): Pacific Commerical Advertisor.

Hersbach, H., Bell, B., Berrisford, P., Hirahara, S., Horányi, A., Muñoz-Sabater, J., Nicolas, J., Peubey, C., Radu, R., Schepers, D., Simmons, A., Soci, C., Abdalla, S., Abellan, X., Balsamo, G., Bechtold, P., Biavati, G., Bidlot, J., Bonavita, M., Chiara, G., Dahlgren, P., Dee, D., Diamantakis, M., Dragani, R., Flemming, J., Forbes, R., Fuentes, M., Geer, A., Haimberger, L., Healy, S., Hogan, R. J., Hólm, E., Janisková, M., Keeley, S., Laloyaux, P., Lopez, P., Lupu, C., Radnoti,

G., Rosnay, P., Rozum, I., Vamborg, F., Villaume, S., and Thépaut, J. (2020). The ERA5 global reanalysis. *Quarterly Journal of the Royal Meteorological Society*, 146(730):1999–2049.

Holton, J. R. (1979). Equatorial Wave-Mean Flow Interaction: A Numerical Study of the Role of Latitudinal Shear. *Journal of the Atmospheric Sciences*, 36(6):1030–1040.

Holton, J. R. and Lindzen, R. S. (1972). An Updated Theory for the Quasi-Biennial Cycle of the Tropical Stratosphere. *Journal of the Atmospheric Sciences*, 29(6):1076–1080.

Holton, J. R. and Tan, H.-C. (1980). The Influence of the Equatorial Quasi-Biennial Oscillation on the Global Circulation at 50 mb. *Journal of the Atmospheric Sciences*, 37(10):2200–2208.

Horinouchi, T. and Yoden, S. (1998). Wave–Mean Flow Interaction Associated with a QBO-like Oscillation Simulated in a Simplified GCM. *Journal of the Atmospheric Sciences*, 55(4):502–526.

Hsu, Y.-J. G. and Arakawa, A. (1990). Numerical Modeling of the Atmosphere with an Isentropic Vertical Coordinate. *Monthly Weather Review*, 118(10):1933–1959.

Kang, M.-J., Chun, H.-Y., Kim, Y.-H., Preusse, P., and Ern, M. (2018). Momentum Flux of Convective Gravity Waves Derived from an Offline Gravity Wave Parameterization. Part II: Impacts on the Quasi-Biennial Oscillation. *Journal of the Atmospheric Sciences*, 75(11):3753–3775.

Kawatani, Y., Watanabe, S., Sato, K., Dunkerton, T. J., Miyahara, S., and Takahashi, M. (2010). The Roles of Equatorial Trapped Waves and Internal Inertia–Gravity Waves in Driving the Quasi-Biennial Oscillation. Part II: Three-Dimensional Distribution of Wave Forcing. *Journal of the Atmospheric Sciences*, 67(4):981–997.

Kim, Y.-H. and Chun, H.-Y. (2015a). Contributions of equatorial wave modes and parameterized gravity waves to the tropical QBO in HadGEM2. *Journal of Geophysical Research: Atmospheres*, 120(3):1065–1090.

Kim, Y.-H. and Chun, H.-Y. (2015b). Momentum forcing of the quasi-biennial oscillation by equatorial waves in recent reanalyses. *Atmospheric Chemistry and Physics*, 15(12):6577–6587.

Klemp, J. B. and Lilly, D. K. (1978). Numerical Simulation of Hydrostatic Mountain Waves. *Journal of the Atmospheric Sciences*, 35(1):78–107.

Krismer, T. R., Giorgetta, M. A., and Esch, M. (2013). Seasonal aspects of the quasi-biennial oscillation in the Max Planck Institute Earth System Model and ERA-40. *Journal of Advances in Modeling Earth Systems*, 5(2):406–421.

Li, X., Read, P. L., and Andrews, D. G. (1997). Mode selection, wave breaking and parametric sensitivity in the quasi-biennial oscillation. *Quarterly Journal of the Royal Meteorological Society*, 123(543):2041–2068.

Lindzen, R. and Goody, R. (1965). Radiative and Photochemical Processes in Mesospheric Dynamics: Part I, Models for Radiative and Photochemical Processes. *Journal of the Atmospheric Sciences*, 22(4):341–348.

Lindzen, R. D. (1967). Planetary Waves on Beta-Planes. *Monthly Weather Review*, 95(7):441–451.

Lindzen, R. S. (1966a). Radiative and Photochemical Processes in Mesospheric Dynamics: Part II, Vertical Propagation of Long Period Disturbances at the Equator. *Journal of the Atmospheric Sciences*, 23(3):334–343.

Lindzen, R. S. (1966b). Radiative and Photochemical Processes in Mesospheric Dynamics. Part III, Stability of a Zonal Vortex at Mid-Latitudes to Axially Symmetric Disturbances. *Journal of the Atmospheric Sciences*, 23(3):344–349.

Lindzen, R. S. (1966c). Radiative and Photochemical Processes in Mesospheric Dynamics: Part IV, Stability of a Zonal Vortex at Mid-Latitudes to Baroclinic Waves. *Journal of the Atmospheric Sciences*, 23(3):350–359.

Lindzen, R. S. (1971). Equatorial Planetary Waves in Shear. Part I. *Journal of the Atmospheric Sciences*, 28(4):609–622.

Lindzen, R. S. (1987). On the Development of the Theory of the QBO. *Bulletin of the American Meteorological Society*, 68(4):329–337.

Lindzen, R. S. and Holton, J. R. (1968). A Theory of the Quasi-Biennial Oscillation. *Journal of the Atmospheric Sciences*, 25(6):1095–1107.

Lindzen, R. S. and Matsuno, T. (1968). On the Nature of Large Scale Wave Disturbances in the Equatorial Lower Stratosphere. *Journal of the Meteorological Society of Japan. Ser. II*, 46(3):215–220.

Martin, Z., Son, S.-W., Butler, A., Hendon, H., Kim, H., Sobel, A., Yoden, S., and Zhang, C. (2021). The influence of the quasi-biennial oscillation on the Madden–Julian oscillation. *Nature Reviews Earth & Environment*, 2(7):477–489.

Maruyama, T. (1967). Large-Scale Disturbances in the Equatorial Lower Stratosphere. *Journal of the Meteorological Society of Japan. Ser. II*, 45(5):391–408.

Matsuno, T. (1966). Quasi-Geostrophic Motions in the Equatorial Area. *Journal of the Meteorological Society of Japan. Ser. II*, 44(1):25–43.

Mayr, H., Mengel, J., Chan, K., and Huang, F. (2010). Middle atmosphere dynamics with gravity wave interactions in the numerical spectral model: Zonal-mean variations. *Journal of Atmospheric and Solar-Terrestrial Physics*, 72(11-12):807–828.

Nardi, K. M., Baggett, C. F., Barnes, E. A., Maloney, E. D., Harnos, D. S., and Ciasto, L. M. (2020). Skillful All-Season S2S Prediction of U.S. Precipitation Using the MJO and QBO. *Weather and Forecasting*, 35(5):2179–2198.

Pahlavan, H. A., Fu, Q., Wallace, J. M., and Kiladis, G. N. (2021). Revisiting the Quasi-Biennial Oscillation as Seen in ERA5. Part I: Description and Momentum Budget. *Journal of the Atmospheric Sciences*, 78(3):673–691.

Pahlavan, H. A., Wallace, J. M., Fu, Q., and Kiladis, G. N. (2020). Revisiting the Quasi Biennial Oscillation as Seen in ERA5.Part II: Evaluation of Waves and Wave Forcing. *Journal of the Atmospheric Sciences*. Publisher: arXiv Version Number: 1.

Pascoe, C. L. (2005). The quasi-biennial oscillation: Analysis using ERA-40 data. *Journal of Geophysical Research*, 110(D8):D08105.

Plumb, R. A. (1977). The Interaction of Two Internal Waves with the Mean Flow: Implications for the Theory of the Quasi-Biennial Oscillation. *Journal of the Atmospheric Sciences*, 34(12):1847–1858.

Plumb, R. A. and Bell, R. C. (1982a). Equatorial waves in steady zonal shear flow. *Quarterly Journal of the Royal Meteorological Society*, 108(456):313–334.

Plumb, R. A. and Bell, R. C. (1982b). A model of the quasi-biennial oscillation on an equatorial beta-plane. *Quarterly Journal of the Royal Meteorological Society*, 108(456):335–352.

Plumb, R. A. and McEwan, A. D. (1978). The Instability of a Forced Standing Wave in a Viscous Stratified Fluid: A Laboratory Analogue of the Quasi-Biennial Oscillation. *Journal of the Atmospheric Sciences*, 35(10):1827–1839.

Randall, D. A. (2015). *An Introduction to the Global Circulation of the Atmosphere*. Princeton University Press, Princeton, New Jersey, 1 edition.

Reed, R. J. (1960). The circulation of the stratosphere.

Reed, R. J., Campbell, W. J., Rasmussen, L. A., and Rogers, D. G. (1961). Evidence of a downward-propagating, annual wind reversal in the equatorial stratosphere. *Journal of Geophysical Research*, 66(3):813–818.

Richter, J. H., Butchart, N., Kawatani, Y., Bushell, A. C., Holt, L., Serva, F., Anstey, J., Simpson, I. R., Osprey, S., Hamilton, K., Braesicke, P., Cagnazzo, C., Chen, C., Garcia, R. R., Gray, L. J., Kerzenmacher, T., Lott, F., McLandress, C., Naoe, H., Scinocca, J., Stockdale, T. N., Versick, S., Watanabe, S., Yoshida, K., and Yukimoto, S. (2022). Response of the Quasi-Biennial Oscillation to a warming climate in global climate models. *Quarterly Journal of the Royal Meteorological Society*, 148(744):1490–1518.

Russell, F. R. and Symons, G. (1888). The Eruption of Krakatoa and Subsequent Phenomena. Technical report, The Royal Society of London.

Salazar, J. A. (2014). *Multicultural Settler Colonialism and Indigenous Struggle in Hawaii: the Politics of Astronomy on Mauna a Wakea*. PhD thesis, University of Hawaii Manoa.

Sammler, K. G. and Lynch, C. R. (2021). Apparatuses of observation and occupation: Settler colonialism and space science in Hawai'i. *Environment and Planning D: Society and Space*, 39(5):945–965.

Saravanan, R. (1990). A Multiwave Model of the Quasi-biennial Oscillation. *Journal of the Atmospheric Sciences*, 47(21):2465–2474.

Scaife, A. A., Butchart, N., Warner, C. D., Stainforth, D., Norton, W., and Austin, J. (2000). Realistic quasi-biennial oscillations in a simulation of the global climate. *Geophysical Research Letters*, 27(21):3481–3484.

Schenzinger, V., Osprey, S., Gray, L., and Butchart, N. (2017). Defining metrics of the Quasi-Biennial Oscillation in global climate models. *Geoscientific Model Development*, 10(6):2157–2168.

Son, S.-W., Lim, Y., Yoo, C., Hendon, H. H., and Kim, J. (2017). Stratospheric Control of the Madden–Julian Oscillation. *Journal of Climate*, 30(6):1909–1922.

Süring, R. (1910). A. Berson's Bericht über die aerologische Expedition des königlichen aeronautischen Observatoriums nach Ostafrika im Jahre 1908 (Report by A. BERSON about the

aerological expedition of the Royal Aeronautic Observatory to East Africa in 1908). *Meteorologische Zeitschrift*, 27:536–542. (translated and edited by Volken, E. and S. Brönniman-Meteorol. Z. 22 (2013), 343-348).

Takahashi, M. (1996). Simulation of the stratospheric Quasi-Biennial Oscillation using a general circulation model. *Geophysical Research Letters*, 23(6):661–664.

Takahashi, M. (1999). Simulation of the Quasi-Biennial Oscillation in a general circulation model. *Geophysical Research Letters*, 26(9):1307–1310.

Tanaka, H. and Yoshizawa, N. (1985). Quasi-biennial Oscillation and Its Analog under the Assumption of Wave Self-Acceleration. *Journal of the Atmospheric Sciences*, 42(22):2350–2359.

Tegtmeier, S., Anstey, J., Davis, S., Ivanciu, I., Jia, Y., McPhee, D., and Pilch Kedzierski, R. (2020). Zonal Asymmetry of the QBO Temperature Signal in the Tropical Tropopause Region. *Geophysical Research Letters*, 47(24).

Tsuda, T., Murayama, Y., Wiryosumarto, H., Harijono, S. W. B., and Kato, S. (1994). Radiosonde observations of equatorial atmosphere dynamics over Indonesia: 1. Equatorial waves and diurnal tides. *Journal of Geophysical Research*, 99(D5):10491.

Uccellini, L. W. and Koch, S. E. (1987). The Synoptic Setting and Possible Energy Sources for Mesoscale Wave Disturbances. *Monthly Weather Review*, 115(3):721–729.

Uppala, S. M., KÅllberg, P. W., Simmons, A. J., Andrae, U., Bechtold, V. D. C., Fiorino, M., Gibson, J. K., Haseler, J., Hernandez, A., Kelly, G. A., Li, X., Onogi, K., Saarinen, S., Sokka, N., Allan, R. P., Andersson, E., Arpe, K., Balmaseda, M. A., Beljaars, A. C. M., Berg, L. V. D., Bidlot, J., Bormann, N., Caires, S., Chevallier, F., Dethof, A., Dragosavac, M., Fisher, M., Fuentes, M., Hagemann, S., Hólm, E., Hoskins, B. J., Isaksen, L., Janssen, P. A. E. M., Jenne, R., Mcnally, A. P., Mahfouf, J.-F., Morcrette, J.-J., Rayner, N. A., Saunders, R. W., Simon, P., Sterl, A., Trenberth, K. E., Untch, A., Vasiljevic, D., Viterbo, P., and Woollen, J. (2005). The ERA-40 re-analysis. *Quarterly Journal of the Royal Meteorological Society*, 131(612):2961–3012.

Veryard, R. and Ebdon, R. A. (1961). Fluctuations in the tropical stratospheric winds. *The Meteorology Magazine*, 90(1066):125–143.

Wallace, J. M. (1967). A Note on the Role of Radiation in the Biennial Oscillation. *Journal of the Atmospheric Sciences*, 24(5):598–599.

Wallace, J. M. (1973). General circulation of the tropical lower stratosphere. *Reviews of Geophysics*, 11(2):191.

Wallace, J. M. and Holton, J. R. (1968). A Diagnostic Numerical Model of the Quasi-Biennial Oscillation. *Journal of the Atmospheric Sciences*, 25(2):280–292.

Wallace, J. M. and Kousky, V. E. (1968). Observational Evidence of Kelvin Waves in the Tropical Stratosphere. *Journal of the Atmospheric Sciences*, 25(5):900–907.

Wang, B. (2003). Kelvin Waves. In *Encyclopedia of Atmospheric Sciences*, pages 1062–1068. Elsevier.

Wang, J., Kim, H., and Chang, E. K. M. (2018). Interannual Modulation of Northern Hemisphere Winter Storm Tracks by the QBO. *Geophysical Research Letters*, 45(6):2786–2794.

Wheeler, M. and Kiladis, G. N. (1999). Convectively Coupled Equatorial Waves: Analysis of Clouds and Temperature in the Wavenumber–Frequency Domain. *Journal of the Atmospheric Sciences*, 56(3):374–399.

Xue, X.-H., Liu, H.-L., and Dou, X.-K. (2012). Parameterization of the inertial gravity waves and generation of the quasi-biennial oscillation: IGW IN WACCM AND GENERATION OF QBO. *Journal of Geophysical Research: Atmospheres*, 117(D6):n/a–n/a.

Yanai, M. and Maruyama, T. (1966). Stratospheric Wave Disturbances Propagating over the Equatorial Pacific. *Journal of the Meteorological Society of Japan. Ser. II*, 44(5):291–294.

Appendix A

Wave Driving of the QBO

Vertically propagating waves contribute easterly and westerly acceleration to the equatorial stratospheric zonal flow by vertical flux of zonal momentum [Pahlavan et al., 2021]. The waves most capable of contributing to the QBO are either those with slow vertical group velocity with absorption rates such that they reach their critical levels in QBO shear zones or those with fast vertical group velocity with a phase speed within the wind speed of the stratospheric wind flow [Dunkerton, 1997]. Waves with too slow of a propagation speed are unable to make it past the tropopause, and those with vertical group propagation too fast and with phase speeds outside the range of speeds propagate transparently through the QBO [Li et al., 1997]. The waves with long wavelengths and low frequencies are more likely to be resolved by models and reanalysis datasets; whereas smaller scale gravity waves have wavelengths too small and periods too short to be resolved, so parameterization is needed. This produces uncertainty in analysis and quantification of wave-driving of the QBO [Pahlavan et al., 2021].

The waves most important to the driving of the QBO are equatorial Kelvin waves, Rossby-gravity waves, inertia-gravity waves, and small-scale convectively generated gravity waves. According to Pahlavan et al. [2021], the westerly zonal tendency is mostly driven by Kelvin waves and small-scale gravity waves ($\lambda < 2000$ km), and easterly zonal tendency is mainly driven by the same small-scale gravity waves, as well as modest contributions from inertia-gravity waves and mixed Rossby-gravity waves.

Kelvin waves and other equatorially trapped waves decay with increasing latitude as the Coriolis parameter increases. Atmospheric equatorial Kelvin waves propagate vertically and entirely westerly in the horizontal plane, with characteristic phase speeds of 20 - 80 m s^{-1} with vertical wavelengths approximately 10-12 km. They form in the troposphere in response to diabatic heating [Wang, 2003]. According to Ern and Preusse [2009a,b], Kelvin waves explain 30-50% of the QBO, but make up only 20-35% of the total wave forcing contribution. Kim and

Chun [2015b] showed with ERA-Interim that forcing by Kelvin waves dominates net forcing by all equatorial wave modes (3-9 m s^{-1} per month vs 3-11 m s^{-1} per month), but that contribution was found to be weaker when performing analysis on interpolated pressure levels than on native model levels.

Mixed Rossby-gravity waves (also known as Yanai or Yanai-Maruyama waves) are also equatorially trapped waves. They travel in both easterly and westerly directions, but their QBO contribution is mostly easterly. The typical vertical wavelength is between 4-8 km [Yanai and Maruyama, 1966; Dunkerton, 1991; Wheeler and Kiladis, 1999]. Equatorially trapped inertia-gravity waves can travel either westerly or easterly, but contribute easterly acceleration to the QBO [Cadet and Teitelbaum, 1979]. They are characterized by short vertical wavelengths and high phase speeds [Baldwin et al., 2001]. These low frequency waves have been observed as the result of tropical jet stream instabilities, creating a pathway for possible jet stream-QBO teleconnections [Uccellini and Koch, 1987; Guest et al., 2000].

Gravity waves with zonal wavelengths smaller than 2000 km contribute easterly and westerly momentum to the QBO. These waves are generated by deep convection and orography, but the non-orographic waves are the most dominant contributors to the QBO, as the tropics are not very mountainous [Baldwin et al., 2001]. Buoyancy driven by latent heating produces vertical motions within clouds, exciting gravity waves [Fritts and Alexander, 2003]. These waves are observed to have larger amplitudes in the equatorial stratosphere than in the middle latitudes [Tsuda et al., 1994]. In westerly shear zones (during the east-to-west (E2W) transition), small scale gravity (SSG) wave forcing is approximately 3.4-6.0 m s^{-1} per month, which is smaller than contributions from resolved-scale waves (Kelvin waves in particular). In easterly shear zones (W2E), SSG forcing is estimated to be 3.1-6.0 m s^{-1} per month, which is larger than the contribution from resolved waves (both Kelvin and inertia-gravity waves) at that time [Kim and Chun, 2015b; Kang et al., 2018].

Appendix B

Discretization

Before any discretization, we applied the mass budget correction described in the previous section to the meridional wind. Hereafter, we refer to the corrected wind as v without a prime. For notation, i, j, k, l are the temporal, meridional, vertical, and zonal indices, respectively. Figure B.1 is a schematic showing the notation for the indices for latitude and isentropic levels, and the "half-levels" where many variables lie.

By the definition of pseudodensity (Equation 2.2), since pressure exists on "full" levels, pseudodensity must lie on "half" levels. We calculate pseudodensity on $k \pm \frac{1}{2}$ levels:

$$\rho_{\theta_{[k+\frac{1}{2}]}} = \frac{-1}{g}\frac{\partial p}{\partial \theta}\Big|_{k+\frac{1}{2}} = \frac{-1}{g}\frac{p_{k+1}-p_k}{\theta_{k+1}-\theta_k} \tag{B.1}$$

The equation that we use to compute vertical angular momentum flux convergence due to unresolved wave forcing and any other residual forcing is Equation 3.22, repeated here for convenience:

$$\frac{-\partial \overline{X}^{\lambda}}{\partial \theta} = \overline{\rho_\theta}^{\lambda}\left(\frac{\partial \overline{M}^{\lambda}}{\partial t} + \frac{\hat{v}}{a}\frac{\partial \overline{M}^{\lambda}}{\partial \varphi} + \hat{\dot{\theta}}\frac{\partial \overline{M}^{\lambda}}{\partial \theta}\right) + \frac{\partial}{\partial t}\left(\overline{\rho_\theta {}^* M^*}^{\lambda}\right) - \nabla \cdot \mathbf{IEPF}. \tag{B.2}$$

We discretize B.2:

$$\begin{aligned}\frac{-\partial \overline{X}^{\lambda,t}}{\partial \theta}\Big|_{[i,j+\frac{1}{2},k+\frac{1}{2}]} = {} & \overline{\rho_\theta}^{\lambda,t}_{[i,j+\frac{1}{2},k+\frac{1}{2}]}\left(\frac{\partial \overline{M}^{\lambda}}{\partial t}_{[i,j+\frac{1}{2},k+\frac{1}{2}]}\right) + \\ & + \overline{\rho_\theta}^{\lambda,t}_{[i,j+\frac{1}{2},k+\frac{1}{2}]}\left(\frac{\hat{v}_{[i,j+\frac{1}{2},k+\frac{1}{2}]}}{a}\frac{\partial \overline{M}^{\lambda,t}}{\partial \varphi}_{[i,j+\frac{1}{2},k+\frac{1}{2}]} + \hat{\dot{\theta}}_{[i,j+\frac{1}{2},k+\frac{1}{2}]}\frac{\partial \overline{M}^{\lambda,t}}{\partial \theta}_{[i,j+\frac{1}{2},k+\frac{1}{2}]}\right) + \\ & + \frac{\partial}{\partial t}\left(\overline{\rho_\theta {}^* M^*}^{\lambda}\right)_{[i,j+\frac{1}{2},k+\frac{1}{2}]} - \nabla \cdot \mathbf{IEPF}_{[i,j+\frac{1}{2},k+\frac{1}{2}]}.\end{aligned} \tag{B.3}$$

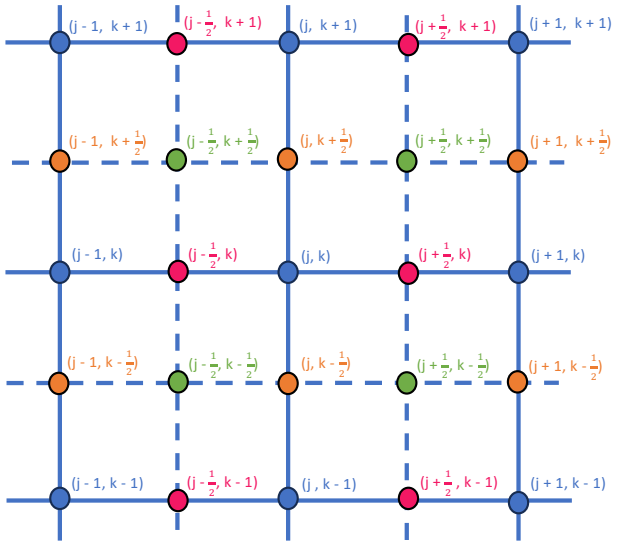

Figure B.1: Schematic of notation for latitude levels (j) and isentropic levels (k). Different colors are used for where variables can lie.

We walk through each term of B.3 and talk about its discretization. We begin with $\overline{\rho_\theta}^{\lambda,t}_{[i,j+\frac{1}{2},k+\frac{1}{2}]}$. The zonal average of ρ_θ at each time step, which already exists on vertical "half" levels ($k \pm \frac{1}{2}$), is linearly interpolated to meridional "half" levels ($j \pm \frac{1}{2}$), and is then averaged over each month. The time tendency of $\overline{M}$ is discretized and computed in the following manner:

$$\frac{\partial \overline{M}^{\lambda}}{\partial t}_{[i,j,k]} = \frac{\overline{M}^{\lambda}_{[i+\frac{1}{2},j,k]} - \overline{M}^{\lambda}_{[i-\frac{1}{2},j,k]}}{\Delta t}, \tag{B.4}$$

and then linearly interpolated to vertical and meridional half levels before substitution into B.3. The values of $\overline{M}^{\lambda}$ at $i \pm \frac{1}{2}$ time steps are taken the first day of the month of interest and the first day of the following month, and $\Delta t = 1$ month, so the resulting time tendency is the change in zonally averaged angular momentum over a month.

We move to the next term in B.3, the meridional advection term. The mass-weighted zonal average of the meridional wind, $\hat{v}$, is computed directly by dividing the zonal average of meridional mass flux ($\overline{\rho_\theta v}^{\lambda}$) by the zonal average of the pseudodensity ($\overline{\rho_\theta}^{\lambda}$). The resulting $\hat{v}$ is then linearly interpolated to meridional half levels and monthly averaged, then substituted into B.3.

The meridional gradient of angular momentum is discretized and computed in the following manner:

$$\frac{\partial \overline{M}^{\lambda,t}}{\partial \varphi}_{[i,j+\frac{1}{2},k]} = \frac{\overline{M}^{\lambda,t}_{[i,j+1,k]} - \overline{M}^{\lambda,t}_{[i,j,k]}}{\Delta\varphi}, \tag{B.5}$$

where $\overline{M}^{\lambda,t}$ is already monthly and zonally averaged. The resulting gradient is linearly interpolated to vertical half levels and substituted into B.3.

For the vertical advection term, we first compute the mass-weighted zonal average of the heating rate, $\hat{\dot{\theta}}$. We do that using continuity. We begin with Equation 2.3, repeated here for convenience:

$$\frac{\partial \rho_\theta}{\partial t} + \frac{1}{a\cos\varphi}\frac{\partial}{\partial \varphi}\left(\rho_\theta v \cos\varphi\right) + \frac{1}{a\cos\varphi}\frac{\partial}{\partial \lambda}\left(\rho_\theta u\right) + \frac{\partial}{\partial \theta}\left(\rho_\theta \dot{\theta}\right) = 0. \tag{B.6}$$

We rearrange and discretize this equation in the following manner to isolate the vertical gradient of vertical mass flux:

$$\begin{aligned}\frac{\partial}{\partial \theta}\left(\rho_\theta \dot{\theta}\right)\Big|_{[i,j+\frac{1}{2},k+\frac{1}{2},l]} = &-\frac{\partial \rho_\theta}{\partial t}\Big|_{[i,j+\frac{1}{2},k+\frac{1}{2},l]} - \\ &\left(a\cos\varphi_{[j+\frac{1}{2}]}\right)^{-1}\left(\frac{\partial}{\partial \varphi}\left(\rho_\theta v\cos\varphi\right)\Big|_{[i,j+\frac{1}{2},k+\frac{1}{2},l]} + \frac{\partial}{\partial \lambda}\left(\rho_\theta u\right)\Big|_{[i,j+\frac{1}{2},k+\frac{1}{2},l]}\right)\end{aligned} \tag{B.7}$$

We walk through each term of B.7. The time tendency of pseudodensity is computed in the following manner:

$$\frac{\partial \rho_\theta}{\partial t}\Big|_{[i,j,k+\frac{1}{2},l]} = \frac{\rho_{\theta_{[i+1,j,k+\frac{1}{2},l]}} - \rho_{\theta_{[i,j,k+\frac{1}{2},l]}}}{\Delta t}. \tag{B.8}$$

In this instance, Δt is 6 hours, and we forward-difference to get the time tendency. The result is linearly interpolated to meridional half-levels before substitution into B.7.

In order to compute the meridional and zonal mass flux divergence terms of B.7, some variables must first be interpolated to vertical and meridional half-levels. For the meridional mass

flux divergence term, meridional wind, v, already exists on vertical half-levels, as was shown in section 3.2; as does pseudodensity, ρ_θ, by definition, so those can be left as is. However for the denominator, latitude itself, φ, must be interpolated to meridional half-levels. The meridional mass flux divergence term is discretized in the following manner:

$$\left(a\cos\varphi_{[j+\frac{1}{2}]}\right)^{-1}\frac{\partial}{\partial\varphi}\left(\rho_\theta v\cos\varphi\right)\Big|_{[i,j+\frac{1}{2},k+\frac{1}{2},l]} = \frac{\rho_{\theta_{[i,j+1,k+\frac{1}{2},l]}}v_{[i,j+1,k+\frac{1}{2},l]}\cos\varphi_{[j+1]} - \rho_{\theta_{[i,j,k+\frac{1}{2},l]}}v_{[i,j,k+\frac{1}{2},l]}\cos\varphi_{[j]}}{\left(a\cos\varphi_{[j+\frac{1}{2}]}\right)\left(\varphi_{j+1}-\varphi_j\right)} \tag{B.9}$$

For the zonal mass flux divergence, zonal wind must first be linearly interpolated to vertical half-levels. The zonal mass flux divergence term is discretized in the following manner:

$$\left(a\cos\varphi_{[j]}\right)^{-1}\frac{\partial}{\partial\lambda}\left(\rho_\theta u\right)\Big|_{[i,j,k+\frac{1}{2},l]} = \frac{\rho_{\theta_{[i,j,k+\frac{1}{2},l+1]}}u_{[i,j,k+\frac{1}{2},l+1]} - \rho_{\theta_{[i,j,k+\frac{1}{2},l]}}u_{[i,j,k+\frac{1}{2},l]}}{\left(a\cos\varphi_{[j]}\right)\left(\lambda_{l+1}-\lambda_l\right)}, \tag{B.10}$$

with

$$\left(a\cos\varphi_{[j]}\right)^{-1}\frac{\partial}{\partial\lambda}\left(\rho_\theta u\right)\Big|_{[i,j,k+\frac{1}{2},-1]} = \frac{\rho_{\theta_{[i,j,k+\frac{1}{2},0]}}u_{[i,j,k+\frac{1}{2},0]} - \rho_{\theta_{[i,j,k+\frac{1}{2},-1]}}u_{[i,j,k+\frac{1}{2},-1]}}{\left(a\cos\varphi_{[j]}\right)\left(\lambda_0-\lambda_{-1}\right)}, \tag{B.11}$$

so that the computation "wraps" around the latitude circle, where $l=-1$ is the last longitudinal index and $l=0$ is the first. Meridional mass flux divergence is computed using a central differencing scheme in latitude, and zonal mass flux divergence is computed using forward differencing in longitude. Zonal mass flux divergence must be linearly interpolated to meridional half levels before substitution into B.7.

Subsituting all of the above into B.7, we directly compute $\frac{\partial}{\partial\theta}\left(\rho_\theta\dot{\theta}\right)$. We want a formula for numerical integration of $\frac{\partial}{\partial\theta}\left(\rho_\theta\dot{\theta}\right)$ in order to solve for $\rho_\theta\dot{\theta}$. We begin by discretizing the left-hand side of B.7:

$$\frac{\partial}{\partial\theta}\left(\rho_\theta\dot{\theta}\right)\Big|_{[i,j+\frac{1}{2},k+\frac{1}{2},l]} = \frac{\left(\rho_\theta\dot{\theta}\right)_{[i,j+\frac{1}{2},k+1,l]} - \left(\rho_\theta\dot{\theta}\right)_{[i,j+\frac{1}{2},k,l]}}{\theta_{[k+1]} - \theta_{[k]}}. \tag{B.12}$$

Rearranging, we have the integration formula for the vertical mass flux (which is the mass-weighted heating rate in isentropic coordinates):

$$\left(\rho_\theta\dot{\theta}\right)_{[i,j+\frac{1}{2},k+1,l]} = \left(\rho_\theta\dot{\theta}\right)_{[i,j+\frac{1}{2},k,l]} + \left(\frac{\partial}{\partial\theta}\left(\rho_\theta\dot{\theta}\right)\Big|_{[i,j+\frac{1}{2},k+\frac{1}{2},l]}\right)\left(\theta_{[k+1]} - \theta_{[k]}\right). \tag{B.13}$$

We integrate downward with $k = 0$ is the "top" level, and we make the assumption that vertical mass flux at the top of the model is zero, or $\rho_\theta\dot{\theta}_{[i,j+\frac{1}{2},0,l]} = 0$. This is not a perfect assumption since the top of the model doesn't represent the top of the real atmosphere. This is something to consider as a possible error source in the resulting heating rate term.

We can take the zonal and monthly average of the resulting vertical mass flux, $\overline{\rho_\theta\dot{\theta}}^{\lambda,t}$, and divide by the zonal and monthly average of the pseudodensity (linearly interpolated to half meridional levels) to produce the mass-weighted zonal average of the heating rate:

$$\hat{\dot{\theta}}_{[i,j+\frac{1}{2},k+\frac{1}{2}]} = \frac{\overline{\rho_\theta\dot{\theta}}^{\lambda,t}_{[i,j+\frac{1}{2},k+\frac{1}{2}]}}{\overline{\rho_\theta}^{\lambda,t}_{[i,j+\frac{1}{2},k+\frac{1}{2}]}}. \tag{B.14}$$

This is the first component of the vertical advection term in B.3. Continuing to the next term in B.3, the vertical gradient of angular momentum is computed in the following manner:

$$\frac{\partial\overline{M}^{\lambda,t}}{\partial\theta}_{[i,j,k+\frac{1}{2}]} = \frac{\overline{M}^{\lambda,t}_{[i,j,k+1]} - \overline{M}^{\lambda,t}_{[i,j,k]}}{\theta_{k+1} - \theta_k}, \tag{B.15}$$

and is then linearly interpolated to meridional half levels before substitution into B.3. Continuing to the next term in B.3, which we will refer to as the "eddy transience" term. First, the zonal average of angular momentum, M, and pseudodensity, ρ_θ, is taken at all time steps,

and is subtracted from the original vector to produce the eddy angular momentum, M^*, and eddy pseudodensity, ρ_θ^*. Eddy angular momentum is interpolated to vertical half levels, and the product of the eddy angular momentum and eddy pseudodensity is zonally averaged. The resulting product is substituted into the following central difference formula for the eddy transience term:

$$\frac{\partial}{\partial t}\left(\overline{\rho_\theta{}^* M^*}^\lambda\right)_{[i,j,k+\frac{1}{2}]} = \frac{\overline{\rho_\theta{}^* M^*}^\lambda_{[i+\frac{1}{2},j,k+\frac{1}{2}]} - \overline{\rho_\theta{}^* M^*}^\lambda_{[i-\frac{1}{2},j,k+\frac{1}{2}]}}{\Delta t}, \tag{B.16}$$

where the values of $\overline{\rho_\theta{}^* M^*}^\lambda$ at $i \pm \frac{1}{2}$ time steps are taken the first day of the month of interest and the first day of the following month, and $\Delta t = 1$ month. The final term of B.3, $\nabla \cdot \mathbf{IEPF}$, is the divergence of isentropic EP flux, which is defined in Equation 2.29, repeated here for convenience:

$$\nabla \cdot \mathbf{IEPF} = \frac{-1}{a\cos\varphi}\frac{\partial}{\partial\varphi}\left[\overline{\left(\rho_\theta v\right)^* M^*}^{\lambda,t}\cos\varphi\right] + \frac{\partial}{\partial\theta}\left[\overline{p^*\frac{\partial z^*}{\partial\lambda}}^{\lambda,t} - \overline{\left(\rho_\theta\dot{\theta}\right)^* M^*}^{\lambda,t}\right]. \tag{B.17}$$

We discretize B.17 in the following manner:

$$\begin{aligned}\nabla \cdot \mathbf{IEPF}_{[i,j+\frac{1}{2},k+\frac{1}{2}]} = &\left[\frac{-1}{a\cos\varphi}\frac{\partial}{\partial\varphi}\left(\overline{\left(\rho_\theta v\right)^* M^*}^{\lambda,t}\cos\varphi\right)\right]_{[i,j+\frac{1}{2},k+\frac{1}{2}]} + \\ &\left[\frac{\partial}{\partial\theta}\left(\overline{p\frac{\partial z}{\partial\lambda}}^{\lambda,t}\right)\right]_{[i,j+\frac{1}{2},k+\frac{1}{2}]} - \left[\frac{\partial}{\partial\theta}\left(\overline{\left(\rho_\theta\dot{\theta}\right)^* M^*}^{\lambda,t}\right)\right]_{[i,j+\frac{1}{2},k+\frac{1}{2}]}\end{aligned} \tag{B.18}$$

The first term of B.18 is the meridional eddy angular momentum flux divergence and is computed using a central difference scheme. Eddy meridional mass flux, $(\rho_\theta v)^*$, is computed by subtracting the zonal average of the meridional mass flux from the original value at all longitudes. Eddy angular momentum, M^*, is linearly interpolated to vertical half-levels, and then the product of eddy meridional mass flux and eddy angular momentum (eddy meridional an-

gular momentum flux) is zonally and monthly averaged. Similar to the meridional mass flux divergence term, before computation, latitude is linearly interpolated to meridional half-levels. The discretization formula for meridional eddy angular momentum flux divergence is:

$$\left[\frac{1}{a\cos\varphi}\frac{\partial}{\partial\varphi}\left(\overline{\left(\rho_\theta v\right)^* M^*}^{\lambda,t}\cos\varphi\right)\right]_{[i,j+\frac{1}{2},k+\frac{1}{2}]} = \frac{\left(\overline{\left(\rho_\theta v\right)^* M^*}^{\lambda,t}_{[i,j+1,k+\frac{1}{2}]}\cos\varphi_{[j+1]}\right) - \left(\overline{\left(\rho_\theta v\right)^* M^*}^{\lambda,t}_{[i,j,k+\frac{1}{2}]}\cos\varphi_{[j]}\right)}{a\cos\varphi_{[j+\frac{1}{2}]}\left(\varphi_{[j+1]} - \varphi_{[j]}\right)}. \quad \text{(B.19)}$$

The result is substituted into B.18, using the appropriate sign. The second term of B.18 is the divergence of the vertical angular momentum flux due to isentropic form drag. Note that in the zonal average:

$$\overline{p^*\frac{\partial z^*}{\partial\lambda}}^{\lambda} = \overline{p\frac{\partial z}{\partial\lambda}}^{\lambda}. \quad \text{(B.20)}$$

We made the replacement of $\overline{p^*\frac{\partial z^*}{\partial\lambda}}^{\lambda,t}$ with $\overline{p\frac{\partial z}{\partial\lambda}}^{\lambda,t}$ between Equations B.17 and B.18. Geopotential height (z) must be computed first using the Montgomery potential (or dry static energy) (s), which is defined in Equation 3.19, repeated here for convenience:

$$s \equiv \Pi\theta + gz, \quad \text{(B.21)}$$

where Π is the Exner function, which is defined as:

$$\Pi = c_p\left(\frac{p}{p_0}\right)^\kappa. \quad \text{(B.22)}$$

Rearranging B.21 and substituting B.22, we have:

$$z = g^{-1}\left(s - c_p\left(\frac{p}{p_0}\right)^\kappa\right). \quad \text{(B.23)}$$

The specific heat of a dry parcel of air, c_p, is $1.005\frac{kJ}{kg\cdot K}$. We use the reference pressure $p_0 =$ 1000 hPa. The exponent in B.23 is $\kappa = \dfrac{R}{c_p} = \dfrac{0.287\frac{kJ}{kg\cdot K}}{1.005\frac{kJ}{kg\cdot K}} = 0.287$ for a parcel of dry air. Discretizing B.23, we have:

$$z_{[i,j,k,l]} = g^{-1}\left(s_{[i,j,k,l]} - c_p\left(\frac{p_{[i,j,k,l]}}{p_0}\right)^{\kappa}\right). \tag{B.24}$$

After solving for z at all temporal, horizontal, and vertical levels, we compute isentropic form drag:

$$\left(p\frac{\partial z}{\partial \lambda}\right)_{[i,j,k,l]} = p_{[i,j,k,l]}\frac{z_{[i,j,k,l+1]} - z_{[i,j,k,l]}}{\lambda_{[l+1]} - \lambda_{[l]}} \tag{B.25}$$

with

$$\left(p\frac{\partial z}{\partial \lambda}\right)_{[i,j,k,-1]} = p_{[i,j,k,-1]}\frac{z_{[i,j,k,0]} - z_{[i,j,k,-1]}}{\lambda_{[0]} - \lambda_{[-1]}} \tag{B.26}$$

to "close" each latitude circle.

We zonally and monthly average the resulting isentropic form drag, $\overline{p\dfrac{\partial z}{\partial \lambda}}^{\lambda,t}$, and use that to compute the divergence using a central differencing scheme:

$$\left(\frac{\partial}{\partial \theta}\left(\overline{p\frac{\partial z}{\partial \lambda}}^{\lambda,t}\right)\right)_{[i,j,k+\frac{1}{2}]} = \frac{\left(\overline{p\frac{\partial z}{\partial \lambda}}^{\lambda,t}\right)_{[i,j,k+1]} - \left(\overline{p\frac{\partial z}{\partial \lambda}}^{\lambda,t}\right)_{[i,j,k]}}{\theta_{[k+1]} - \theta_{[k]}} \tag{B.27}$$

The resulting divergence of vertical angular momentum flux divergence due to isentropic form drag is linearly interpolated to half latitudinal levels ($j \pm \frac{1}{2}$) and substituted into B.18. The third and final term of B.18 is the divergence of vertical angular momentum flux to eddy heating. Eddy vertical mass flux, $\left(\rho_\theta \dot{\theta}\right)^*$, is computed by subtracting the zonal average of the vertical mass flux from the original value at all longitudes. Note that $\rho_\theta \dot{\theta}$ exists on "full" vertical levels (shown in B.13). We calculate the product of eddy vertical mass flux ($\left(\rho_\theta \dot{\theta}\right)^*$) and eddy angular momentum (M^*); the result, vertical angular momentum flux due to eddy heating, is zonally

and monthly averaged. The discretization formula for the vertical angular momentum flux divergence due to eddy heating is:

$$\left[\frac{\partial}{\partial\theta}\left(\overline{\left(\rho_\theta\dot{\theta}\right)^* M^*}^{\lambda,t}\right)\right]_{[i,j,k+\frac{1}{2}]} = \frac{\left(\overline{\left(\rho_\theta\dot{\theta}\right)^* M^*}^{\lambda,t}\right)_{[i,j,k+1]} - \left(\overline{\left(\rho_\theta\dot{\theta}\right)^* M^*}^{\lambda,t}\right)_{[i,j,k]}}{\theta_{[k+1]} - \theta_{[k]}} \tag{B.28}$$

The result is linearly interpolated to half latitudinal levels and substituted into B.18 with the appropriate sign. We now have all the pieces of B.18, which is computed and substituted into B.3, producing the residual term, $\frac{-\partial\overline{X}^{\lambda,t}}{\partial\theta}$, which includes vertical angular momentum flux convergence due to unresolved wave forcing. We can then divide each term by $a\cos\varphi$ (with latitude linearly interpolated to half-levels) to calculate the contribution of each term to the zonal wind acceleration, as shown in Equation 3.25.

Appendix C

Seasonal dependence of QBO transition: Revisiting Dunkerton 1990

In Timothy Dunkerton's 1990 paper "Annual Variation of Deseasonalized Mean Flow Acceleration in the Equatorial Lower Stratosphere" [Dunkerton, 1990], evidence is presented making an argument that the onset of the easterly phase transition of the QBO at 50 hPa occurs primarily in the northern hemisphere late Spring. He presents evidence from 3 observation locations with data extending from 1950-1990 to support this claim. I extend his analysis to include data up to the present, using observational data from Singapore, and imitating his figures. I also use ERA-Interim isentropic reanalysis interpolated to pressure levels to consider the zonal average of the zonal wind, as well as the longitudinal variation in the relationship. I show that while the majority of his analysis holds, there are some important differences. It certainly still remains the case, as Dunkerton pointed out, that while the seasonal cycle does appear to exert some controlling influence of the time of year of the onset of the easterly phase of the QBO, there is not enough evidence to assert an exact phase relationship. It could, however, strengthen forecasts of the timing of QBO transition.

C.1 Summary of the Analysis & Results of Dunkerton 1990

The paper "Annual Variation of Deseasonalized Mean Flow Acceleration in the Equatorial Lower Stratosphere" [Dunkerton, 1990] is commonly cited in papers about the quasi-biennial oscillation, describing seasonal dependence for the onset of the easterly phase of the QBO. Dunkerton's 1990 paper makes an argument that phase transitions at 50mb occur primarily in the northern spring/summer season. He suggests that the mechanism for this relationship involves the easterly phase of the QBO "stalling" between July and February, producing few onsets after August. Dunkerton argues that this "stall" is what drives the variability in the QBO period.

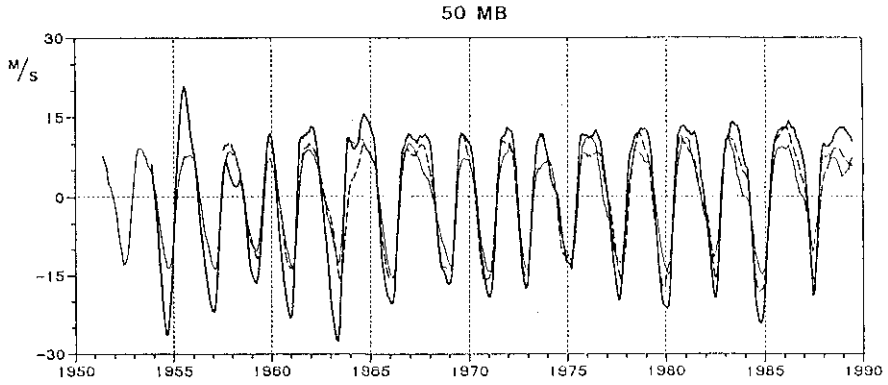

Figure C.1: Original Figure 1 of [Dunkerton, 1990]. "Time series of 50 mb mean zonal wind at Singapore (heavy solid), Balboa (light solid), and Ascension (dashed). Data were deseasonalized and smoothed with a 5-month running mean." 1951-1990.

Deseasonalized zonal wind data is utilized from 3 observation locations–Singapore (1.3°N), Balboa (9°N, Panama City), and Ascension Island (8°S)–extending from 1951-1990, as evidence to support this claim.

Figure C.1 is a time series of 50 mb mean zonal wind at the three locations, deseasonalized and smoothed with a 5-month running mean, showing the variability of the QBO phase, with larger amplitude at Singapore than other locations.

Figure C.2 is shows the timing of the "zero crossings" in the deseasonalized time series of 50mb zonal wind at Singapore. The cycle numbering follows [Dunkerton and Delisi, 1985] and has been laid out in Table C.2. The data show no easterly onsets (open circles) occurring after August.

Figure C.3 analyzes the timing of zonal wind accelerations associated with the QBO. High deseasonalized zonal wind accelerations are used as analogs for QBO phase transition. Since the seasonal cycle is removed from the zonal wind, he grouped positive and negative accelerations before averaging in order to "recover seasonal dependence," then applied a 5-month running mean. He notes that the strongest easterly accelerations at 30 mb tend to occur a couple of months before the strongest at 50 mb, and the strongest accelerations towards easterly winds occur in early NH autumn at 10 mb. He remarks that the 10 mb shows this shift from 50 mb because "the QBO is nearly opposite in phase."

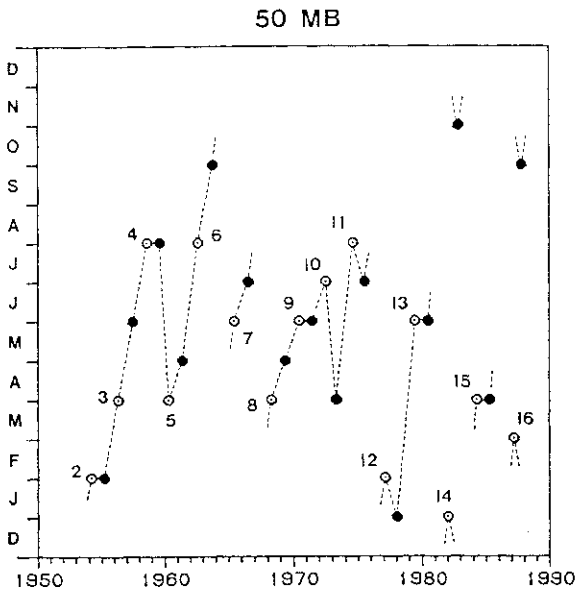

Figure C.2: Figure 2 of [Dunkerton, 1990]. "Zero crossings in the deseasonalized time series of 50mb zonal wind at Singapore. Solid (open) circles denote westerly (easterly) onsets. Numbering of cycles begins with east-west cycle 2; cycle 1 observed at Balboa begins in 1952 (see Fig. 1). Onset time plotted to nearest month."

Figure C.4 shows the number of zero crossings as a histogram for time of year, with east-to-west transitions on top and west-to-east transitions on the bottom. This includes six samples–a smoothed and un-smoothed version of the deseasonalized zonal wind time series at each of the three locations. These show similar results to Figure C.2.

Dunkerton remarks that the seasonal dependence he has shown contributes to the variability of the QBO and can improve predictions of the QBO, but he makes sure to note that he does not claim exact seasonal synchronization.

C.2 Data

In [Dunkerton, 1990], Dunkerton utilizes rawinsonde data, described as being from three locations with the following coordinates: Singapore (1.3°N, 256.1°W), Balboa (9.0°N,79.6°W), and Ascension (8.0°S, 14.4°W). Data is taken at 10mb, 30mb, and 50mb. As for the origin of data, the following line is included in the *Acknowledgments* section of [Dunkerton, 1990]: "I thank Jim Angell for providing up-to-date station data for tropical winds used in this study." Angell

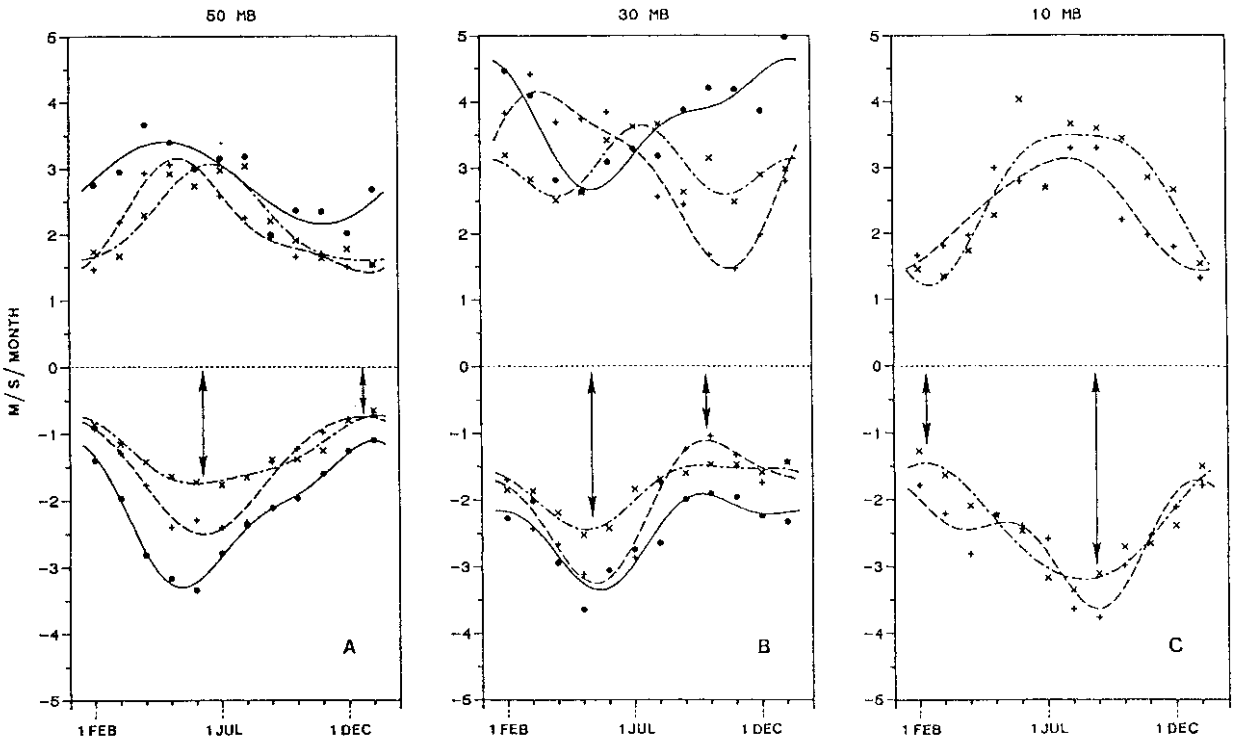

Figure C.3: Figure 3 of [Dunkerton, 1990]. "Average positive and negative accelerations as a function of time of year for Singapore (solid, ●), Balboa (dot-dash, ×), and Ascension (dashed, +). The seasonal cycle was removed prior to averaging the accelerations, and the data were smoothed with a 5 month running mean as in Fig. 1. Solid and dashed lines are a smooth fit to these data points (retaining zeroth, first, and second harmonics only). (a) 50 mb; (b) 30 mb; (c) 10 mb."

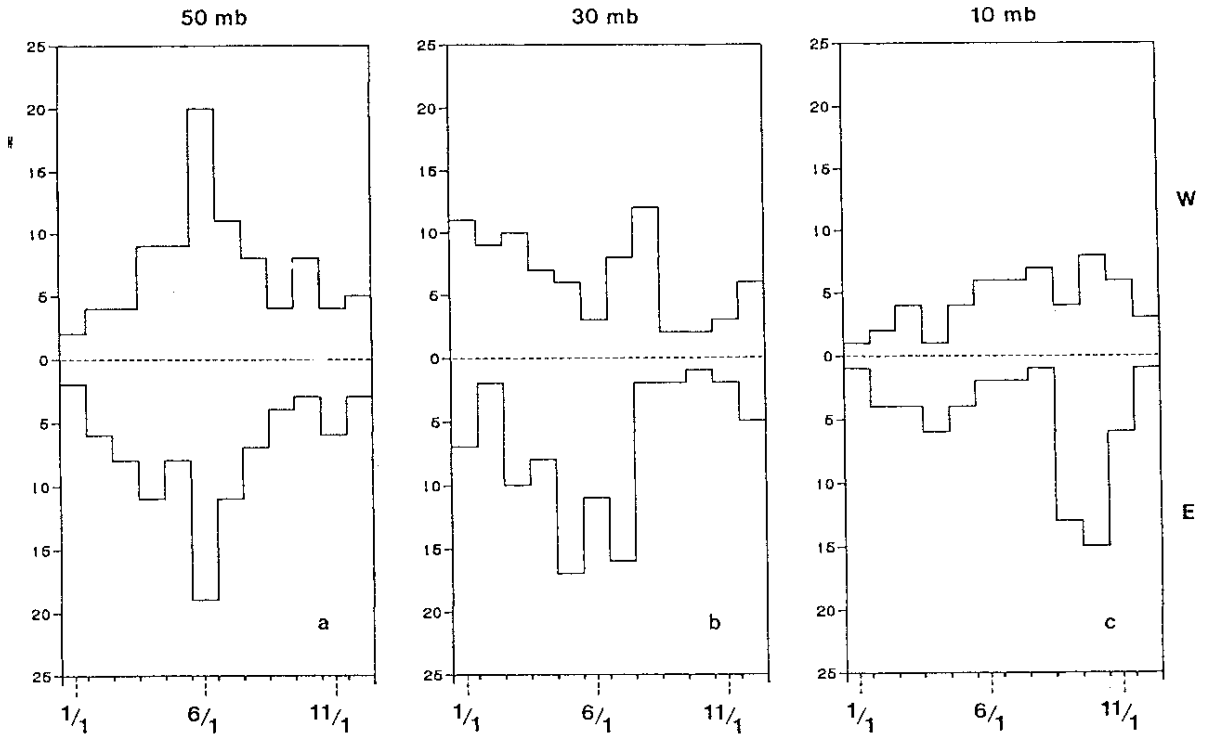

Figure C.4: Figure 4 of [Dunkerton, 1990]. "Number of zero crossings east-to-west (top) and west-to-east (bottom) as a function of time of year. Each histogram combines deseasonalized statistics from Balboa, Singapore, and Ascension, with and without the 5-month running mean. Consequently there are six times as many zero crossings in each histogram compared to the total number of QBO phase transitions in the data record (approximately 16 E-W and 16 W-E)."

Table C.1: Observational Data

Origin	Location	Temporal Range	Levels
NOAA NCDC IGRA	Changi airport (1.3667°N,103.9833°E)	1969-2022	50mb
MSS	Changi airport (1.3667°N,103.9833°E)	1979-2022	30mb, 10mb

worked at NOAA Air Resources Laboratory for the majority of his career. In an effort to find data that is either identical or as similar as possible to imitate the figures in this article, I utilized data from NOAA's NCDC's IGRA, which includes monthly average observation from a station at Changi airport in Singapore at coordinates (1.3667°N,103.9833°E) from 1955-2022. However, observations at 50mb are not consistent until 1969 in this dataset, so I utilized data 1969-2022 for zonal wind at 50mb. For measurements at 30mb and 10mb, I utilized the historical upper air observations from Meteorological Service of Singapore's site from 1979-2022. I lay out the osbervational data I utilized in Table C.1. In order to analyze this relationship in the zonal mean, I intended to use ECMWF ERA-5 reanalysis on pressure surfaces. However, I had ERA-Interim isentropic reanalysis quickly available to me, and it was very easy to interpolate to pressure levels to see results at 50, 30, and 10 mb to imitate figures from the original paper. I use the zonally averaged zonal wind, meridionally averaged between 5°S and 5°N, and deseasonalized.

C.3 Figure Imitations and Discussion

In Figures C.5 & C.6, I imitate Figure C.1 with Singapore sonde data and ERA-I data, respectively.

Figure C.7 compares the differences in these time series, in local and zonal mean zonal wind associated with the QBO, with the Singapore data trimming to 1979-2018 to match up with the time span of the ERA-I time series. There is good agreement between the two time series in period. The amplitude in Singapore is enhanced, but this is expected due to the proximity of the Singapore station to the Equator. The amplitude of the QBO maximizes at the Equator and weakens with increasing latitude [Dunkerton and Delisi, 1985], and the ERA-Interim data is meridionally averaged from 5°S-5°N.

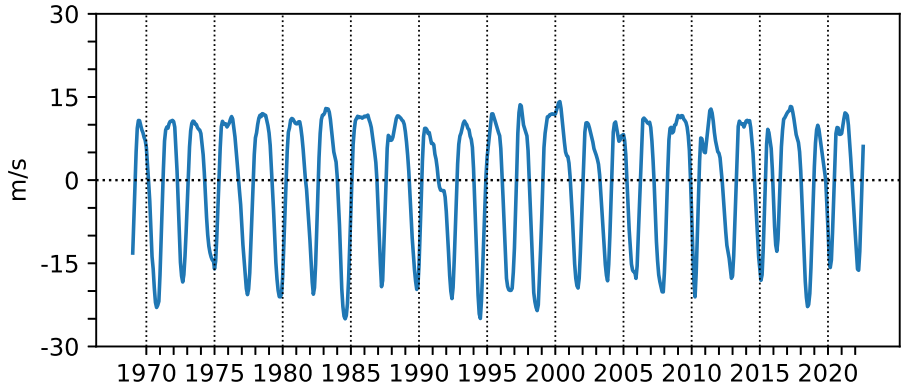

Figure C.5: Time series of 50 mb mean zonal wind at Singapore. Deseasonalized and smoothed with a 5-month running mean. 1969-2022. A remake with updated data for Figure 1 of [Dunkerton, 1990].

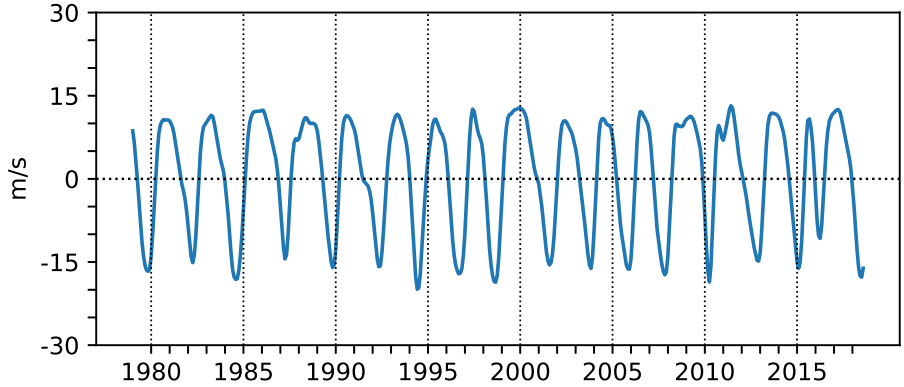

Figure C.6: Time series of 50 mb mean zonal wind averaged from 5°N-5°S from ERA-I reanalysis. Deseasonalized and smoothed with a 5-month running mean. 1979-2018. Adapted from Figure 1 of [Dunkerton, 1990].

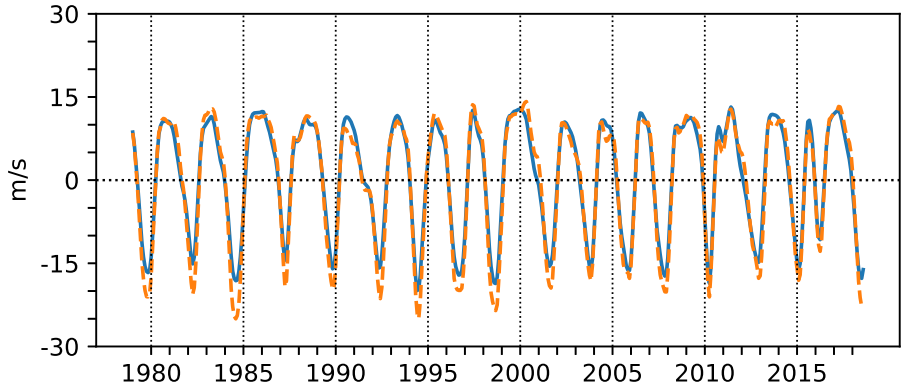

Figure C.7: Time series of 50 mb mean zonal wind averaged from 5°N-5°S from ERA-I reanalysis *(solid blue)* and 50 mb mean zonal wind at Singapore (*dashed orange*). Both deseasonalized and smoothed with a 5-month running mean. 1979-2018.

The phase of Dunkerton's Singapore data is shifted slightly from the Singapore data I used in the years of overlap. The reason for this is unclear, because regardless of measurement location, the phase of the QBO does not vary in horizontal space. Figure C.8 is Figure C.1 cropped to just 1969-1989 with the zonal wind at Singapore from 1969-1989 overlaid in blue. The magnitude of Dunkerton's Singapore data, the solid dark line, matches fairly closely with my Singapore sonde data. However, Dunkerton's data from all three locations is shifted forward in time from the updated data. The same effect is shown in Figure C.9, with zonal mean ERA-I appearing to represent the mean amplitude of Dunkerton's data fairly well, but again, the phases are misaligned by a few months in some places. This is concerning for data used to perform a seasonal analysis. Although, I do have a suspicion that the actual data used in Dunkerton's analysis matches my data more accurately than is depicted in these overlap figures and that the plot was poorly aligned on the time axis when it was created.

Figures C.10 & C.11 imitate Figure C.2 with Singapore sonde data and ERA-I data, respectively. The numbering represents a continuation of the numbering used to identify various QBO cycles and is specified in Table C.2. The differences in the timing of the zero-crossings between samples is never more than a month, with an exception between updated Singapore data and ERA-I in cycle 22 in 2001, both still in the NH Spring. The lack of disagreement in the timing of

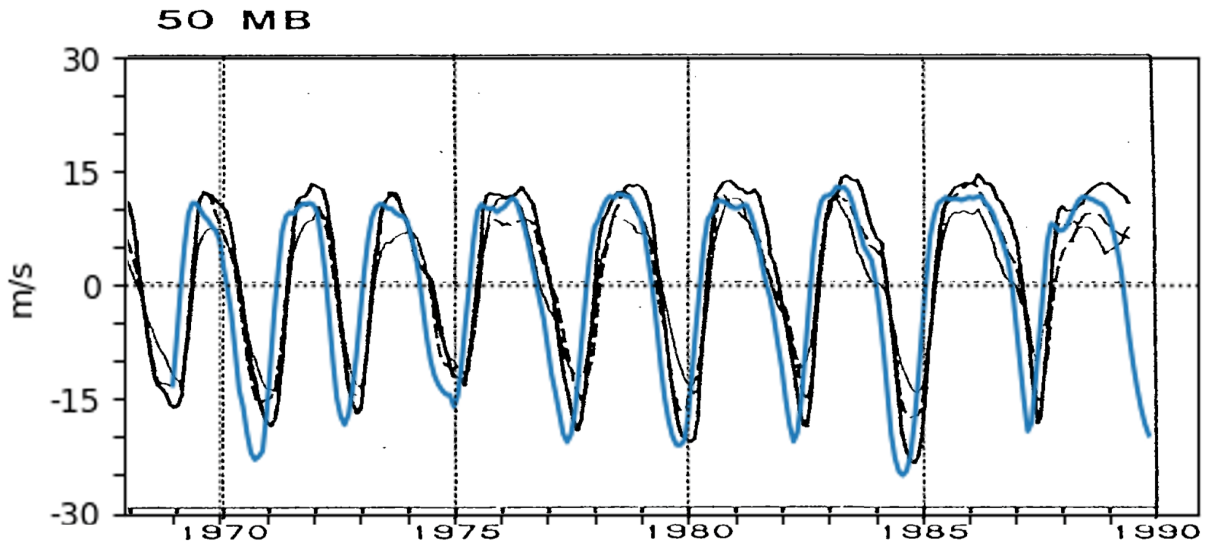

Figure C.8: Figure 1 from [Dunkerton, 1990], cropped to 1969-1989, overlaid with the time series of 50 mb zonal wind at Singapore (*solid blue*). Both are deseasonalized and smoothed with a 5-month running mean. Dunkerton's Singapore is the solid black line.

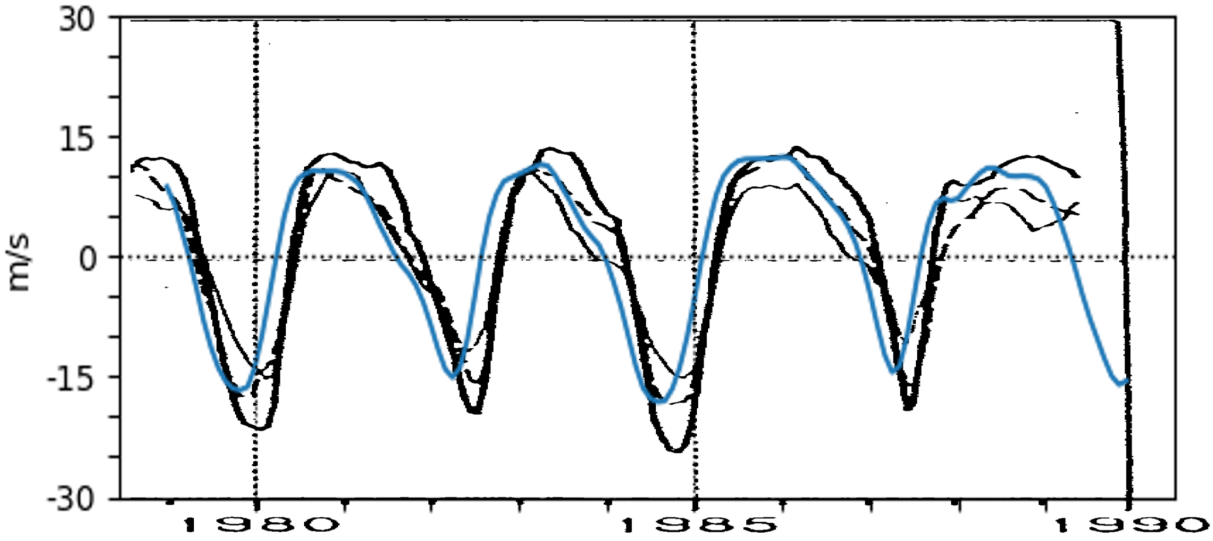

Figure C.9: Figure 1 from [Dunkerton, 1990], cropped to 1979-1989, overlaid with time series of 50 mb mean zonal wind averaged from 5°N-5°S from ERA-I reanalysis (*solid blue*). Both are deseasonalized and smoothed with a 5-month running mean.

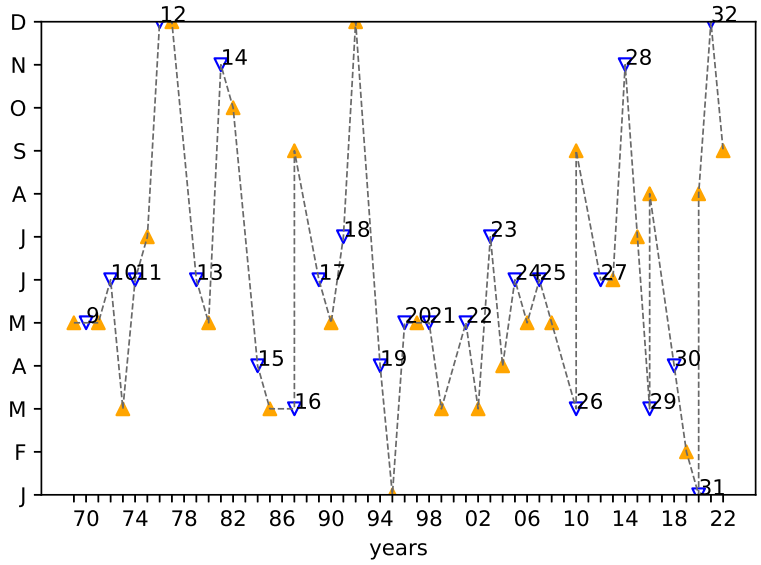

Figure C.10: Zero crossings in the deseasonalized time series of 50 mb zonal wind at Singapore. 1969-2022. Orange solid triangles indicate transition from easterly to westerly winds, and blue upside down triangles indicate transition from westerly to easterly winds. A remake with updated data for Figure 2 of [Dunkerton, 1990].

zero-crossings bolsters my hypothesis that the data Dunkerton used is not in fact off by a few months, but is drawn poorly in Figure C.1.

In order to see the results shown in Figures C.2, C.10, and C.11 more clearly, Figure C.12 highlights the periodic nature of the dataset. The radial axis is approximately temporal with higher cycle numbers towards the outer edge and vice versa. The angular axis is the time of year. There are slight phase differences present in the exact timing of the easterly onset between the samples, but the tendency to occur in late spring and early summer of the Northern Hemisphere is evident by the grouping of cycle numbers in March-July, as postulated by Dunkerton. Differing from the Dunkerton Singapore data, the addition of more QBO cycles with the other two samples shows that some onsets do occur outside the aforementioned season, which supports the idea that the synchronization is by no means exact, and there is no "phase locking" between the QBO and the seasonal cycle.

Figures C.13 & C.14 imitate Figure C.3 with Singapore sonde data and ERA-I data, respectively. While there was a fair amount of agreement in Dunkerton's data and updated data for

Table C.2: This table lists the numbering used in Figures C.2, C.10, and C.11 for Dunkerton's data used from Singapore, the Singapore data sourced from NOAA, and the ERA-Interim reanalysis, with the timing of the onset of the QBO-E phase.

	Dunkerton Singapore Date	Singapore Sonde Date	ERA-I Date
2	Jan/Feb 1954		
3	Mar/Apr 1956		
4	Jul/Aug 1958		
5	Mar/Apr 1960		
6	Jul/Aug 1963		
7	May/June 1965		
8	Mar/Apr 1968		
9	May/Jun 1970	May/Jun 1970	
10	Jun/Jul 1972	Jun/Jul 1972	
11	Jul/Aug 1974	Jun/Jul 1974	
12	Jan/Feb 1977	Dec/Jan 1976	
13	May/Jun 1979	Jun/Jul 1979	Jun/Jul 1979
14	Dec/Jan 1982	Nov/Dec 1981	Nov/Dec 1981
15	Mar/Apr 1984	Apr/May 1984	Apr/May 1984
16	Feb/Mar 1987	Mar/Apr 1987	Feb/Mar 1987
17		Jun/July 1989	Jun/July 1989
18		Jul/Aug 1991	Aug/Sep 1991
19		Apr/May 1994	Apr/May 1994
20		May/Jun 1996	Apr/May 1996
21		May/Jun 1998	Apr/May 1998
22		May/Jun 2001	Feb/Mar 2001
23		Jul/Aug 2003	Jun/July 2003
24		Jun/July 2005	Jun/July 2005
25		Jun/July 2007	Jun/July 2007
26		Mar/Apr 2010	Feb/Mar 2010
27		Jun/July 2012	May/Jun 2012
28		Nov/Dec 2014	Oct/Nov 2014
29		Mar/Apr 2016	Mar/Apr 2016
30		Apr/May 2018	Mar/Apr 2018
31		Jan/Feb 2020	
32		Dec/Jan 2021	

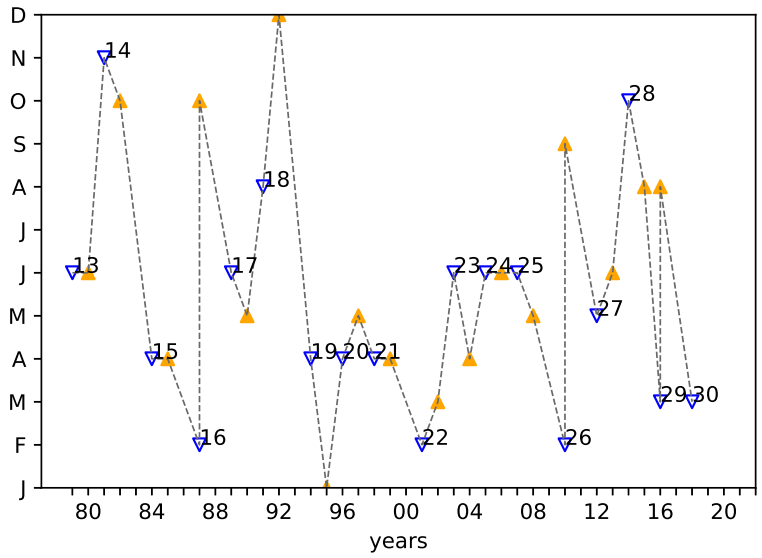

Figure C.11: Zero crossings in the deseasonalized time series of 50 mb zonally averaged zonal wind (ERA-I). 1979-2018. Orange solid triangles indicate transition from easterly to westerly winds, and blue upside down triangles indicate transition from westerly to easterly winds. Adapted from Figure 2 of [Dunkerton, 1990].

originals and reproductions of Figure C.2 with the zonal wind zero-crossings, the accelerations do not show the same level of agreement. In a broad sense, all three samples at 50 mb show strongest accelerations toward easterlies in the first half of the year. All samples show no relationship in time or height for a shift to westerly winds. The negative accelerations get stronger on average with height in all three samples.

However, in the updated data, weakest accelerations towards easterlies, as an analog for the maximum of the QBO easterly phase, tend to occur at 50 & 10 mb in the Northern Hemisphere fall. Whereas Dunkerton's results show the maximum occurring in the Northern Hemisphere winter, shifted forward in time by a few months from updated data. Contrary to my previous assertion, this lends some evidence that the data used in Dunkerton's study could actually being shifted forward in time by a couple months, as shown in Figures C.8 & C.9, not just misaligned in the plots.

Another major difference in the figures is at 10 mb. It should be noted that Dunkerton does not have Singapore data at 10mb, only data from Ascension Island and Panama City. In Figure

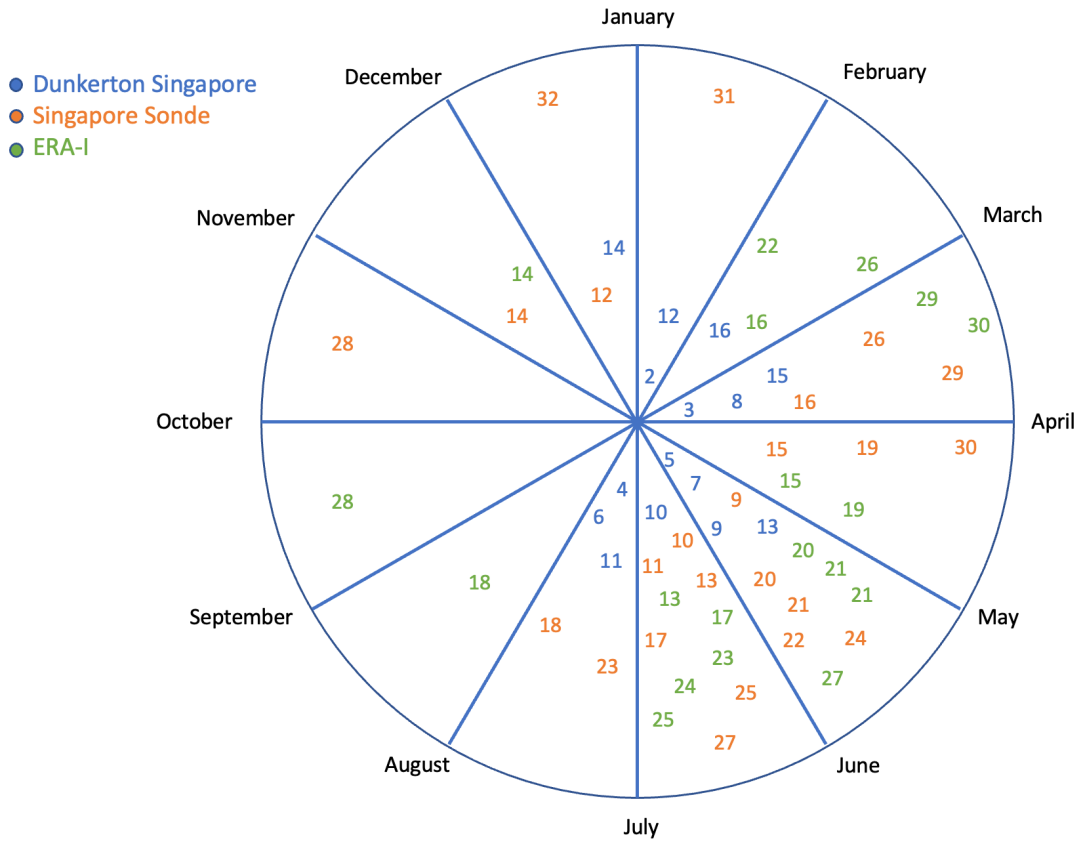

Figure C.12: Polar plot of the data from Figures C.2, C.10, and C.11. Numbers are the QBO cycle numbers described in Table C.2.

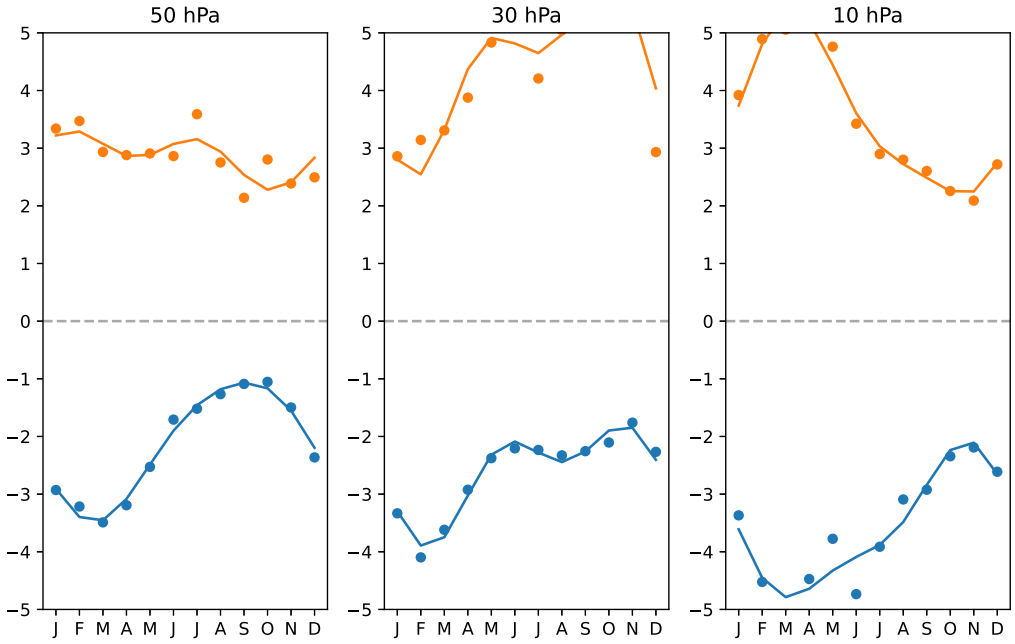

Figure C.13: Average positive and negative accelerations as a function of time of year for Singapore. Accelerations are computed from deseasonalized wind, then a 5 month running mean was applied to the accelerations, then positive & negative accelerations are averaged. Solid lines are a smooth fit to these data points (retaining zeroth, first, and second harmonics only). Adapted from Figure 3 of [Dunkerton, 1990].

C.3, at 50 & 30 mb, Singapore has a higher magnitude than the other two locations, but the qualitative temporal relationship remains consistent across stations. Dunkerton made a point about shift in the time of year of the strongest negative accelerations with height, showing that 10 mb and 50 mb are almost inverses of one another. However, updated data does not show this relationship. In contrast, Figures C.13 & C.14 show a similar functional relationship at 50 & 10 mb with stronger magnitude at 10 mb. As expected, ERA-I and Singapore show broadly similar temporal patterns at all heights with weakened temporal contrast and smaller magnitude in the zonally averaged data.

To get an even closer look comparing datasets at each height, I made polar plots, Figures C.15, C.16, and C.16, at 50, 30, & 10 mb, respectively. The radial axis is the negative accelerations of the zonal mean flow with time of year on the angular axis. In Figure C.15, at 50 mb, we see

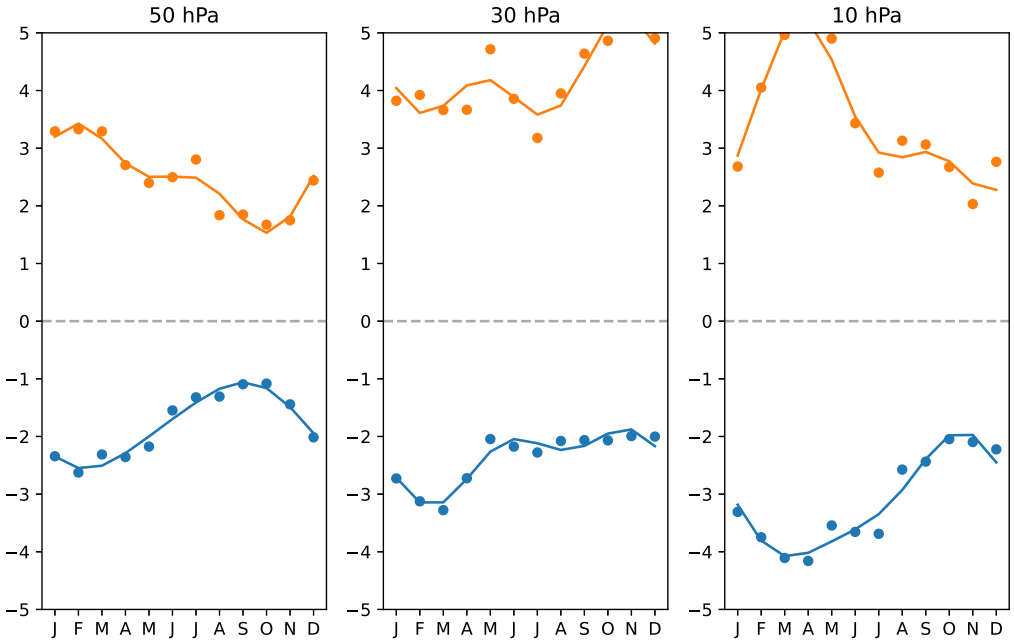

Figure C.14: Average positive and negative accelerations as a function of time of year (ERA-I). Accelerations are computed from deseasonalized zonally averaged zonal wind, then a 5 month running mean was applied to the accelerations, then positive & negative accelerations are averaged. Solid lines are a smooth fit to these data points (retaining zeroth, first, and second harmonics only). Adapted from Figure 3 of [Dunkerton, 1990].

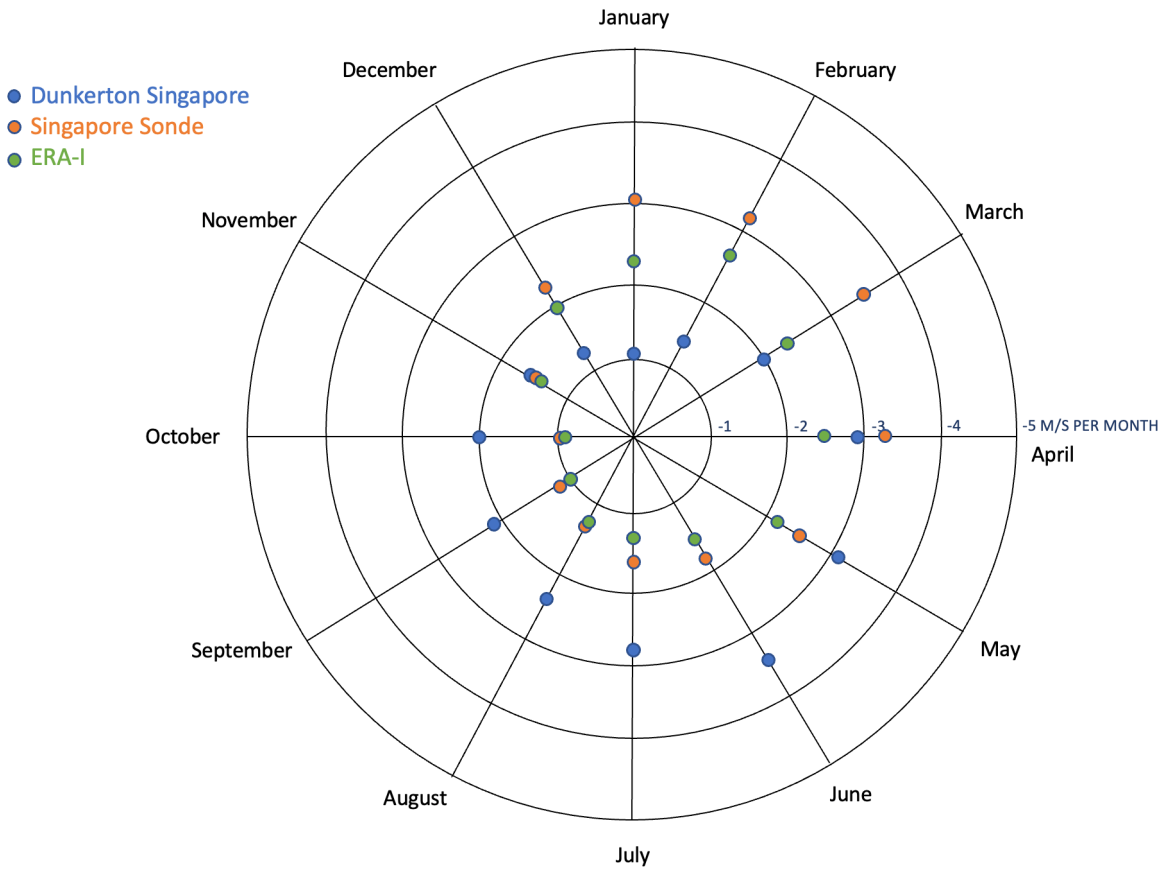

Figure C.15: Polar plot of the data from Figures C.3, C.13, and C.14, showing average negative acceleration of the mean zonal flow at 50 mb, associated with each month of the year.

amplitude agreement between three samples, but the phases are shifted in Dunkerton's data by a few months. With the added clarity of the overlay, strongest negative accelerations occur early in the calendar year for updated data (*orange and green*), but closer to late Spring and early NH Summer for Dunkerton data (*blue*). In Figure C.16, at 30 mb, a similar pattern emerges of a phase shift between old and updated data. In ERA-I & Singapore data, high accelerations occur in the early NH Spring with Dunkerton highest accelerations in late NH Spring. Although the samples do overlap with low accelerations in the final months of the year. In Figure C.17, at 10 mb, we are missing Dunkerton's Singapore data, but can see the agreement in ERA-I and updated Singapore data in phase with strong accelerations in NH Spring and weak accelerations in NH Fall.

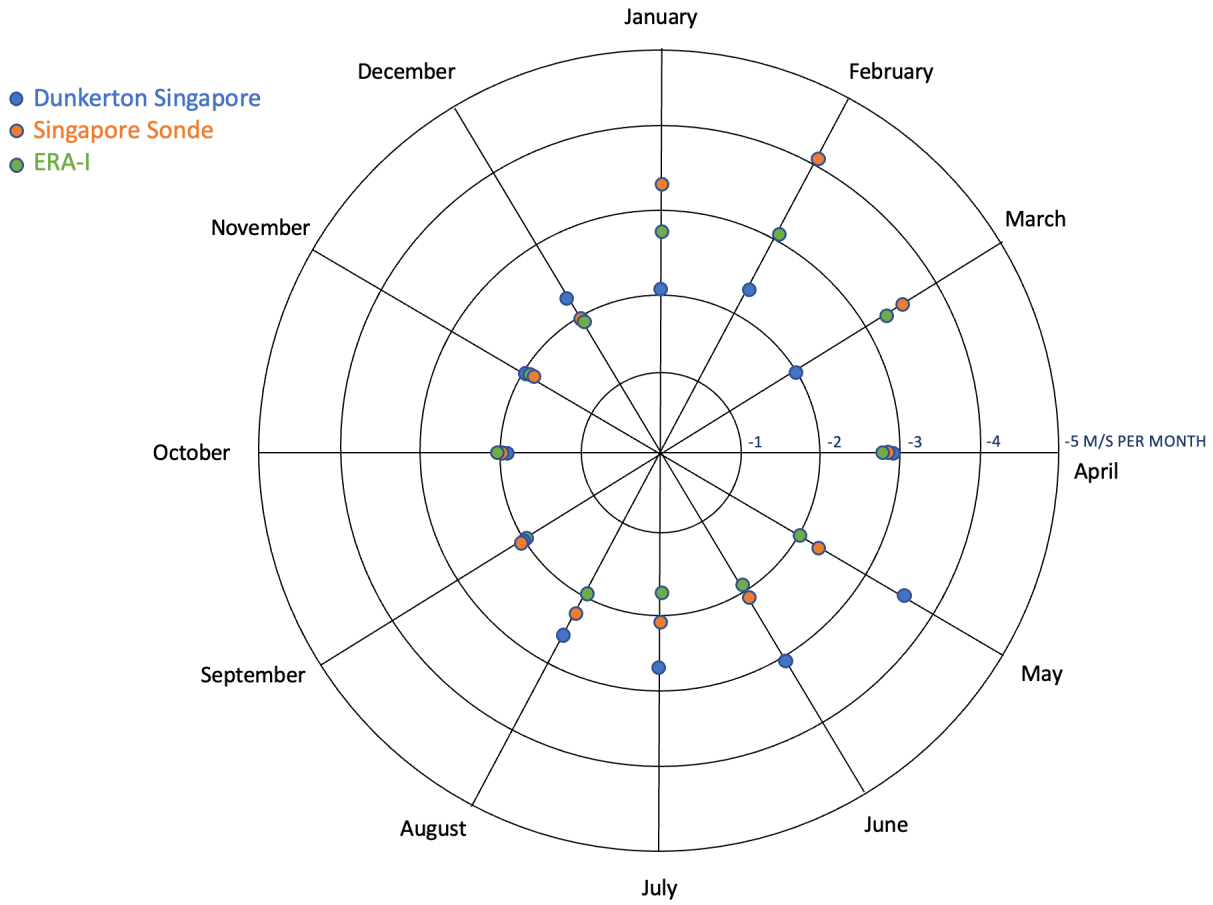

Figure C.16: Polar plot of the data from Figures C.1, C.13, and C.14, showing average negative acceleration of the mean zonal flow at 30 mb, associated with each month of the year.

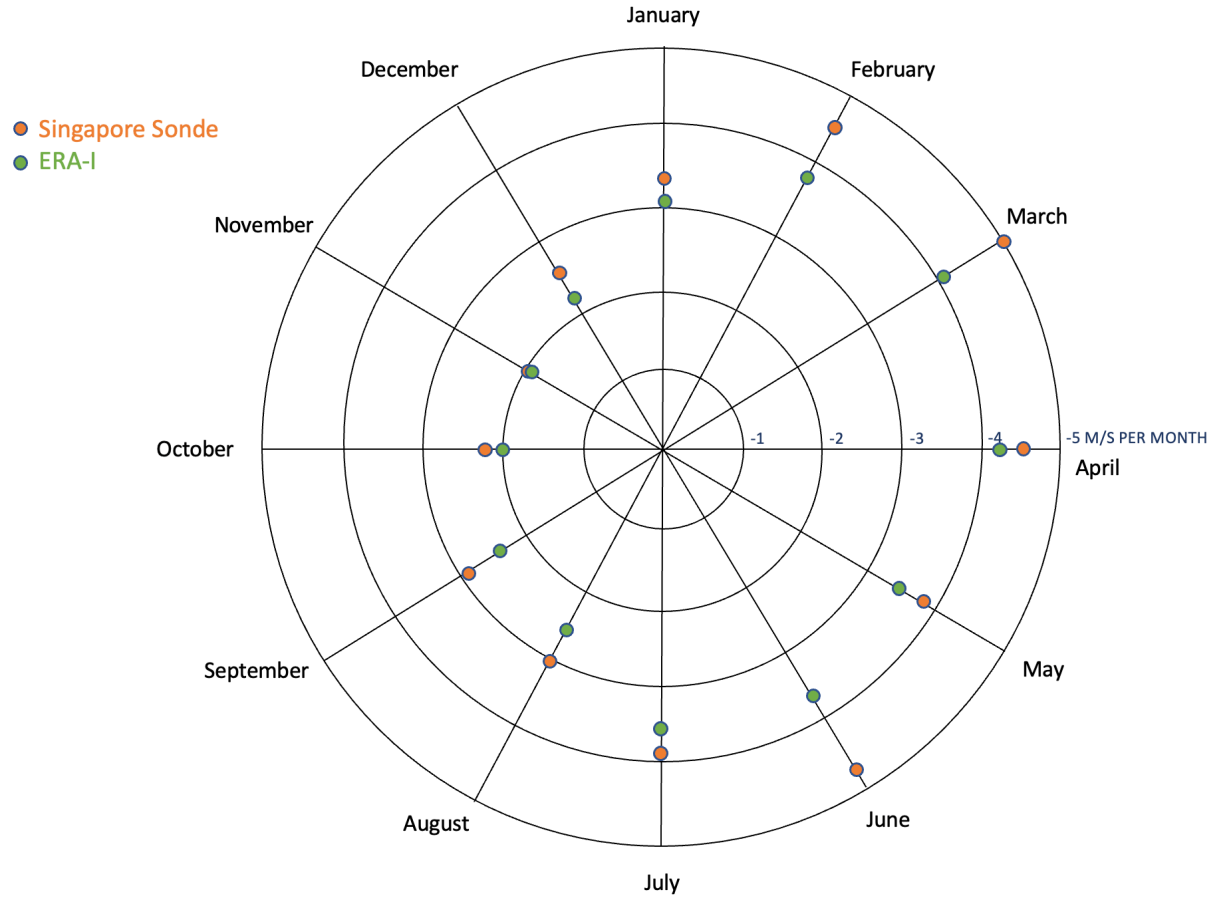

Figure C.17: Polar plot of the data from Figures C.13 and C.14, showing average negative acceleration of the mean zonal flow at 10 mb, associated with each month of the year.

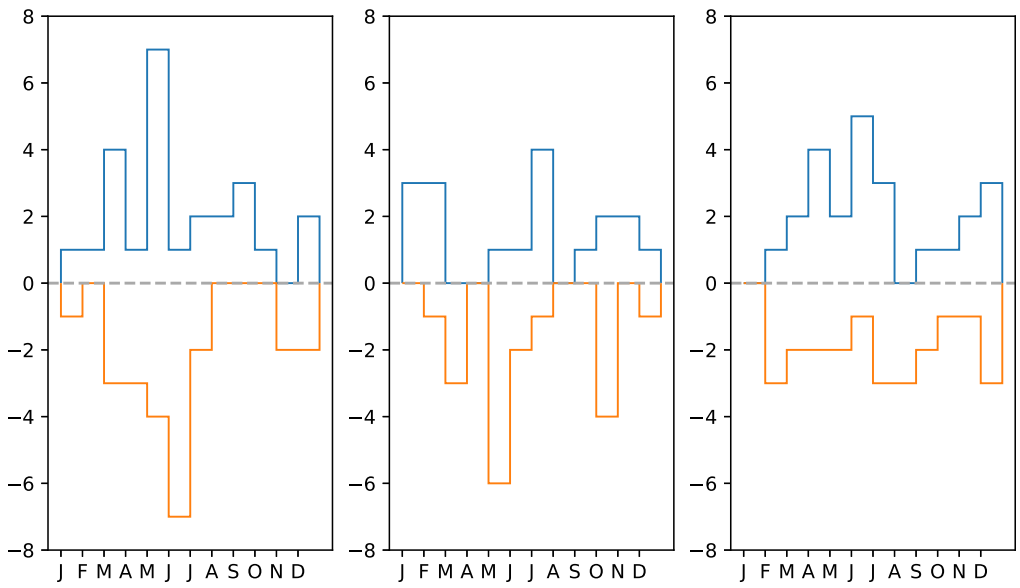

Figure C.18: Number of zero crossings east-to-west (top) and west-to-east (bottom) as a function of time of year. Each histogram includes deseasonalized statistics from Singapore without the 5-month running mean. Adapted from Figure 4 of [Dunkerton, 1990].

Figures C.18 & C.19 imitate Figure C.4 with Singapore sonde data and ERA-I data, respectively. An important distinction should be made that these each include only 1 sample of data in the histogram bins; while Dunkerton's Figure C.4 includes six samples–all three measurement locations, each with a smoothed and un-smoothed version of the data. I am not sure what the benefit of this was, but that explains the difference in the extent of the y-axis between my and his figures. There is decent qualitative agreement between all three samples at 50 & 30 mb. Dunkerton & ERA-I show some agreement at 10 mb, but there is no apparent temporal relationship in the updated Singapore data.

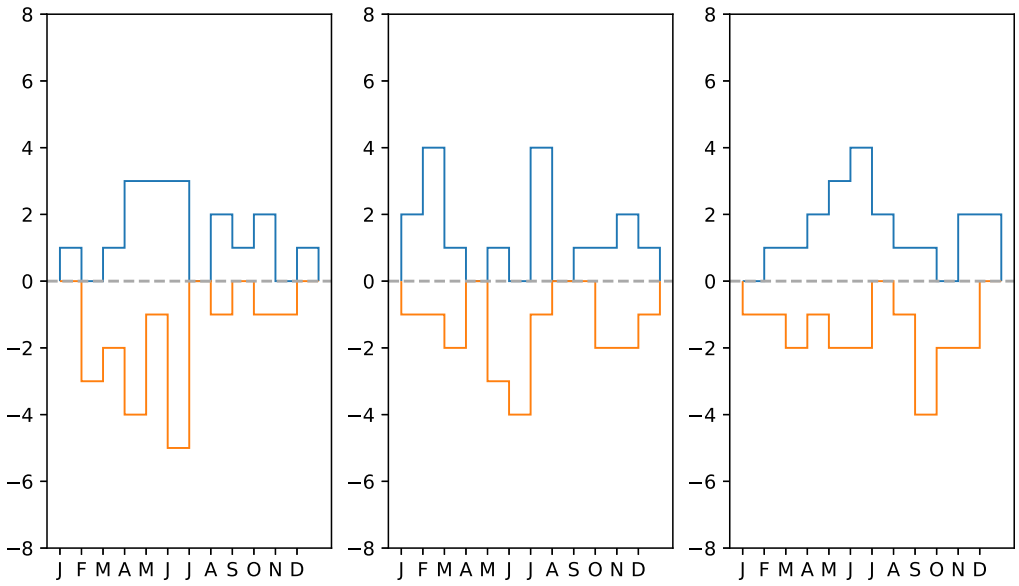

Figure C.19: Number of zero crossings east-to-west (top) and west-to-east (bottom) as a function of time of year. Each histogram includes deseasonalized statistics from zonal average ERA-I without the 5-month running mean. Adapted from Figure 4 of [Dunkerton, 1990].